Processing, Microstructure, and Thermal/Mechanical Properties of Al/Carbon Composites

January 2019

Yi Lifu

Contents

Chapter 1: Introduction

In recent years, with the continuing development in the fields of electronic packaging and thermal management applications, various electronic devices with high calculating speed, miniaturization, and light weight have become new trends [1]. However, the concurrent increase in power density of electronic components leads to generation of large amount of heat, which seriously reduces the efficiency and service life of the electronic devices [2]. Moreover, in order to reduce the fuel consumption and environment pollution caused by CO_2 emissions, thermal management materials were also widely used in electric vehicle systems. Especially, in modern automotive engines, the electronic control unit plays the crucial role of controlling and integrating different complex actions such as mixture formation, combustion and exhaust gas treatment [3]. Therefore, it is important to develop efficient heat-dissipation materials to meet the requirements of rapid heat removal.

In general, the heat-dissipation materials were required to possess high thermal conductivity (TC) and low coefficient of thermal expansion (CTE). Since the conventional heat sink materials were difficult to satisfy both of them, more and more researchers have focused on developing composite materials. The densities and thermal properties of the representative electronic packaging materials were listed in table 1.1. The first and second generation materials used as substrate in electronic packaging were CuMo, CuW, BeO, and Al/SiC, showed TC values of ~200 W/mK. However, with the rapid development in the modern electronic devices, they were no longer able to meet the requirements of thermal management [4]. In order to design a new generation

material, metal matrix composites (MMCs) have attracted particular interest by many research groups to fabricate heat-dissipation materials among various composite material systems. For the metal matrix with high TC, aluminum (Al) has been extensively used due to its lightweight and low cost in comparison with copper and silver. Besides, carbon materials, such as diamond, carbon fibers (CFs) including carbon nanotubes (CNTs) and nanofibers (CNFs), and graphite have become popular research topics because of their outstanding thermal properties, which make them ideal second phases for Al matrix composites. However, the utilization of diamond is seriously limited by its high price and hardness. In addition, the addition of CNTs and CNFs will lead to more Al/C interfaces, which result in larger interfacial thermal resistance. Thus, in this research, graphite and CFs were chosen as the second phases. It is believed that through controlling the composition and orientation of the second phases in Al matrix, good thermal and mechanical properties of the Al matrix composites (AMCs) can be obtained [5-7].

On the other hand, the fabrication method is also an important factor, which determines the properties, productivity, and cost of the AMCs. As shown in Fig. 1.1, the fabrication processes of AMCs can be classified in two routes: liquid-state process and solid-state process [8]. The liquid-state process mainly includes stir casting, squeeze casting, and pressure infiltration. These methods can fabricate the AMCs with high composition and ideal orientation of second phase. However, the high processing temperature may lead to the formation of some compounds at the interfaces, which degrade the thermal and mechanical properties. The solid-state process is generally divided into hot pressing, spark plasma sintering (SPS), hot extrusion, and so on. The hot pressing and SPS methods have been widely investigated to fabricate the AMCs

with high thermal and mechanical properties, however, they are difficult to be used in mass production due to their high costs and limitation in degree of freedom on the composites shape. In comparison, extrusion is a cost-effective processing technique in fabricating elongated products with various cross-sectional shapes. It can also be applied to form powders or poor-processing materials, since heavy deformation can be achieved under a high hydrostatic pressure. Furthermore, it is possible to control the preferred orientation of grains during extrusion, especially for those materials with layered structure such as graphite. However, few works have been reported to fabricate AMCs by extrusion process. Therefore, in this research, a hot-extrusion technique was proposed to prepare Al/carbon composites.

Table 1.1 Densities and thermal properties of representative electronic packaging materials [7]

Material	Density (g/cm^3)	CTE ($\times 10^{-6}$/C)(25-150°C)	TC (W/mK)
Al	2.7	26	237
Cu	8.9	17	398
Ag	10.5	19	431
Si	2.3	4.2	151
GaAs	5.23	6.5	54
CuW	15.7-17.0	6.5-8.3	180-200
CuMo	10	7-8	160-170
BeO	3	6	260
SiC	3.2	2.7	200-270
Al/SiC	2.9-3.3	6.2-16.2	120-220
Al/diamond	3-3.2	7-7.5	400-600
Al/CF	2.4-2.5	7-9.4	170-320
Al/graphite	2.4-2.5	7.5-16.9	200-780

Fabrication processes of AMCs

Liquid-state process	Solid-state process
Stir casting	**Hot pressing**
Squeeze casting	**Spark plasma sintering (SPS)**
Pressure infiltration	**Hot extrusion**
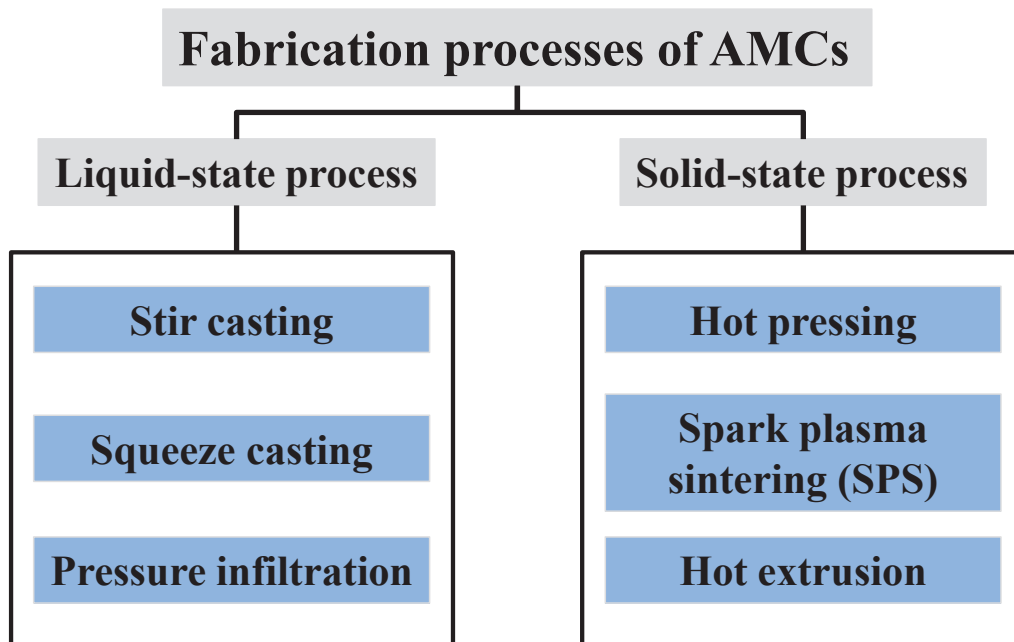
Fig. 1.1 Fabrication processes of AMCs

1.1 Development status of AMCs for thermal management applications

1.1.1 Al/SiC composites

As the second generation of heat dissipation materials, Al/SiC composites showed better thermal properties, lower density and cost in comparison with the first generation heat dissipation materials like CuMo and CuW. These advantages attracted much attention of semiconductor manufacturers. Since the late 1980s, Al/SiC composites have been used for thermal management packaging solutions for high-power output microwave application. In the early 1990s, Al/SiC composites were introduced as power substrates instead of Cu substrates in the field of commercial communication applications for cellular base stations. From the 21st century, with the rapid increase in application of personal computer, Al/SiC composites were widely investigated by more and more researchers to meet the demand of CPU thermal management [9-11].

Xu *et al.* [12] fabricated the Al/SiC composites by powder metallurgy and

extrusion with TCs of 150-180 W/mK. Lee *et al.* [13] consolidated the Al/SiC composites by squeeze casting process with 120-177 W/mK and CTEs of 6-10 ppm/K. Further, Molina *et al.* [14] prepared the Al/SiC composites by liquid infiltration method with TCs of 150-220 W/mK and CTEs of 7.8-10.8 ppm/K. Based on the above reports, it is found that the CTE of Al can be easily reduced due to the low CTE of SiC (2.7 ppm/K). However, due to the unsatisfied TC of SiC (200-270 W/mK), the TC of Al is hard to be enhanced. From the 2010s, with the increasing power density in electronic packing field, the unsatisfied TC of Al/SiC composites became no longer able to meet the thermal management requirements. Therefore, more and more researchers started to used diamond, graphite, and CFs instead of SiC.

1.1.2 Al/diamond composites

Owing to the exceptionally high TC of 2500 W/mK and low CTE of 1.3 ppm/K of diamond at room temperature, diamond appears to be a promising thermal management carbon material. In addition, the price of good-quality synthetic diamonds also continuously decreases in recent years. Thus, Al/diamond composites have been widely developed to replace the traditional heat sinks.

Chen *et al.* [15] and Johnson *et al.* [16] prepared Al/diamond composites by a pressureless infiltration technique with TCs of 259-288 W/mK at diamond contents of 50-75 vol%. The experimental TCs were much lower than the theoretical TCs due to the formation of Al_4C_3 at the interfaces between Al and diamond, which leads to larger interfacial thermal resistance. In order to improve the interfacial bonding and suppress the formation of Al_4C_3, surface coating of diamond was considered as an effective way. Liang *et al.* [17] fabricated Al/Ti-coated diamond composites by SPS process, and Tan

et al. [18] fabricated Al/W-coated diamond composites by hot pressing process. At a diamond content of 50 vol%, the Al/Ti-coated diamond composites showed TC of 491 W/mK and the Al/W-coated diamond composites exhibited TC of 599 W/mK. On the other hand, from the viewpoint of enhancing the relative density and interfacial bonding, the effect alloy addition on microstructure and TC was investigated by Mizuuchi *et al*. [19-20]. As reported, the Al/diamond composites with Al-Mg alloy fabricated by SPS at a temperature range between the solidus and liquidus temperatures of Al-Mg alloy. The relative packing density of 97.5% and the TC of 403 W/mK were obtained for Al-45.5 vol% diamond composite. Further, their research group also reported that the SPSed Al-50 vol% diamond composites with Al-Si alloy showed higher relative packing density of 99% and the TC of 552 W/mK.

Although the Al/diamond composites exhibited excellent thermal properties in comparison with Al/SiC composites, the isotropic thermal properties, high hardness, and high price of diamond still seriously limit its application in thermal management field. In order to overcome these constraints, Al/CF composites and Al/graphite composites with anisotropic thermal properties, good workability, and relatively low price were widely investigated for heat sinking application.

1.1.3 Al/CFs composites

In recent decades, fibrous composites were prepared with various metallic matrices. Among these, Al/CFs composites have been the preferred choice of researchers, due to its low density, good workability and thermal properties. In particular, the reinforcement of AMCs with CNTs can significantly enhance the mechanical properties. For example, Bakshi *et al*. [21] fabricated the Al-Si alloy-10 vol% CNTs composites by

6

powder mixing and plasma sprayed onto the mild steel substrate. The mechanical properties, such as elastic modulus and yield strength, were reported to be enhanced. However, the TC was declined to almost half (73 W/mK) as compared to cast Al-Si alloy (170 W/mK), due to the severe aggregation of CNTs and large amount of Al/CNTs interfaces. In order to reduce the aggregation and improve the interfacial bonding, larger sized CFs were chosen with surface coating. The research groups of Liu *et al*. [22] fabricated Al/chromium carbide-coated CFs composites by SPS process. The CFs were randomly oriented in-plane perpendicular to the pressing direction, leading to the in-plane TC values of 221 W/mK. Although the TC values were not high, the Al/CFs samples showed low CTE of 9.4 ppm/K at only 45.4 vol% CFs content. Further, Kurita *et al*. [23] fabricated dense Al/CF composites with Al-Si alloy by hot pressing process, with TC and CTE of 258 W/mK and 7.0 ppm/K. In order to align the CFs in one direction and further enhance the TC, Lee *et al*. [24] prepared the unidirectional Al/CF composites by low pressure infiltration process. However, due to the formation of large amount of Al_4C_3, a slightly higher TC of 273 W/mK was obtained. To reduce the generation of Al_4C_3, Tokunaga *et al*. [25] fabricated the unidirectional Al/CF composites with Al-Si alloy by hot extrusion process. The composite with 40 vol% of CFs exhibited 323 W/mK, which leads to 40% improvement in TC in comparison with pure Al. The above reports indicate that the orientation control of CFs in the matrix is seriously related to the thermal properties of Al/CF composites.

1.1.4 Al/graphite composites

Recently, Al/graphite composites have attracted much attention due to their high TC, low coefficients of thermal expansion, and low costs, which are considered to be

promising materials for heat sink applications. As is well known, graphite is highly anisotropic in both thermal and electrical conductivity, and the TC along its basal planes is much higher than that in c-axis. Besides, graphite is easy to react with liquid Al and form Al_4C_3 phase, which can deteriorate the TC of Al/graphite composites [26]. Thus, in order to prepare Al/graphite composites with a preferred orientation and avoid the reactions between Al and graphite, powder metallurgy route is considered to be one of the effective methods to fabricate Al/graphite composites. As a typical technique, hot pressing has been widely studied to fabricate Al/graphite composites in recent years. For example, Chen *et al*. [27] reported an extremely high TC value of 783 W/mK in hot-pressed Al/80 vol% graphite sample. Kurita *et al*. [28], Xue *et al*. [29], and Chamroune *et al.* [30] also obtained TC values of 460 W/mK, 735 W/mK, and 450 W/mK in Al/50 vol% graphite, Al/70 vol% graphite, and Al/50 vol% graphite samples, respectively. These high TC values are mainly attributed to high contents and good orientation of graphite. For example, the basal planes of the graphite are preferentially perpendicular to the hot-pressing direction. Although the hot-pressed Al/graphite composites showed such high TC values, hot pressing is still difficult to be used in mass production due to high costs.

1.2 Purpose of present work

In the present work, graphite and CFs were chosen as the second phases, which were incorporated into Al matrix, and a hot-extrusion technique was proposed to prepare Al/carbon composites. The purpose is to understand the relationships among processing conditions, densification behavior, microstructure, thermal and mechanical properties, thus to promote their industrial applications and contribute to enhance the

reliability and service life of electronic components.

1.3 Outline of this work

This work has focused on the fabrication and performance improvement of Al/carbon composites. Chapter 2 focused on the fabrication of Al/graphite composites by hot-extrusion technique. The effects of processing conditions such as graphite particle size, graphite content, and extrusion temperature on extrusion behavior, microstructure, texture, and TC were systematically investigated.

Chapter 3 clarified the effect of Al-Si alloy addition on microstructure, thermal conductivity (TC), coefficient of thermal expansion (CTE) and compressive strength of the extruded Al/graphite composites.

Chapter 4 focused on the fabrication of Al/carbon fibers (CFs) composites by hot-extrusion technique. The effects of processing conditions such as CFs size, CFs content, and extrusion temperature on microstructure, texture, and TC of the extruded Al/CFs composites were investigated.

Chapter 5 studied the effect of Ni-coating on microstructure, thermal and mechanical properties of SPSed Al/CFs composites. The optimum coating time, sintering pressure, sintering temperature, and sintering time were clarified.

Chapter 6 focused on the fabrication of Al/Ni-coated CFs composites by hot-extrusion technique. Microstructure, thermal and mechanical properties were investigated.

Finally, in Chapter 7, general conclusions and summary of this work, as well as some achievements pegged on this work are presented.

References

[1] C. Zweben: Advances in composite materials for thermal management materials in electronic applications. JOM. 50. 47-51 (1998).

[2] A. Luedtke: Thermal management materials for high-performance applications. Adv. Eng. Mater. 6. 142-144 (2004).

[3] S. Mallik, N. Ekere, C. Best and R. Bhatti: Investigation of thermal management materials for automotive electronic control units. Appl. Therm. Eng. 31. 355-362 (2011).

[4] H. Katsutani, S. Yamagata, I. Nakamura: History and furture development of heat spreader products. Sei. Technical. Review. 82. 76-82 (2016).

[5] X.H. Qu, L. Zhang, M. Wu, S.B. Ren: Review of metal matrix composites with high thermal conductivity for thermal management applications. Prog Nat Sci: Mater Int 21. 189-197 (2011).

[6] K. Mizuuchi, K. Inoue, Y. Agari: Trend of the development of metal-based heat dissipative materials. Microelectron. Reliab. 79. 5-19 (2017).

[7] S.S. Sidhu, S. Kumar, A. Batish: Metal matrix composites for thermal management: a review. Critical Reviews in Solid State and Materials Sciences. 0: 1-26 (2015).

[8] K. Shirvanimoghaddam, S.U. Hamim, M.K. Akbari, S.M. Fakhrhoseini, H. Khayyam. A.H. Pakseresht, E. Ghasali, M. Zabet, K.S. Munir, S. Jia, J.P. Davim, M. Naebe: Carbon fiber reinforced metal matrix composites: Fabrication processes and properties. Compos. Part. A. 92. 70-96 (2017).

[9] M.A. Occhionero, R.A. Hay, R.W. Adams, K.P. Fennessy, G. Sundberg: Aluminum silicon carbide (AlSiC) microprocessor lids and heat sinks for integrated thermal

management solutions. HDI and Systems Pacjaging. 1-5 (2000).

[10] C. Kawai: Effect of interfacial reaction on the thermal conductivity of Al–SiC composites with SiC dispersions. J. Am. Ceram. Soc. 84. 896-898 (2001).

[11] R. Arpon, J.M. Molina, R.A. Saravanan, C.G. ordovilla, E. Louis, J. Narciso: Thermal expansion behavior of aluminum/SiC composites with bimodal particle distributions. Acta. Materialia. 51. 3145-3156 (2003).

[12] Y. Xu, Y. Tanaka, M. Murata, K. Kamihira, Y. Isoda, K. Yagi: Thermal conductivity of unidirectionally aligned SiC whisker reinforced Al alloy matrix composite with interfacial thermal resistance. Mater. Trans. 46. 148-151 (2005).

[13] H. S. Lee, K.Y. Jeon, H.Y. Kim, and S. H. Hong: Fabrication process and the thermal properties of SiC/Al metal matrix composites for electronic packaging applications, J. Mater. Sci. 35. 6231–6236 (2000).

[14] J.M. Molina, J. Narciso, L. Weber, A. Mortensen and E. Louis: Thermal conductivity of Al–SiC composites with monomodal and bimodal particle size distribution. Mater. Sci. Eng. A. 480. 483-488 (2008).

[15] N. Chen, X.F. Pan, M.Y. Gu: Microstructure and physical properties of Al/diamond composite fabricated by pressureless infiltration. Mater. Sci. Technol. 25. 400-402 (2009).

[16] W.B. Johnson, B. Sonuparlak: Diamond/Al metal matrix composites formed by the pressure less metal infiltration process. J. Mater. Res. 8. 1169-1173 (1993).

[17] X. Liang, C. Jia, K. Chu, H. Chen, J. Nie, W. Gao: Thermal conductivity and microstructure of Al/diamond composites with Ti-coated diamond particles consolidated by spark plasma sintering. J. Compos. Mater. 46. 1127-1136 (2012).

[18] Z.Q. Tan, Z.Q. Li, G.L. Fan, Q Guo, X.Z. Kai, G. Ji, L.T. Zhang, D. Zhang: Enhanced thermal conductivity in diamond/aluminum composites with a tungsten interface nanolayer. Mater and Des. 47. 160–166 (2013).

[19] K. Mizuuchi, K. Inoue, Y. Agari. Y. Morisada, M. Sugioka, M. Tanaka, T. Takeuchi, M. Kawahara, Y. Makino: Thermal conductivity of diamond particle dispersed aluminum matrix composites fabricated in solid-liquid co-existent state by SPS. Compos. Part. B. 42. 1029-1034 (2011).

[20] K. Mizuuchi, K. Inoue, Y. Agari. Y. Morisada, M. Sugioka, M. Tanaka, T. Takeuchi, M. Kawahara, Y. Makino: Processing of diamond particle dispersed aluminum matrix composites in continuous solid-liquid co-existent state by SPS and their thermal properties. Compos. Part. B. 42. 825-831 (2011).

[21] S. R. Bakshi, V. Singh, S. Seal, A. Agarwal: Aluminum composite reinforced with multi-walled carbon nanotubes from plasma spraying of spray dried powders. Surf. Coat. Technol. 203. 1544–1554 (2009).

[22] T.T. Liu, X.B. He, Q. Liu: Effect of chromium carbide coating on thermal properties of short graphite fiber/Al composites. J. Mater. Sci. 49. 6705-6715 (2014).

[23] H. Kurita, E. Feuillet, T. Guillemet, J.M. Heintz, A. Kawasaki, J.F. Silvain: Simple fabrication and characterization of discontinuous carbon fiber reinforced aluminum matrix composite for lightweight heat sink applications. Acta metal. Sin (Engl. Let.). 27. 714-722 (2014).

[24] M. Lee, Y. Choi, K. Sugio, K. Matsugi, G. Sasaki: Effect of aluminum carbide on thermal conductivity of the unidirectional CF/Al composites fabricated by low pressure infiltration process. Compos. Sci. Technol. 97. 1-5 (2014).

[25] T. Tokunaga, K. Takahashi, M. Ohno, K. Sasaki, T. Imanishi, K. Matsuura:

Fabrication of carbon fiber oriented Al-based composites by hot extrusion and evaluation of their thermal conductivity. Mater. Tran. 58. 938-944 (2017).

[26] T. Etterab, P. Schulza, M. Weberb, J. Metzc, M. Wimmlerc, J. F.Lofflerb, P.J. Uggowitzerb: Aluminum carbide formation in interpenetrating graphite/aluminum composites. Mater. Sci. Eng. A. 448. 1-6 (2007).

[27] J.K. Chen, I.S. Huang: Thermal properties of aluminum-graphite composites by powder metallurgy. Compos. Part. B. 44. 698-703 (2013).

[28] H. Kurita, T. Miyazaki, A. Kawasaki, Y.F. Lu, J.F. Silvain: Interfacial microstructure of graphite flake reinforced aluminum matrix composites fabricated via hot pressing. Compos. Part. A. 73. 125-131 (2015).

[29] C. Xue, H. Bai, P.F. Tao, J.W. Wang, N. Jiang, S.L. Wang: Thermal conductivity and mechanical properties of flake graphite/Al composite with a SiC nano-layer on graphite surface. Mater. Des. 108. 250-258 (2016).

[30] N. Chamroune, D. Mereib, F. Delange, N. Caillault, Y.F. Lu, J.L. Grosseau-Poussard and J.F. Silvain: Effect of flake powder metallurgy on thermal conductivity of graphite flakes reinforced aluminum matrix composites. J. Mater. Sci. 53. 8180-8192 (2018).

Chapter 2   Fabrication of Al/graphite composites by hot-extrusion process

2.1 Introduction

As reported, hot pressing has been widely studied to fabricate Al/graphite composites as a typical technique in recent years. For example, Kurita *et al*. [1] reported that with addition of a small amount of Al-Si alloy in the Al matrix powder, an extremely high TC value of 460 W/mK can be obtained in a fully dense hot-pressed Al/50 vol% graphite sample. Chamroune *et al*. [2] investigated the effect of Al powders morphology on microstructure and TC of vacuum hot-pressed Al/graphite composites, and also obtained high TC values of 400-450 W/mK at a graphite content of 50 vol%. These high TC values are mainly attributed to high contents and good orientation of graphite. For example, the basal planes of the graphite are preferentially perpendicular to the hot-pressing direction. Although the hot-pressed Al/graphite composites showed such high TC values, their applications are still limited because hot pressing is difficult to be used in mass production.

As is well known, extrusion is a cost-effective processing technique in fabricating elongated products with various cross-sectional shapes. It can also be applied to form powders or hard-to-work materials, since heavy deformation can be achieved under a high hydrostatic pressure. Furthermore, it is possible to control the preferred orientation of grains during extrusion, especially for those materials with layered structure such as graphite. However, to the best of our knowledge, no research work has been reported to fabricate Al/graphite composites by extrusion process. In the present work, from the viewpoints of orientation control and mass production, a hot-extrusion technique was proposed to prepare Al/graphite composites. The objective was to examine the effects of

graphite size and content as well as extrusion temperature on extrusion behavior, microstructure, texture, and TC of the Al/graphite composites.

2.2 Experimental procedure

2.2.1 Starting materials

Pure Al powder (>99.9% purity, mean particle size of 30 µm) and natural graphite powders with mean particle sizes of 10, 60, and 250 µm were used as the starting materials, as shown in Fig. 2.1, the Al powder had an irregular shape, while the graphite powders exhibited either granular or flaky morphologies. In addition to these single-sized (monomodal) graphite powders, a bimodal powder, prepared from coarse (250 µm) and fine (10 µm) powders with a mixing ratio of 3:1, was also used for the purpose of identifying the effect of particle size distributions of graphite on extrusion behavior, microstructure, and TC of Al/graphite composites.

2.2.2 Consolidation method

The Al and graphite powders with nominal compositions of 20, 40, and 60 vol% graphite were ball-milled for 12 h in ethanol. After drying, the Al/graphite powder mixture was pressed into a cylindrical green compact under a uniaxial pressure of 400 MPa, followed by vacuum-encapsulation in an Al can (Φ30mm×45mm) to obtain an extrusion billet. The conditions of uniaxial pressing are listed in Table 2.1. The extrusion was performed in a temperature range of 400-500 ˚C with an extrusion ratio of 14:1 (determined by the ratio of D_{billet}^2 and $D_{extruded\ sample}^2$, $D_{billet}\ and\ D_{extruded\ sample}$ are the diameters of billet and extruded sample, respectively) with a punch speed of 1 mm/min. The extrusion conditions are listed in

Table 2.2, and the schematic of hot-extrusion setup is showed in Fig. 2.2. Moreover, to improve the distribution and orientation of graphite in the composites and their TC values, some Al/40 vol% graphite (250 μm) green compacts were rotated 90° (Fig. 2.3) and then subjected to hot extrusion at 450 ˚C.
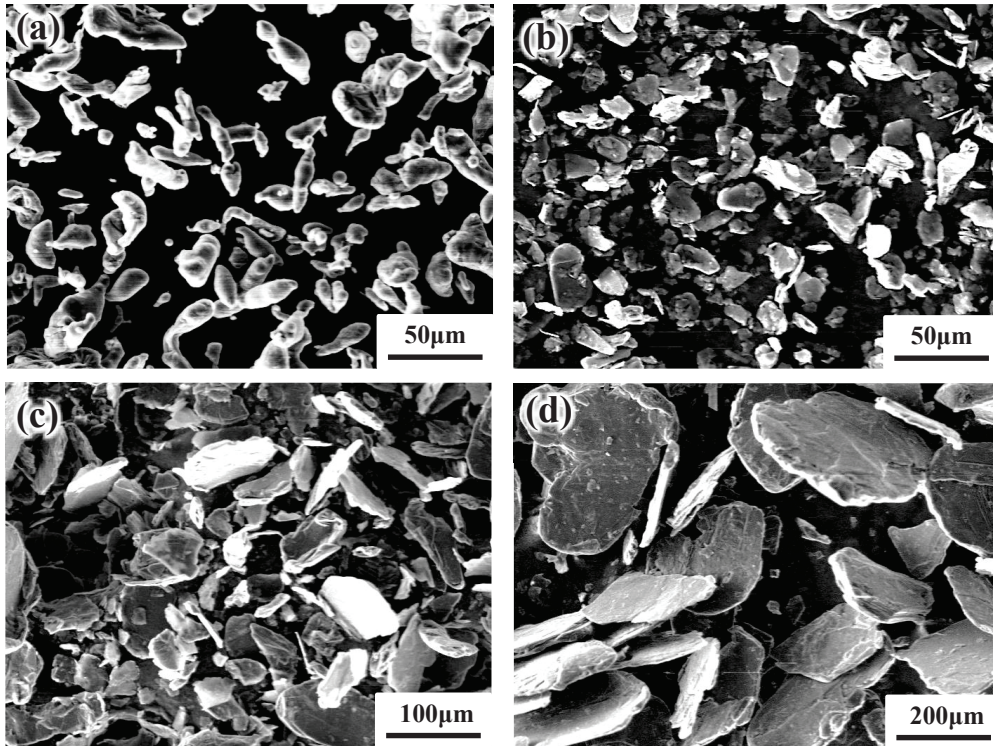

Fig. 2.1 SEM images of the starting materials used in the experiments. (a) Al powder (30 μm) and graphite powders with mean particle sizes of (b) 10 μm, (c) 60 μm, and (d) 250 μm.

Table 2.1 Conditions of uniaxial pressing

Atmosphere	Air
Lubricant	Stearic acid
Temperature	Room temperature
Pressure	400 MPa
Sizes of green compact	Φ20mm×25mm

Table 2.2 Conditions of hot extrusion

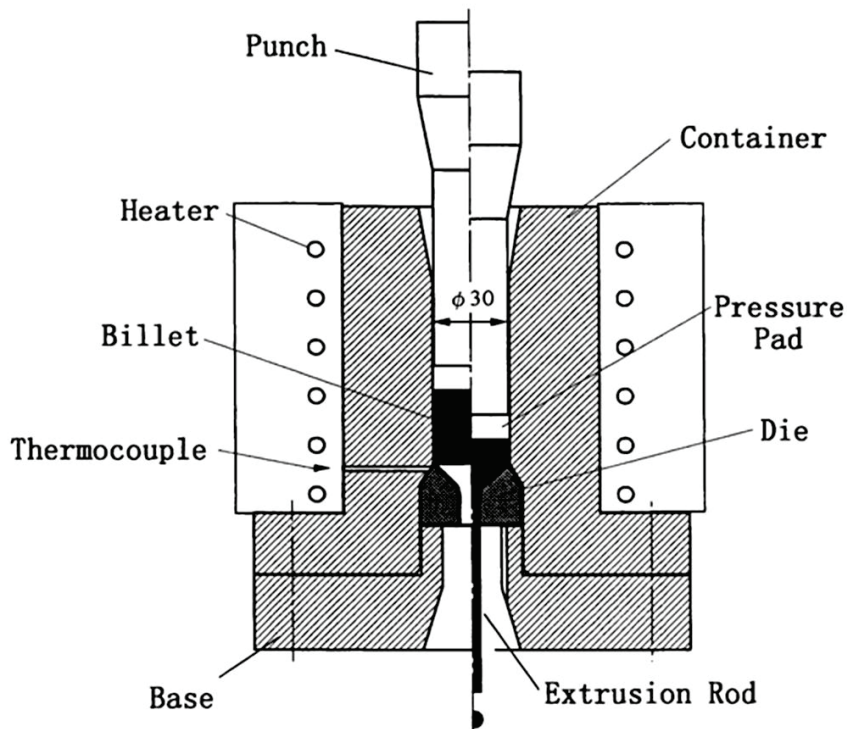|	
Extrusion billet	Cold-pressed compact
Atmosphere	Air
Extrusion temperature	400-500℃
Extrusion ratio	14
Extrusion speed	1mm/min

Fig. 2.2 Schematic of hot extrusion.

2.2.3 Characterization

The density of the extruded samples was determined by the Archimedes method. The density and relative density were calculated by the following equations, respectively.

$$\rho = \frac{m_a}{m_a - m_w} \times \rho_w \tag{2.1}$$

$$\rho_R = \frac{\rho}{\rho_T} \times 100 \tag{2.2}$$

17

where ρ and ρ_w are the density of the sample and water, respectively; m_a and m_w are the weight of sample in the air and water, respectively; ρ_R and ρ_T are the relative density and theoretical density of the sample, respectively.

Phase identification was performed by X-ray diffraction (XRD) with Cu Kα radiation. The orientation degree of the graphite in the Al/graphite extruded samples was estimated using the Lotgering method [3] which provides an orientation index deduced from XRD pattern for the oriented materials. The Lotgering factor f reflecting the degree of orientation by the following equation:

$$f = (P - P_0)/(1 - P_0) \tag{2.3}$$

where P denotes the ratio of the sum of the peak intensities corresponding to the preferred orientation axis $I(00l)$ to that of all diffraction peaks $I(hkl)$ in the extruded sample,

$$P = \sum I(00l)/\sum I(hkl) \tag{2.4}$$

P_0 is a reference value of P for a randomly oriented sample

$$P_0 = \sum I_0(00l)/\sum I_0(hkl) \tag{2.5}$$

The value of f varies between 0 and 1, where $f = 0$ corresponds to random orientation, while $f = 1$ corresponds to perfect orientation.

The microstructure was observed by scanning electron microscopy (SEM). Orientation imaging microscopy (OIM) analysis was performed using SEM equipped with an electron backscattered diffraction (EBSD) system. The TC was determined by measuring thermal diffusivity and specific heat at room temperature by using a laser flash apparatus (LFA457 Micro Flash, Netzsch, Germany).
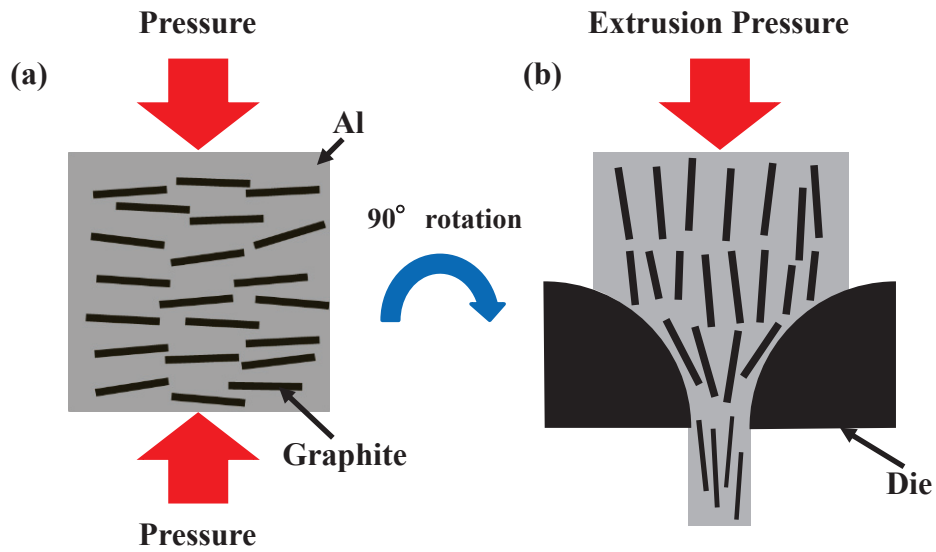
18

Fig. 2.3 Schematic views of (a) pressing and (b) extrusion of Al/graphite composites. The pressed green compact was rotated 90° and then extruded at 450 ˚C.

2.3 Results and discussion

2.3.1 Microstructure and thermal conductivity
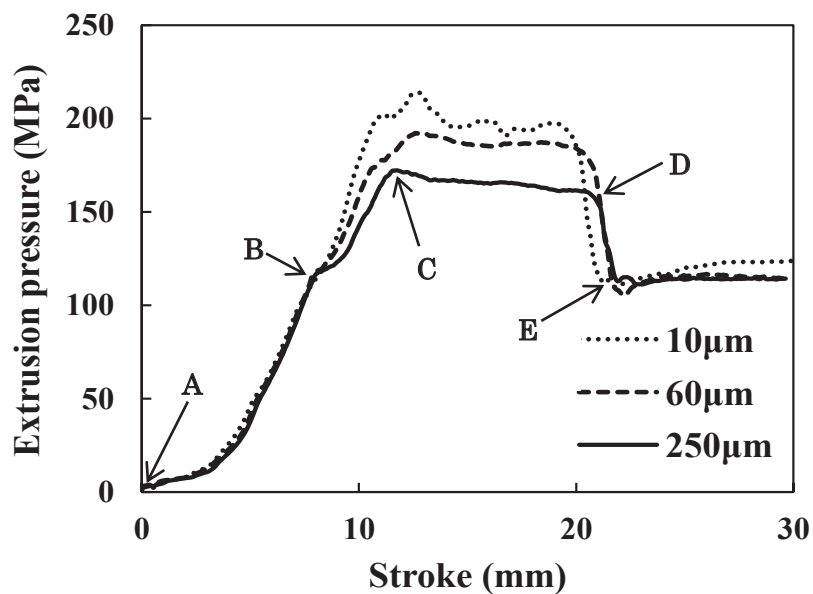
2.3.1.1 Effects of graphite size and content

Fig. 2.4 Extrusion pressure-stroke curves of 450 ˚C extruded-Al/40 vol% graphite samples extruded with different graphite sizes.

Fig. 2.4 shows the extrusion pressure *vs*. stroke curves of 450˚C extruded-Al/40 vol% graphite samples with different graphite sizes. In the initial stage up to point B shown in Fig. 2.4, the pressure gradually increased with extrusion stroke. This corresponds to the compaction of Al/graphite powder inside the Al can and plastic deformation of the Al can. At point B where the slope of the pressure *vs*. stroke curve became small, the Al in the front end of the billet started to be extruded out of the die. When the pressure reached point C, Al/graphite composite started to be formed with Al sheath on its surface layer. As the extrusion proceeded, the change of the pressure was not evident and the extrusion of the composite steadily continued up to point D. After the Al/graphite compact was completely extruded out of the die, only the residual Al sheath was subjected to the extrusion and thus the pressure level was sharply decreased (point E as shown in Fig. 2.4). In addition, with the incorporation of larger graphite particles, the extrusion pressure level became lower, which is considered as the result of the decrease in deformation resistance of the billet. Moreover, similar extrusion behavior was also found in the extrusion of the samples with different graphite contents. The effect of graphite content on extrusion pressure level was not remarkable.

Fig. 2.5 shows the appearances of the extruded Al/graphite (250 µm) samples with different graphite contents. The samples with lower graphite contents (20 vol% and 40 vol%) exhibited sound appearances, and no evident cracks, voids and other defects were observed, as shown in Fig. 2.5 (a) and (b). However, many defects were clearly observed on the surface of the sample with 60 vol% graphite (Fig. 2.5 (c)). This may result from severe aggregation of graphite due to a large amount of graphite and thus lead to poor formability. In addition, it has been confirmed that graphite size and extrusion temperature have a small effect on appearances of the extruded samples under

the experimental conditions used in the current work. These results suggest that graphite content is a major factor influencing the formability of Al/graphite composites in the extrusion temperature range of 400-500 ˚C.
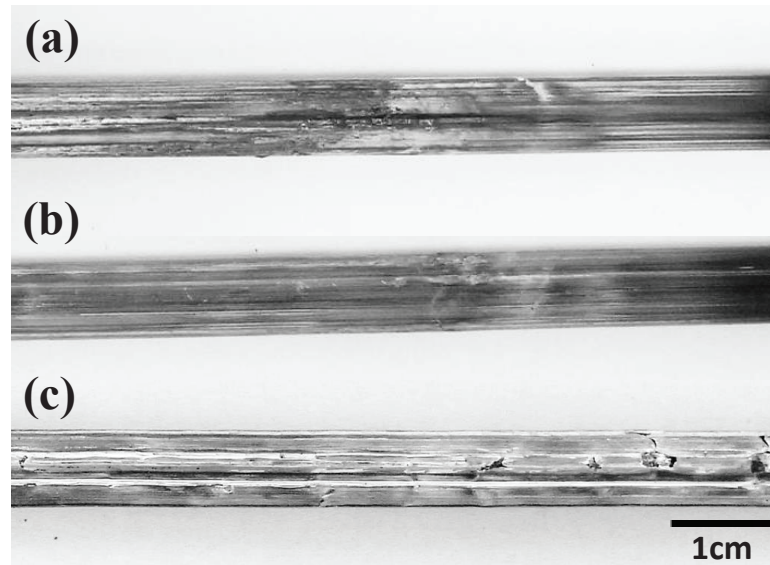

Fig. 2.5 Appearances of Al/graphite samples with (a) 20 vol%, (b) 40 vol%, and (c) 60 vol% graphite (250 μm). Extrusion temperature: 450 ˚C.

Fig. 2.6 shows the variations of relative density of the Al/graphite samples with different graphite particle sizes and contents extruded at 450 ˚C. The relative density of all the samples decreased with increasing the graphite content. This indicates that the presence of graphite inhibits the deformation of Al matrix and densification of the composites. For the monomodal graphite powders, as the particle size of graphite increased, the relative density became higher. It is believed that with the incorporation of larger graphite particles, the interfacial area between graphite and Al particles decreases. This results in a smaller inhibition effect of graphite on densification of the Al matrix during hot extrusion. Therefore, the extruded samples with larger graphite sizes showed higher density values, as shown in Fig. 2.6.
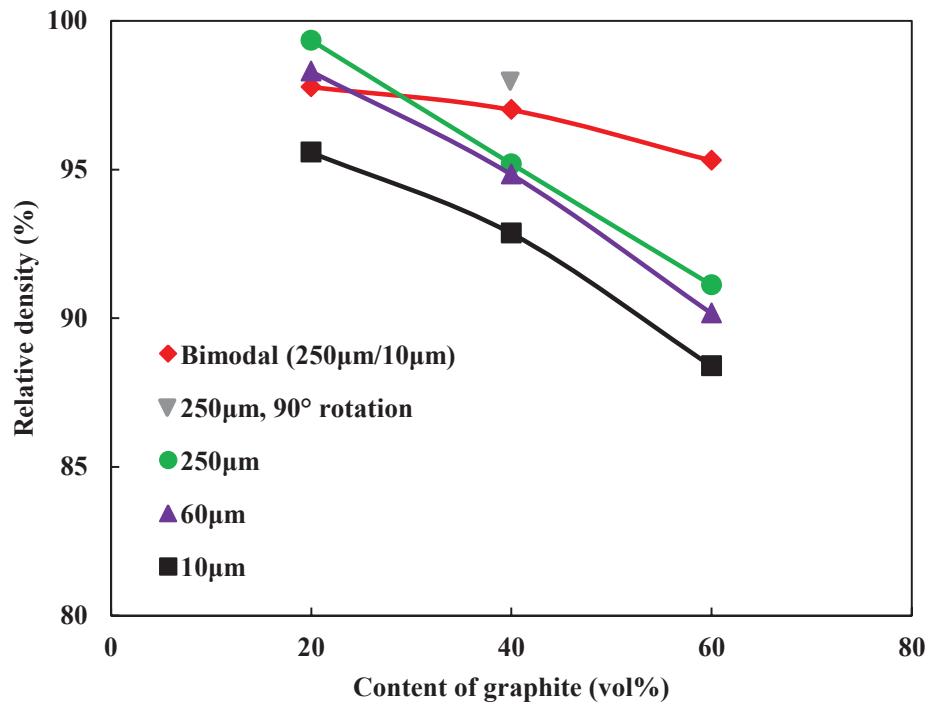
Fig. 2.6 Variations of the relative density on graphite content for Al/graphite samples. Extrusion temperature: 450 ˚C.

On the other hand, the 90°-rotated sample showed higher density value compared to the non-rotated sample. As illustrated in Fig. 2.3, the graphite flakes tend to be arranged in the direction perpendicular to the loading direction during pressing of Al/graphite powder mixture. After 90° rotation, further deformation of graphite along the extrusion direction occurs easily during subsequent hot-extrusion process. This is because the graphite distributions in the 90°-rotated billet are approximately parallel to the extrusion direction, which is also beneficial to reduction in breakage of graphite during the extrusion. These lead to enhancement in densification of the extruded sample.

With regard to the bimodal samples containing both 250 μm and 10 μm graphite powders, the relative density of the extruded samples did not decrease as remarkably as

those of the monomodal samples and exhibited higher values at graphite contents of 40 and 60 vol% (Fig. 2.6). It has been demonstrated that when the size ratio and volume fraction ratio of large to small particles reach certain values, respectively, the voids in mixed-sized sample can be obviously reduced compared to the single-sized samples [4], thus leading to increase in relative density. Similar improvements in density have also been found in Al/SiC composites with mixed-sized SiC particles [5-6].

Fig. 2.7 shows the SEM images (backscattered electron mode) on longitudinal sections of the monomodal samples with different graphite sizes and contents, where the white and dark regions correspond to Al and graphite, respectively. It was clearly observed that the graphite tended to be distributed along the extrusion direction in the extruded samples. This tendency seems to be weakened and the thickness of the deformed graphite became larger with increasing graphite content, which is attributed to aggregation of graphite. The preferred orientation of graphite along the extrusion direction in hot-extruded samples is believed to be associated with the shear deformation occurred during the extrusion, because graphite can be easily deformed along the basal plane due to its layered structure. In addition, as the graphite size decreased, both the length and thickness of the deformed graphite were reduced, and the graphite showed more homogeneous distributions within the Al matrix. In the case of the graphite particles with an average size of 10 μm, when the graphite content attained 60 vol% (Fig. 2.7(i)), it appears that the Al with a bright contrast is homogeneously distributed in the graphite matrix.
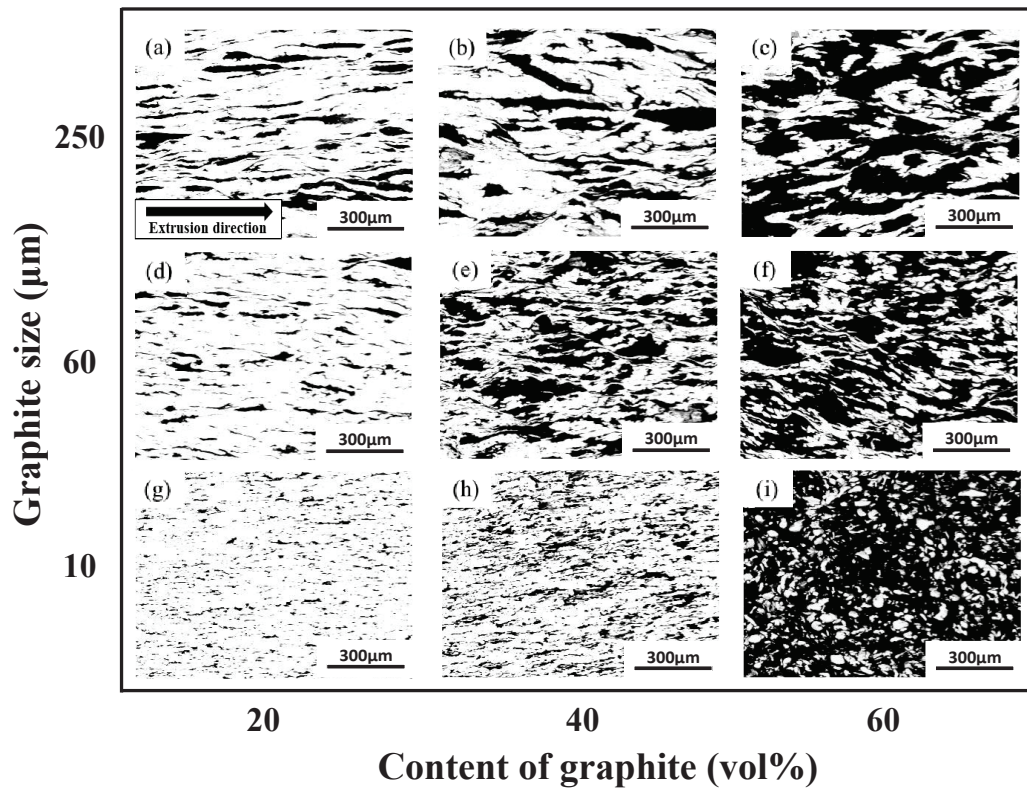
Fig. 2.7 SEM images on longitudinal sections of the hot-extruded monomodal samples with different graphite sizes and contents. Extrusion temperature: 450 ˚C.

Fig. 2.8 shows the SEM images on longitudinal sections of the bimodal samples with different graphite contents. Similar to the monomodal samples, the graphite was also distributed along the extrusion direction, and smaller graphite particles were uniformly dispersed in the Al matrix. With increasing the graphite content, more aggregation of graphite can also be observed in the hot-extruded samples. Since the average particle size (10 μm) of the small graphite powder is much smaller than those of both Al (30 μm) and large graphite powder (250 μm), it is assumed that the small graphite particles can effectively fill up the voids between Al/Al, Al/large graphite, and large graphite/graphite particles in the bimodal samples, thus resulting in higher relative density (Fig. 2.6).
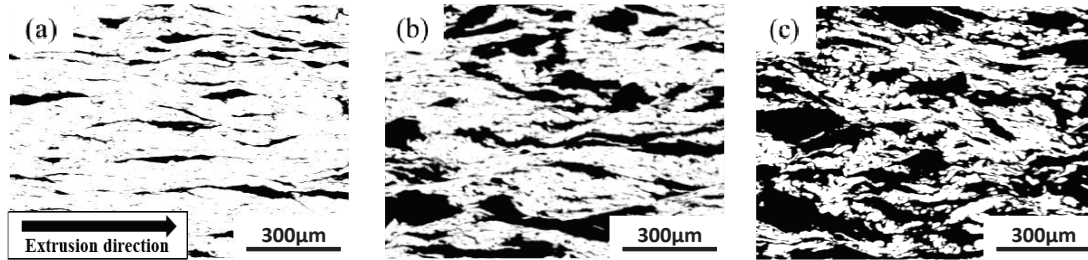
24

Fig. 2.8 SEM images on longitudinal sections of the hot-extruded bimodal samples with graphite content of (a) 20 vol%, (b) 40 vol%, and (c) 60 vol%. Extrusion temperature: 450 ˚C.

Fig. 2.9 shows the SEM image on the longitudinal section of the 90°-rotated Al/40 vol% graphite (250 μm) sample. In comparison with the non-rotated sample shown in Fig. 2.7 (e), it is obvious that the distribution of graphite along the extrusion direction became stronger in the 90°-rotated sample. Furthermore, the breakage of graphite was reduced evidently, which led to fewer Al/graphite interfaces.
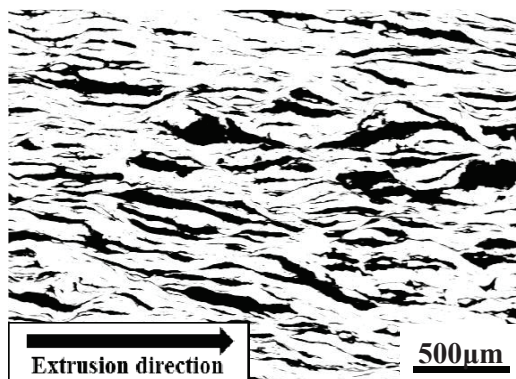

Fig. 2.9 SEM images on longitudinal sections of Al/40 vol% graphite (250 μm) samples extruded at 450 ˚C (90°-rotated sample).

Fig. 2.10 (a) shows the dependence of the Lotgering factor on graphite content and size. The extruded samples with a larger content of graphite exhibited smaller values of the Lotgering factor. It is considered that the severe aggregation of graphite at a larger content (Fig. 2.7) decreases the deformation degree of graphite along the basal plane. On the other hand, when the graphite particle size was increased from 10 to 60 μm, the

25

Lotgering factor increased slightly. This indicates that small-sized graphite particles are somewhat difficult to be deformed along the basal planes during extrusion compared to large-sized graphite. However, as the graphite particle size was further increased from 60 to 250 µm, the Lotgering factor remained almost unchanged. These results suggest that the particle size of graphite has a small influence on the orientation degree of the graphite in the extruded Al/graphite composites.

The dependence of the Lotgering factor on graphite content in the bimodal and 90°-rotated samples is illustrated in Fig. 2.10 (b). Similar to the monomodal samples shown in Fig. 2.10 (a), the bimodal samples showed a gradually reduced trend in the Lotgering factor with increasing the graphite content due to the aggregation of graphite. For the 90°-rotated sample, its Lotgering factor exhibited a higher value than the sample without rotation. This result indicates that the 90°-rotation of the pressed green compact can promote the shear deformation and preferred orientation of the graphite during hot-extrusion process (Fig. 2.3).
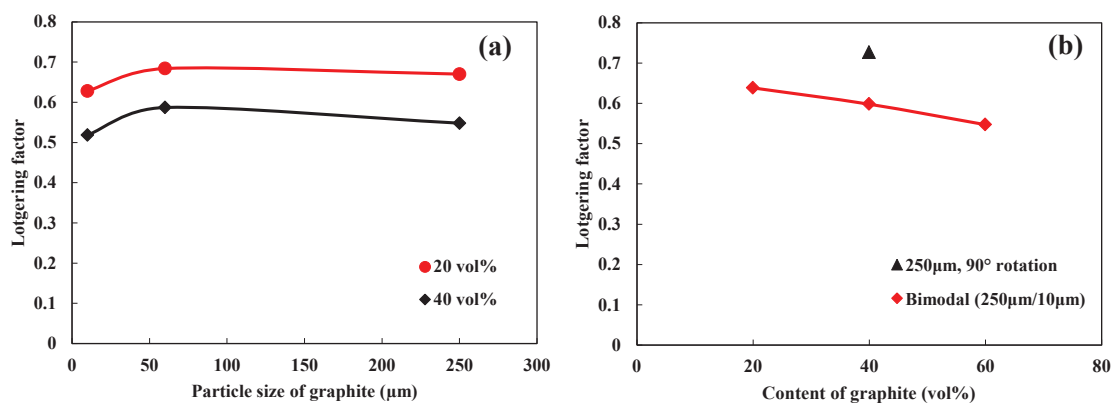

Fig. 2.10 Dependences of the Lotgering factor on (a) graphite content and particle size and (b) graphite content in the bimodal and 90°-rotated samples.

Fig. 2.11 shows the graphite content dependence of TC of the monomodal, bimodal, and 90°-rotated samples extruded at 450 ˚C. For the samples with the monomodal

graphite powders, as the graphite content increased, the TC increased gradually in Al/graphite (250 μm) samples, whereas the TC had small change in Al/graphite (60 μm) samples and decreased in Al/graphite (10 μm) samples. Generally, a larger graphite content leads to a higher TC value as indicated in Al/graphite (250 μm) samples in this work. However, the reductions in TC with increasing graphite content in 10μm- and 60μm-graphite incorporated samples are likely to be associated with lower relative density of the composites and more Al/graphite interfaces, as shown in Figs. 2.6 and 2.7, respectively. It should be noted that it was difficult to prepare Al/60 vol% graphite extruded samples for TC measurements due to their poor formability.

With regard to the bimodal samples, the TC increased with increasing graphite content and exhibited a higher value at 40 vol% compared to those of the monomodal samples. Although the small graphite particles with an average size of 10 μm result in more Al/graphite interfaces in the bimodal samples, the improvement in TC is believed to mainly arise from the significant increase in relative density (Fig. 2.6).

As for the 90°-rotated Al/40 vol% graphite (250 μm) sample, a higher TC value was obtained in comparison with the sample with exactly the same composition but without rotation. Such an enhancement in TC is considered to be associated with its higher relative density, fewer Al/graphite interfaces, and higher orientation degree $f_{(00l)}$ of the graphite as mentioned above.

On the other hand, the TC in the direction perpendicular to the extrusion direction was also measured. The results indicated that the TC values in the direction parallel to extrusion direction (//ED) were much larger than those perpendicular to the extrusion direction (⊥ED). For example, for Al/40 vol% graphite (60 μm) sample, the TC parallel to the extrusion direction was 2.6 times larger than that perpendicular to the extrusion
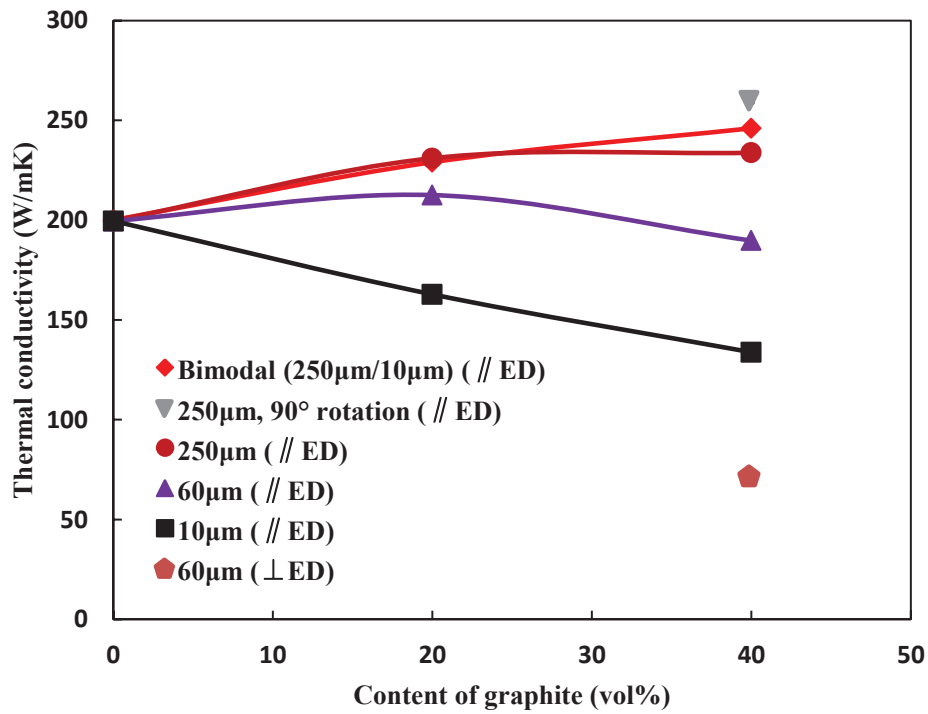
direction.

Fig. 2.11 Thermal conductivity of Al/graphite composites extruded at 450 ˚C (ED: extrusion direction).
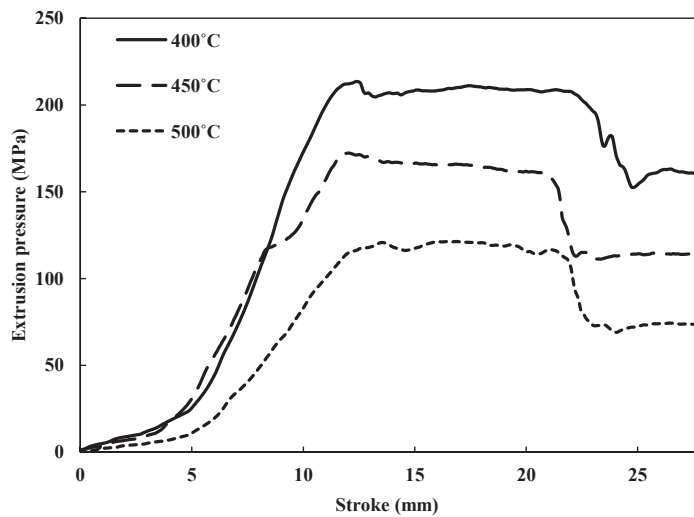
2.3.1.2 Effect of extrusion temperature

Fig. 2.12 Extrusion pressure-stroke curves of Al/40vol% graphite (250 μm) samples extruded at different temperatures.

Fig. 2.12 shows the extrusion pressure *vs*. stroke curves of Al/40 vol% graphite (250 μm) samples extruded at different temperatures. As the extrusion temperature increased, the extrusion pressure level decreased due to lower deformation resistance at a higher extrusion temperature. Moreover, it should be noticed that as the extrusion temperature varied, the appearance and relative density had small change.

Fig. 2.13 shows the SEM images of the Al/40 vol% graphite (250 μm) samples extruded at different temperatures. It seems that the majority of graphite are distributed along the extrusion direction at 400 ˚C. With increasing the extrusion temperature, the aspect ratio of the graphite became smaller and its distribution along the extrusion direction became weaker. It has been reported that the mechanical properties of graphite are almost unchanged under 1000 ˚C [7], while the deformation resistance of Al rapidly decreases with increasing temperature, which can be easily found from the pressure levels at different temperatures shown in Fig. 2.12. Therefore, the changes in morphology and distribution of the graphite in Al/graphite composites with extrusion temperature are likely to be due to the difference in deformation resistance between Al and graphite. As the extrusion temperature increases, the deformation of the Al matrix occurs easily compared to graphite. As a result, the deformed graphite flakes exhibited smaller aspect ratios at a higher temperature.
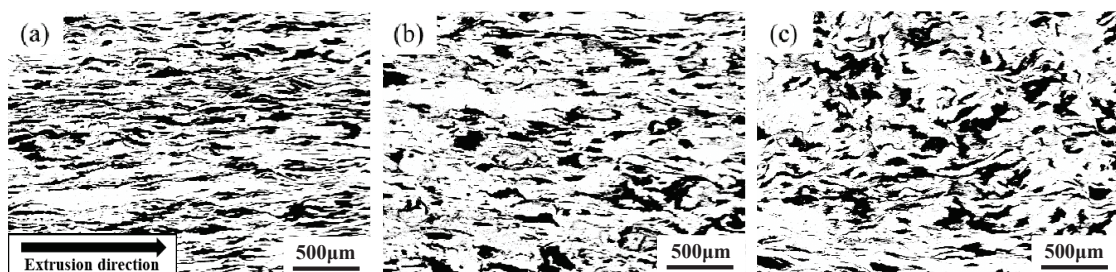

Fig. 2.13 SEM images on longitudinal sections of Al/40 vol% graphite (250 μm) samples extruded at (a) 400 ˚C, (b) 450 ˚C, and (c) 500 ˚C.

Fig. 2.14 illustrates the quantitative results of the aspect ratios of graphite in Al/40 vol% graphite (250 μm) samples, which were measured from the SEM images. With increasing the extrusion temperature, the average aspect ratio of graphite decreased from about 13 to 4.

The effect of extrusion temperature on the microstructure of hot-extruded Al/40 vol% graphite samples was also examined by EBSD. Fig. 2.15 shows the inverse pole figure (IPF) maps of Al matrix on longitudinal sections of the composites extruded at different temperatures. It should be noted that the dark regions in Fig. 2.15 correspond to graphite and its IPF maps are not included in the figure because the confidence index (CI) values of graphite are very small. The extremely small CI value of the graphite may be associated with its uneven surfaces in polished Al/graphite samples because Al and graphite have different hardness values and graphite easily drops out during polishing. All the maps in Fig. 2.15 have CI values of >0.1, indicating that the IPF maps shown in Fig. 2.15 represent the orientations of the Al matrix [8, 9].
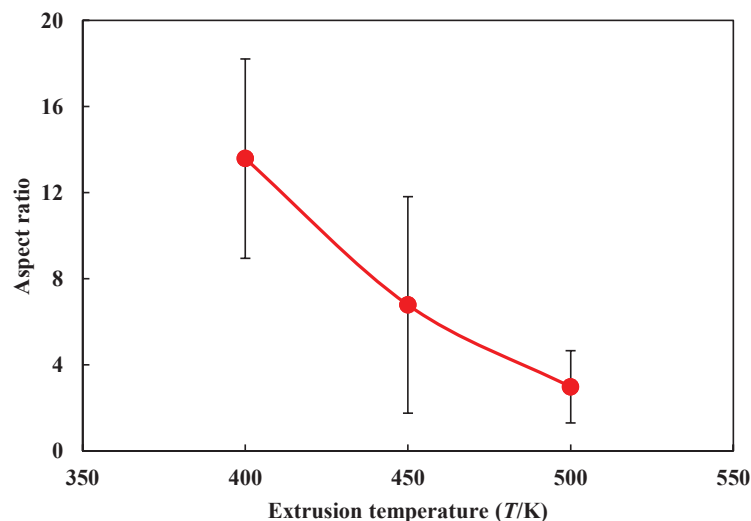

Fig. 2.14 Measured aspect ratios of graphite in Al/40 vol% graphite (250 μm) samples extruded at (a) 400 ˚C, (b) 450 ˚C, and (c) 500 ˚C.

As shown in Fig. 2.15, most of the Al grains were elongated along the extrusion direction in the extruded samples. As the extrusion temperature increased, grain growth occurred. The average grain sizes of the Al matrix were measured as 9.79 μm, 10.96 μm, and 11.36 μm at 400 ˚C, 450 ˚C, and 500 ˚C, respectively. In addition, from the IPF maps shown in Fig. 2.15, one of the main textures of the Al matrix on longitudinal sections arises from {111}, which is in agreement with the texture of hot-extruded commercial pure Al as reported by Bieda *et al.* [10].
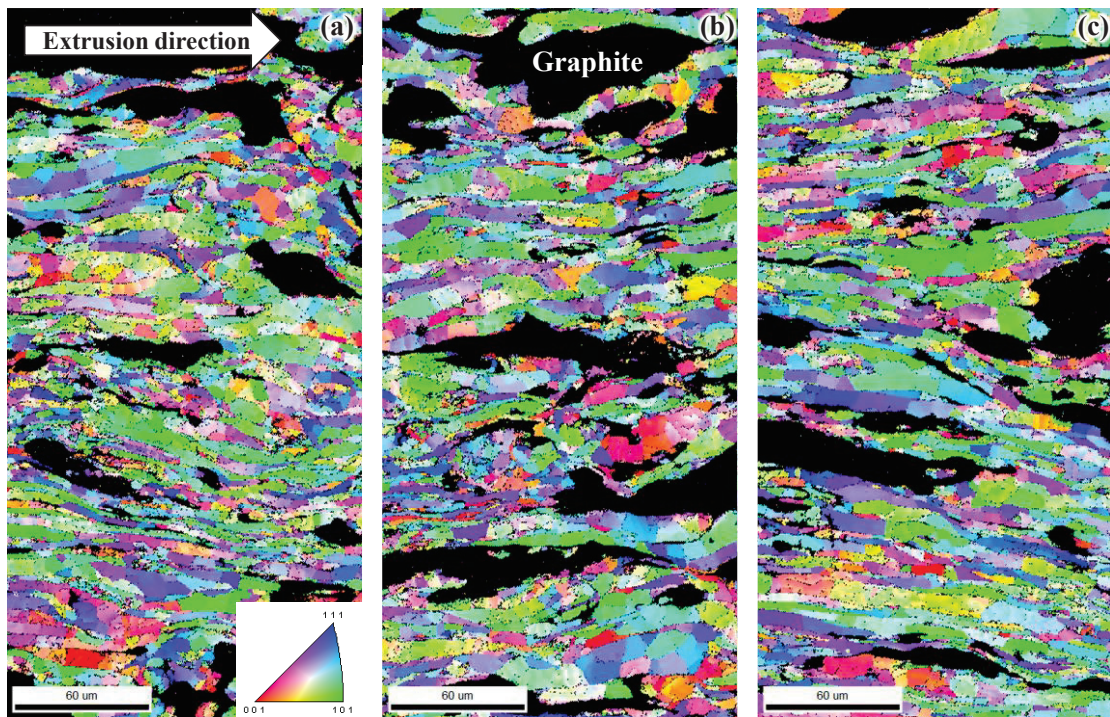

Fig. 2.15 Inverse pole figure (IPF) maps on longitudinal sections of Al/40 vol% graphite (250 μm) samples extruded at (a) 400 ˚C, (b) 450 ˚C, and (c) 500 ˚C.

To further examine the textures of the Al matrix, the {111} and {101} pole figures on longitudinal sections of the 450 ˚C-extruded samples are shown in Fig. 2.16. From the {111} pole figure, it is clear that the positions of two strong pole intensities fitted well with the extrusion direction. Furthermore, the {101} pole figure exhibited a typical

pole figure as seen in a {111} fiber texture [10]. This demonstrates again that the Al matrix showed {111} texture on the longitudinal sections of the extruded samples.
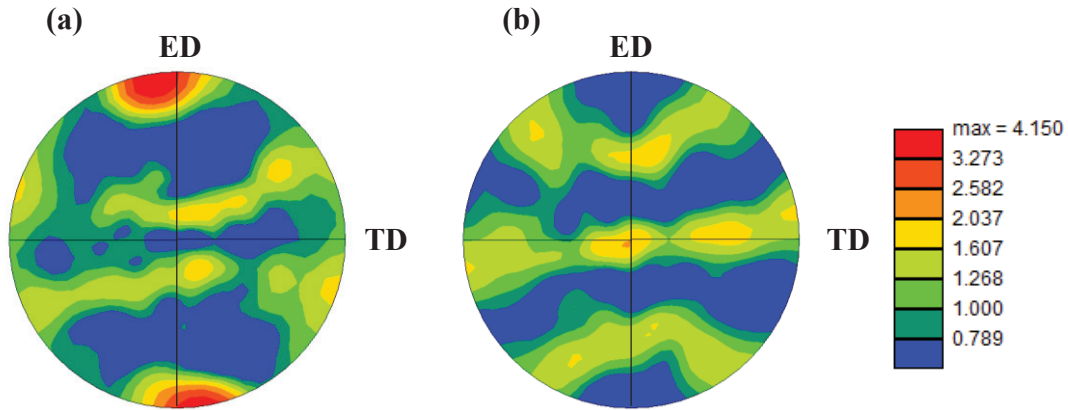

Fig. 2.16 (a) {111} and (b) {101} pole figures on longitudinal sections of the 450 ˚C-extruded Al/40 vol% graphite (250 μm) sample.

As an example, Fig. 2.17 (a) illustrates the XRD patterns on longitudinal and transverse sections of Al/40 vol% graphite samples extruded at 450 ˚C and 500 ˚C. The two patterns on longitudinal sections at 450 ˚C and 500 ˚C are similar to each other, where the (00l) basal planes of graphite (*e.g.*, (002) and (004)) as well as (111) peak of Al showed large diffraction intensities on the sections parallel to the extrusion direction. Furthermore, in comparison with the patterns on longitudinal sections, the pattern on transverse section showed weaker diffraction intensities on (00l) basal planes of graphite and stronger diffraction intensities of Al, especially on (111) plane. These results further suggest that the (00l) basal planes of graphite are preferentially orientated to the extrusion direction in hot-extruded Al/graphite composites. Besides, no peaks of aluminum carbide (Al$_4$C$_3$) phase were detected in the extruded samples, but further detailed TEM observations at Al/graphite interfaces are necessary.

In order to quantitatively evaluate the orientation degree of the graphite in hot-extruded Al/40 vol% graphite samples, the orientation factor $f_{(00l)}$ of the graphite

32

was calculated by the Lotgering method from the XRD data, and the dependence of the Lotgering factor on extrusion temperature is shown in Fig. 2.17 (b). With the increase in extrusion temperature, the Lotgering factor slightly decreased from 400 ˚C to 450 ˚C, and then obviously decreased from 450 ˚C to 500 ˚C. The orientation evolution of the graphite is in good agreement with the graphite distributions along the extrusion direction shown in Fig. 2.13.
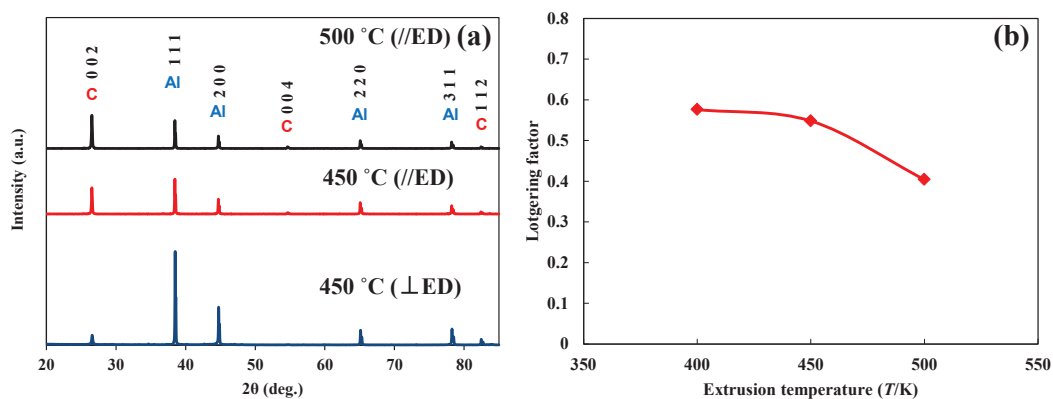

Fig. 2.17 (a) XRD patterns on longitudinal sections of Al/40 vol% graphite (250 μm) samples extruded at 450 ˚C and 500 ˚C and (b) dependence of the Lotgering factor of graphite on extrusion temperature.

Fig. 2.18 shows the thermal conductivity (TC) of hot-extruded Al/40 vol% graphite samples as a function of extrusion temperature. It is worth pointing out that the measuring direction of both thermal diffusivity and specific heat was parallel to the extrusion direction. As a reference, the TC value of a 450 ˚C-extruded pure Al sample was also plotted in Fig. 2.18. The TC value increased as the extrusion temperature increased from 400 to 450 ˚C. This is mainly attributed to the grain growth (Fig. 2.15) at a higher extrusion temperature, which causes reduction in scattering of phonons at grain boundaries. However, as the extrusion temperature further increased from 450 to 500 ˚C, the TC decreased and thus reached a peak at 450 ˚C. A lower TC value at 500 ˚C is

33

likely to be due to a significant reduction in orientation degree of graphite as mentioned previously (Fig. 2.17 (b)). Another possible reason is the formation of Al_4C_3 compound during the hot extrusion at 500 ˚C although Al_4C_3 cannot be detected in XRD analysis. The above results suggest that grain boundaries play a dominant role in thermal conduction in the extrusion temperature range of 400-450 ˚C, whereas the orientation degree of the graphite becomes dominant at 450-500 ˚C.
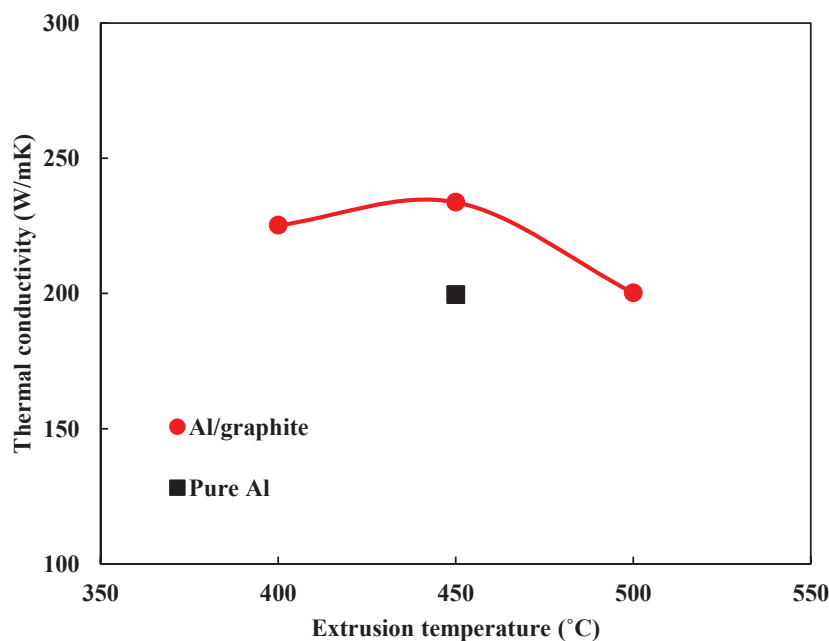

Fig. 2.18 Thermal conductivity of Al/40 vol% graphite (250 μm) samples as a function of extrusion temperature.

From the above results, it can be found that the hot-extruded Al/graphite composites exhibited relatively lower TC in comparison with the hot-pressed samples (~450 W/mK). This is presumably attributed to larger interfacial thermal resistance, because the deformation and breakage of graphite flakes occur during hot extrusion, resulting in larger Al/graphite interfaces. Nevertheless, the hot-extruded Al/graphite composites showed excellent workability and remarkable anisotropic behavior in TC. Furthermore, we have attempted to reduce Al/graphite interfacial thermal resistance and

34

improve the density of the composites, which result in a significant enhancement in TC of the extruded Al/graphite composites (the results will be shown in chapter 3). Accordingly, hot-extrusion process is believed to be a promising technique to fabricate Al/graphite composites for thermal management applications.

2.4 Conclusions

(1) Sound and dense Al/graphite composites with relative density of > 95% were successfully fabricated by a hot-extrusion process under the conditions of extrusion temperatures ranging from 400 ˚C to 500 ˚C and graphite contents of $\leq$ 40 vol%.

(2) The microstructural observations showed that graphite was mainly distributed along the extrusion direction. The (00*l*) basal planes of the graphite in extruded composites exhibited preferred orientation on longitudinal sections parallel to the extrusion direction.

(3) The preferred orientation of graphite resulted in an anisotropy of TC in the extruded samples. The TC in the extrusion direction was higher than that in the direction perpendicular to the extrusion direction.

(4) The incorporation of large-sized graphite flakes is beneficial to the improvement in TC of extruded Al/graphite composites. In comparison with monomodal graphite powder, the utilization of bimodal graphite powder is beneficial to the enhancement of both relative density and TC of the Al/graphite composites, although the incorporation of small graphite particles causes more Al/graphite interfaces.

(5) The 90°-rotated sample exhibited higher TC (259 W/mK) due to its higher relative density, fewer Al/graphite interfaces, and higher orientation degree of the graphite.

References

[1] H. Kurita, T. Miyazaki, A. Kawasaki, Y.F. Lu, J.F. Silvain: Interfacial microstructure of graphite flake reinforced aluminum matrix composites fabricated via hot pressing. Compos. Part. A. 73. 125-131 (2015).

[2] N. Chamroune, D. Mereib, F. Delange, N. Caillault, Y.F. Lu, J.L. Grosseau-Poussard and J.F. Silvain: Effect of flake powder metallurgy on thermal conductivity of graphite flakes reinforced aluminum matrix composites. J. Mater. Sci. 53. 8180-8192 (2018).

[3] F.K. Lotgering: Topotactical reactions with ferrimagnetic oxides having hexagon crystal structures—I. J. Inorg. Chem 9. 113-123 (1959).

[4] A.B. Yu, N. Standish, A. McLean: Porosity calculation of binary mixtures of nonspherical particles. J. Am. Ceram. Soc 76. 2813-2816 (1993).

[5] K. Mizuuchi, K. Inoueb, Y. Agaria, M. Sugioka, M. Tanaka, T. Takeuchi, J. Tani, M. Kawahara, Y. Makino, M. Ito: Bimodal and monomodal diamond particle effect on the thermal properties of diamond-particle-dispersed Al-matrix composite fabricated by SPS. Microelectron. Reliab. 54. 2463-2470 (2014).

[6] J.M. Molina, R.A. Saravanan, R. Arpon, C. García-Cordovilla, E. Louis, J. Narciso: Pressure infiltration of liquid aluminum into packed SiC particulate with a bimodal size distribution. Acta. Mater. 50. 247-257 (2002).

[7] D.P. Kim, Y. Suhng, M. Labes: Mechanical properties of pyrolytic graphite flakes. Carbon. 30. 729-737 (1992).

[8] D.P. Field: Recent advances in the application of orientation imaging. Ultramicroscopy. 67. 1-9 (1997).

[9] Z.L. Wang, T. Akao, T. Onda and Z.C. Chen: Microstructure and thermoelectric properties of Bi-Sb-Te bulk materials fabricated from rapidly solidified powders. Scr. Mater. 136. 111-114 (2017).

[10] M. Bieda, S. Boczkal, P. Koprowski, K. Sztwiertnia and K. Piela: Texture and microtexture of pure (6N) and commercially pure aluminum after deformation by extrusion with forward-backward rotating die (Kobo). Arch. Metall. Mater. 61. 461-468 (2016).

Chapter 3   Microstructure and thermal/mechanical properties of hot-extruded Al/graphite composites with Al-Si alloy addition

3.1 Introduction

In chapter 2, Al/graphite composites have been successfully fabricated by a hot-extrusion technique. The effects of processing conditions such as graphite particle size, content, and extrusion temperature on microstructure and TC have been clarified. The results showed that the extruded samples had an anisotropic TC and good workability. However, the enhancement of TC in extrusion direction was not so evident in comparison with pure Al, as a result of low density and high Al/graphite interfacial thermal resistance in the hot-extruded composites.

In order to simultaneously improve the thermal and mechanical properties of Al/graphite composites, in the present work, small amounts of Al-Si alloy powder were introduced into Al/graphite powder mixtures, followed by consolidation using spark plasma sintering (SPS) and hot-extrusion processes. As is well known, the melting point of Al-Si alloy is lower than that of pure Al. Therefore, when the sintering temperature was set between Al and Al-Si alloy, the solid phase of Al-Si alloy can change to liquid phase while Al cannot. With the help of the existence of melted Al-Si alloy during SPS, it is expected that the densification of Al/graphite composites and interfacial bonding between Al and graphite can be improved during subsequent hot extrusion. The objective of this work was to examine the effect of Al-Si alloy addition on densification behavior, microstructure, TC, CTE, and compressive strength of the extruded Al/graphite composites.

3.2 Experimental procedure

3.2.1 Starting materials

Pure Al powder (mean particle size of 30 μm), natural graphite powder (250 μm), and Al-12mass%Si alloy powder (<45 μm, melting point: 577 ˚C) were used as the starting materials. As shown in Fig. 3.1, the Al, graphite, and Al-12Si alloy powders exhibited irregular, flaky, and spherical morphologies, respectively.
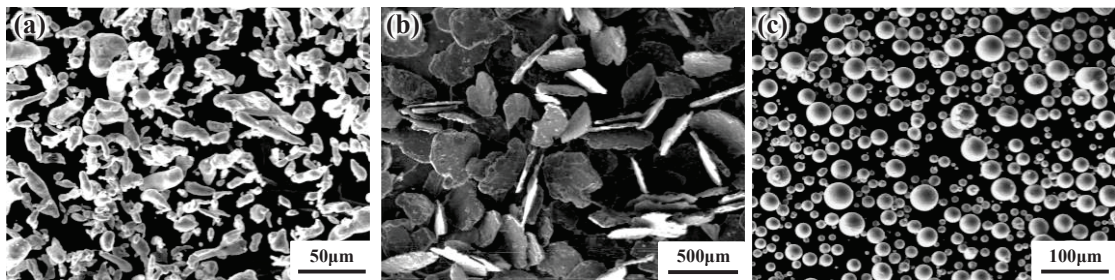

Fig. 3.1 SEM images of the starting materials used in the experiments. (a) Al powder (30 μm), (b) graphite flakes (250 μm), and (c) Al-12Si alloy powder (<45 μm).

3.2.2 Consolidation method

The raw powders with nominal compositions of Al/20-60 vol% graphite/3-12 vol% Al-Si alloy were ball-milled for 12 h in ethanol. After drying, the powder mixture was consolidated by SPS at 580 ˚C for 10 min under 40 MPa (the SPS conditions are listed in Table 3.1), followed by vacuum-encapsulation into an Al can to obtain a hot-extrusion billet. The extrusion was performed in a temperature range of 400-500 ˚C with an extrusion ratio of 14:1 and a punch speed of 1 mm/min (the extrusion conditions are listed in Table 3.2).

Table 3.1 Conditions of SPS.

Atmosphere	Vacuum
Heating rate	30 ˚C/min
Temperature	580 ˚C
Pressure	40 MPa
Sizes of green compact	Φ20mm×10mm

Table 3.2 Conditions of hot extrusion.

Extrusion billet	SPSed compact
Atmosphere	Air
Extrusion temperature	400-500℃
Extrusion ratio	14
Extrusion speed	1mm/min

3.2.3 Characterization

The density of the extruded samples was determined by the Archimedes method. Phase identification was performed by X-ray diffraction (XRD) with Cu Kα radiation. The microstructure was observed and analyzed by scanning electron microscopy (SEM), electron probe micro-analyzer (EPMA), and electron backscattered diffraction (EBSD).

The orientation degree of the graphite in the Al/graphite extruded samples was estimated using the Lotgering method [1] which provides an orientation index deduced from XRD pattern for the oriented materials. The Lotgering factor f reflecting the degree of orientation by the following equation:

$$f = (P - P_0)/(1 - P_0) \tag{3.1}$$

where P denotes the ratio of the sum of the peak intensities corresponding to the preferred orientation axis $I(00l)$ to that of all diffraction peaks $I(hkl)$ in the extruded sample,

$$P = \sum I(00l)/\sum I(hkl) \tag{3.2}$$

P_0 is a reference value of P for a randomly oriented sample

$$P_0 = \sum I_0(00l)/\sum I_0(hkl) \tag{3.3}$$

The value of f varies between 0 and 1, where $f = 0$ corresponds to random orientation, while $f = 1$ corresponds to perfect orientation.

With regard to the thermal and mechanical properties of hot-extruded samples, the TC was determined by measuring thermal diffusivity and specific heat at room temperature by using a laser flash apparatus (NETZSCH LFA457, Germany). The specimens for TC measurements were in the form of discs with a diameter of 6 mm and a thickness of 2 mm. The CTE was determined using a horizontal dilatometer (SEIKO TMA/SS6000, Japan) in a temperature range of 20-150 ˚C at a heating rate of 2 ˚C min^{-1}. The CTE was measured on cuboid samples with dimensions of 20 mm×5 mm×5 mm. In addition, compression tests were carried out using a universal testing machine (SHIMADZU SFL-50kNAG, Japan) with a compression rate of 1 mm/min. Cylindrical samples with dimensions of Φ6 mm×8 mm were used in the compression tests.

3.3 Results and discussion

3.3.1 Microstructure and thermal conductivity

3.3.1.1 Effect of extrusion temperature

In order to examine the effect of extrusion temperature on microstructure and TC of Al/graphite composites with Al-Si alloy addition, the composite samples with a

composition of Al/40 vol% graphite/6 vol% Al-Si alloy were prepared by hot extrusion in a temperature range of 400-500 ˚C. Fig. 3.2 shows the relative density of the hot-extruded samples as a function of extrusion temperature. For the purpose of comparison, the density values of hot-extruded Al/40% graphite samples without Al-Si alloy are also included in the figure. Obviously, the extruded samples with Al-Si alloy showed higher density values in comparison with those without Al-Si alloy. It is believed that the melted Al-Si alloy may infiltrate into the Al/graphite powder mixture during SPS, thus promoting the densification during sintering and density improvement in extruded samples. In addition, the extruded samples with and without Al-Si addition showed no noticeable variations in density with increasing the extrusion temperature. This indicates that extrusion temperature has a small influence on density values of the extruded composites in the extrusion temperature range used in the current experiments.
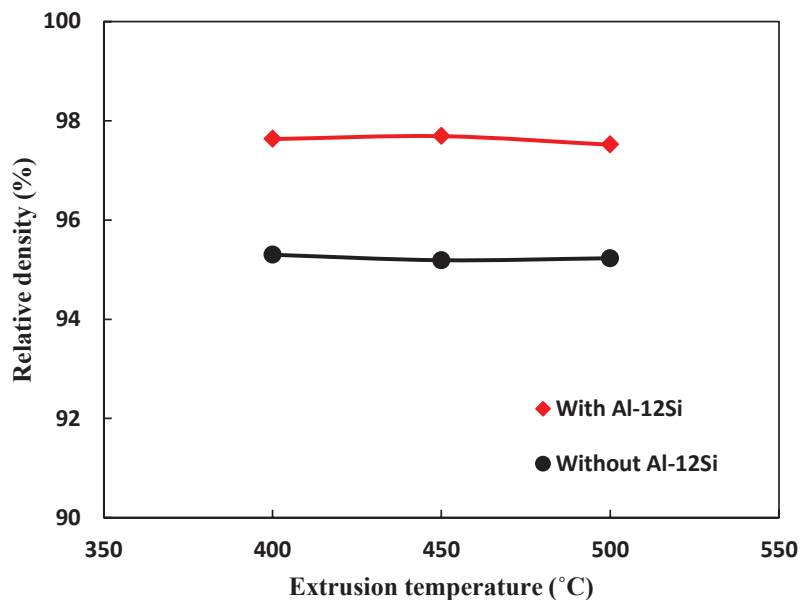

Fig. 3.2 Relative density of hot-extruded Al/40 vol% graphite samples with and without Al-Si alloy as a function of extrusion temperature.
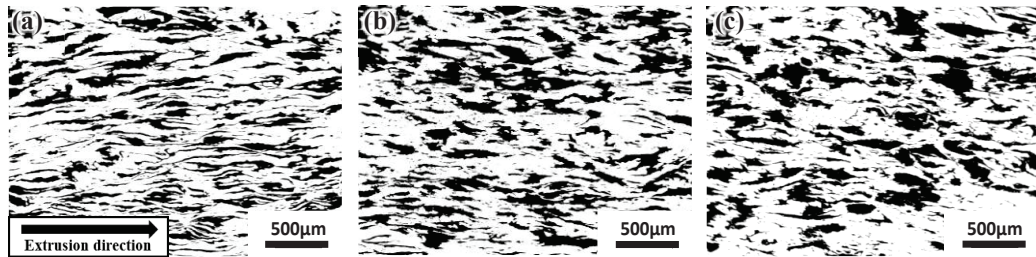
Fig. 3.3 SEM images on longitudinal sections of Al/40 vol% graphite/6 vol% Al-Si samples extruded at (a) 400 ˚C, (b) 450 ˚C, and (c) 500 ˚C.

Fig. 3.3 shows the SEM images (backscattered electron mode) on longitudinal sections of Al/40 vol% graphite/6 vol% Al-Si samples extruded at different temperatures. The white and dark regions shown in Fig. 3.3 correspond to Al and graphite, respectively. The graphite was mainly distributed along the extrusion direction in the extruded samples. As the extrusion temperature increased, the distribution of the graphite along the extrusion direction became weaker and its average aspect ratio was reduced. This phenomenon is related to the relative deformation resistances of Al and graphite at different temperatures. It is known that the mechanical properties of graphite are almost unchanged under 1000 ˚C [2], while the deformation resistance of Al rapidly decreases with increasing temperature. Accordingly, the deformed graphite flakes exhibited smaller aspect ratios at a higher temperature.

The XRD patterns on longitudinal sections of Al/40 vol% graphite/6 vol% Al-Si samples extruded at different temperatures are shown in Fig. 3.4 (a). Three patterns at 400 ˚C, 450 ˚C, and 500 ˚C are similar to each other. One strong diffraction peak at $2\theta = 26.5$˚ and two weak diffraction peaks at around 54.6˚ and 83.2˚ are attributed to (002), (004), and (112) planes of graphite, respectively. No peaks corresponding to aluminum carbide (Al_4C_3) phase were detected, indicating that no obvious reactions between graphite and Al or Al-Si alloy occur during SPS and hot-extrusion processes.

By using the integrated intensity values of the three diffraction peaks of graphite, the orientation factor $f_{(00l)}$ of graphite was quantitatively calculated by the Lotgering method [1]. In consistent with the orientation evolution of the graphite as shown in Fig. 3.3, the Lotgering factor (Fig. 3.4 (b)) of the extruded samples gradually decreased with increasing the extrusion temperature. As shown in Fig. 3.4 (b), the extruded samples with and without Al-Si alloy exhibited a similar change tendency with extrusion temperature, but the samples with Al-Si alloy showed higher Lotgering factors than those without Al-Si alloy. This may be related to the difference of preparation methods of the extrusion billets. In fact, the billets containing Al-Si alloy were consolidated by SPS, whereas those without Al-Si alloy were prepared by cold pressing. Since the SPSed samples had higher density values than the cold-pressed samples, the orientation degree of graphite in the SPSed samples is believed to be higher than that of the cold-pressed samples. Accordingly, it seems reasonable to consider that the Al/graphite samples consolidated by SPS and hot-extrusion processes have higher Lotgering factors.
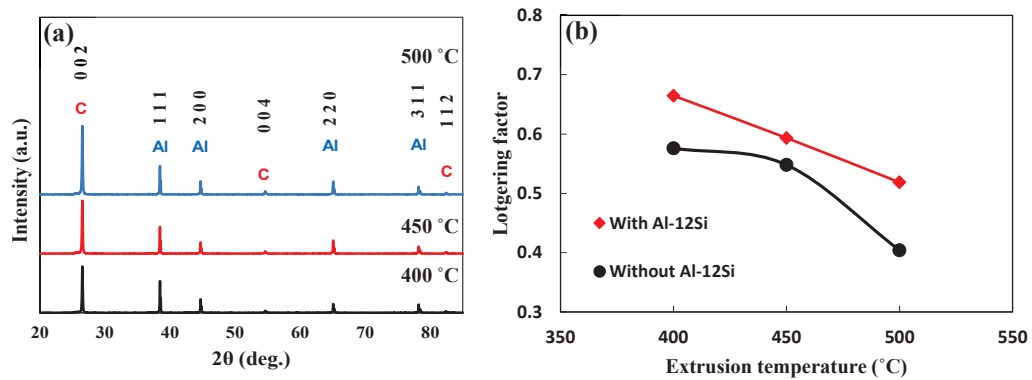

Fig. 3.4 (a) XRD patterns on longitudinal sections of Al/40 vol% graphite/ 6 vol% Al-Si samples extruded at 400 ˚C, 450 ˚C, and 500 ˚C and (b) Lotgering factor of graphite of Al/40 vol% graphite samples with and without Al-Si alloy as a function of extrusion temperature.

Fig. 3.5 shows the inverse pole figure (IPF) maps on longitudinal sections of Al/40

vol% graphite/6 vol% Al-Si samples extruded at different temperatures. Note that the dark regions in Fig. 3.5 correspond to graphite and its IPF maps are not included in the figure because the confidence index (CI) values of graphite are extremely small. All the maps in Fig. 3.5 have CI values of >0.1, accurately reflecting the orientations of the Al matrix. The majority of the Al grains were elongated along the extrusion direction, which is attributed to the heavy shear deformation during extrusion. As the extrusion temperature increased, grain growth occurred. The average grain sizes of the Al matrix were measured as 9.63 μm, 11.76 μm, and 12.31 μm at 400 ˚C, 450 ˚C, and 500 ˚C, respectively.
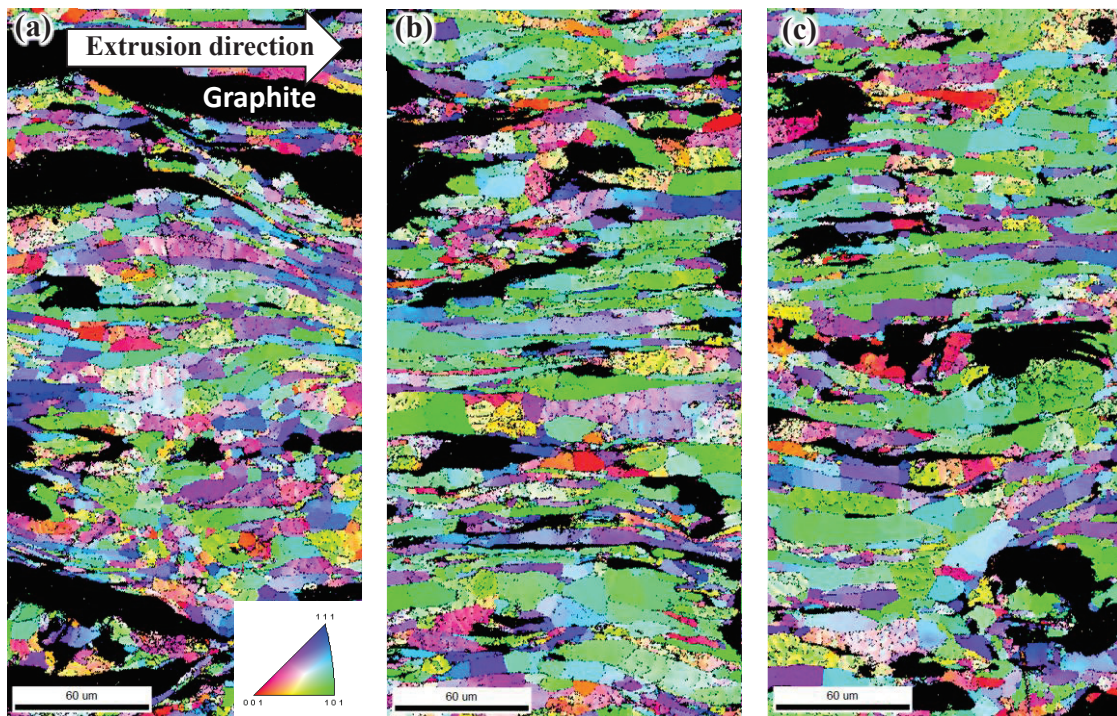

Fig. 3.5 Inverse pole figure (IPF) maps on longitudinal sections of Al/40 vol% graphite/6 vol% Al-Si samples extruded at (a) 400 ˚C, (b) 450 ˚C, and (c) 500 ˚C.

Fig. 3.6 shows the TC of Al/40 vol% graphite samples with and without Al-Si alloy as a function of extrusion temperature. As a reference, the TC value of a 450

˚C-extruded pure Al sample is also plotted in the figure. With the addition of Al-Si alloy, the TC values were significantly improved in comparison with those without Al-Si alloy. Although Al-Si alloy has a relatively low TC (~150 W/mK), the improved TC with addition of Al-Si alloy is mainly attributed to the enhancements in both relative density of the composites (Fig. 3.2) and orientation degree $f_{(00l)}$ of graphite (Fig. 3.4 (b)), as mentioned above. Similar to the samples without Al-Si alloy, the TC of the samples with Al-Si alloy increased slightly with increasing the extrusion temperature from 400 to 450 ˚C. This is likely to be due to the grain growth of Al matrix at a higher extrusion temperature (Fig. 3.5), which causes reduction in scattering of phonons at grain boundaries. As the extrusion temperature further increased from 450 to 500 ˚C, the samples with Al-Si alloy did not show decrease in TC like those without Al-Si alloy. This suggests that the influence of reduction in graphite orientation degree $f_{(00l)}$ is completely compensated by the contribution of grain growth of the Al matrix.
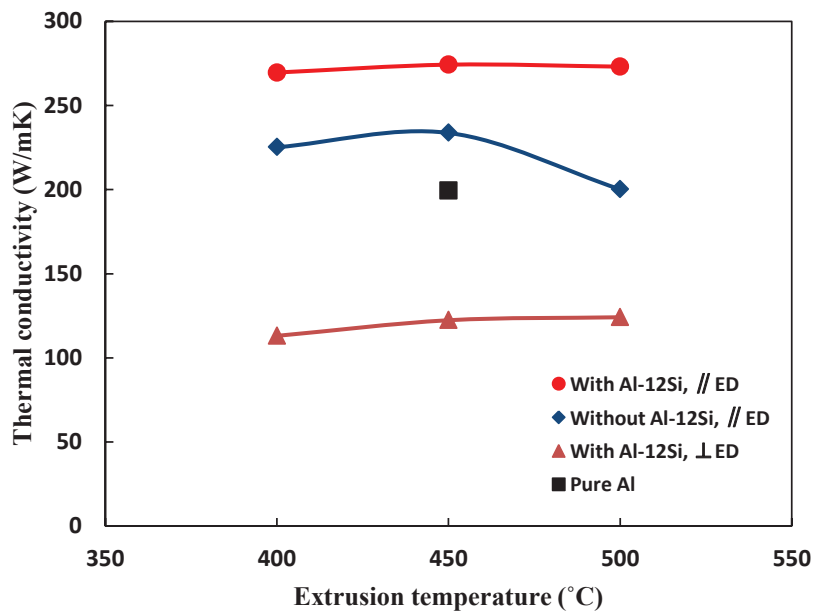

Fig. 3.6 Thermal conductivity of hot-extruded Al/40 vol% graphite samples with and without Al-Si alloy as a function of extrusion temperature (ED: extrusion direction).

In addition to the TC in the direction parallel to the extrusion direction (//ED), the TC in the direction perpendicular to the extrusion direction (⊥ED) was also measured. As shown in Fig. 3.6, the former is about 2.4 times higher than the latter, showing an anisotropic behavior in TC in the extruded samples. This is obviously the result of directional distribution of graphite in extruded Al/graphite composites because the TC along the basal planes is much higher than that in c-axis of graphite.

3.3.1.2 Effect of Al-Si alloy content

To examine the effect of Al-Si alloy content on microstructure and thermal conductivity, 3-12 vol% Al-Si alloy powder was incorporated into Al/40 vol% graphite samples which were extruded at 450 ˚C. Fig. 3.7 shows the relative density of the hot-extruded samples as a function of Al-Si alloy content. The addition of 3 % Al-Si alloy resulted in a significant increase in relative density, but it remained almost unchanged with further increases in Al-Si alloy content. Generally, the existence of more liquid phase can promote the densification during sintering and thus lead to a higher density value. The reason for small density changes with Al-Si alloy content is considered to be related to the loss of small amount of melted alloy, which flows out of the gap between the die and punch under the pressure applied during SPS.
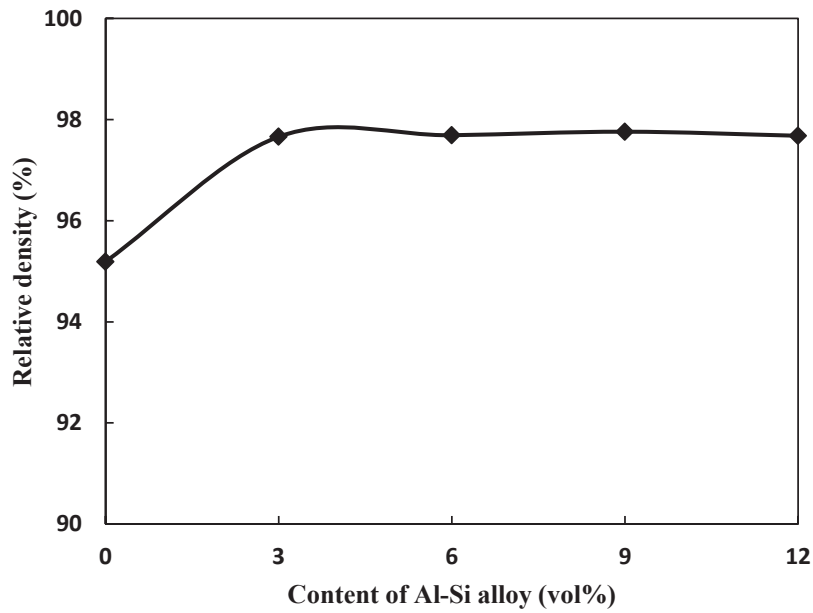
Fig. 3.7 Relative density of the hot-extruded Al/40 vol% graphite samples with different contents of Al-Si alloy, extruded at 450 ˚C.

Fig. 3.8 shows the SEM images on longitudinal sections of the 450 ˚C-extruded Al/40 vol% graphite samples with different contents of Al-Si alloy. Although the Al-Si alloy content was varied from 3% to 12%, no obvious change in graphite distribution can be observed. Furthermore, it has also been confirmed in our experiments that the content of Al-Si alloy has small effects on both orientation factor $f_{(00l)}$ of graphite and Al grain sizes in the extruded samples. Fig. 3.9 shows the elemental distributions of Al, C and Si in the 450 ˚C-extruded Al/40 vol% graphite samples with 6 vol% and 9 vol% Al-Si alloy. It should be note that CP is backscattered electron mode. As the Al-Si alloy content increased, more Si was distributed around Al/graphite interfaces, which is undoubtedly beneficial to the improvement of the interfacial bonding between Al and graphite and, hence, decrease in interfacial thermal resistance.
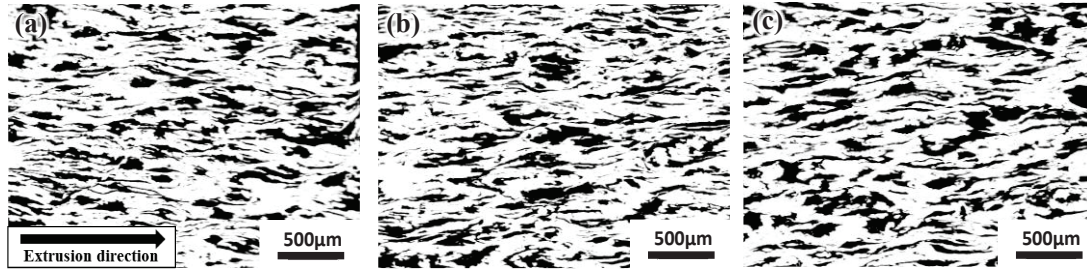
Fig. 3.8 SEM images on longitudinal sections of 450 ˚C-extruded Al/40 vol% graphite samples with Al-Si alloy contents of (a) 3 vol%, (b) 9 vol%, and (c) 12 vol%.
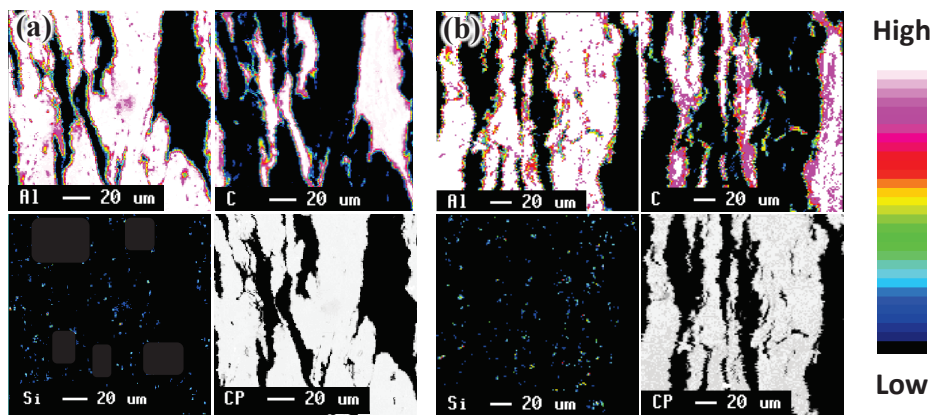

Fig. 3.9 Element mappings of 450 ˚C-extruded Al/40 vol% samples with Al-Si contents of (a) 6 vol% and (b) 9 vol%

Fig. 3.10 illustrates the TC of the 450 ˚C-extruded Al/40 vol% graphite samples as a function of Al-Si alloy content. As the alloy content increased, the TC increased remarkably and reached a peak at 9 %, followed by a reduction. It is believed that the significant enhancement of TC is attributed to (i) density increase of the composites, (ii) enhancement in orientation degree of graphite, and (iii) improvement in Al/graphite interfacial bonding, which gives rise to decrease in interfacial thermal resistance between Al and graphite. In addition, the reduction in TC from 9 % to 12 % may be the result of the addition of excessive Al-Si alloy, because Al-12Si alloy has a much lower TC value (~ 150 W/mK) than pure Al (~ 200 W/mK). Therefore, for hot-extruded Al/40vol% graphite composites, 9 % of Al-12Si alloy seems to be an optimum content,

49

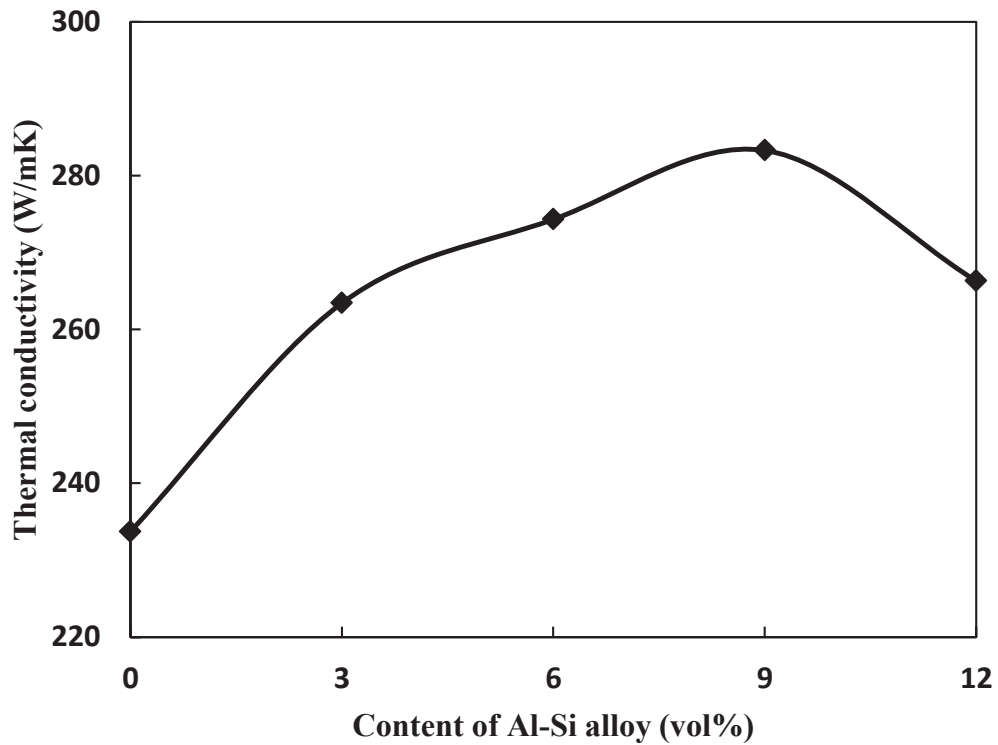which leads to good interfacial bonding and the highest TC (283 W/mK).

Fig. 3.10 Thermal conductivity of 450 ˚C-extruded Al/40 vol% graphite samples as a function of Al-Si alloy content.

3.3.1.3 Effect of graphite content

It is clear that graphite amount in Al/graphite composites is one of the most important factors that influence the microstructure, thermal (*e.g.*, TC and CTE) and mechanical properties (*e.g.*, strength) of the composites. On the basis of the above results, the Al/graphite samples containing 9 vol% Al-Si alloy and different contents (20-60 vol%) of graphite were prepared by the hot-extrusion process at 450 ˚C. Fig. 3.11 shows the variations of relative density of the hot-extruded Al/graphite samples on graphite content. The relative density gradually decreased as the graphite content increased. This results from the inhibition effect of graphite on plastic deformation of Al matrix and densification of the composites. When graphite content is ≤ 20 %, the

extruded samples exhibit almost the same density values whether Al-Si alloy is added or not. However, the effect of Al-Si alloy addition on density improvement of the composites became more and more important with further increasing graphite content. It is considered that a larger graphite content leads to more Al/graphite interfaces, thus the infiltration effect of melted Al-Si alloy can improve the density of composites more effectively by enhancing the Al/graphite interfacial bonding.

Fig. 3.12 shows the SEM images on longitudinal sections of the extruded samples with different graphite contents. As the graphite content increased, more aggregations of graphite were observed. For example, severe aggregations of graphite occurred (Fig. 12 (c)) at a graphite content of 60%. As a result, the orientation factor $f_{(00l)}$ of graphite decreased from 0.71 at 20% graphite to 0.55 at 60% graphite.
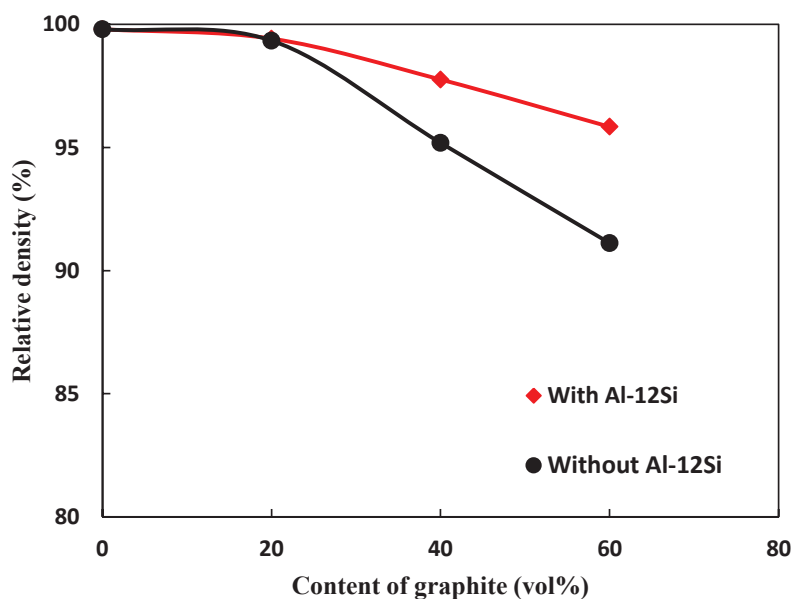

Fig. 3.11 Relative density of 450 ˚C-extruded Al/40 vol% graphite samples with and without Al-Si alloy as a function of graphite content.
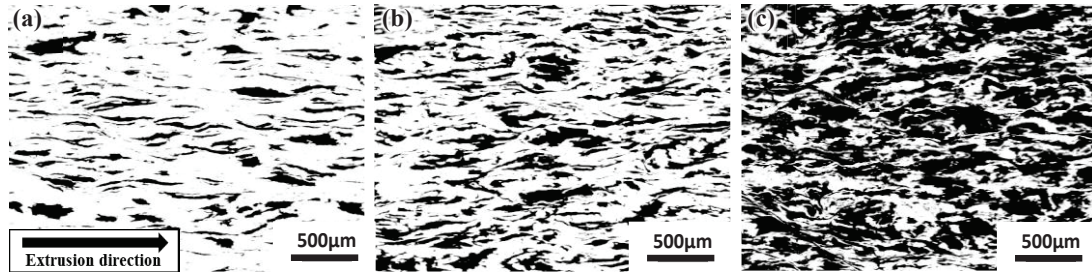
Fig. 3.12 SEM images on longitudinal sections of 450 ˚C-extruded Al/graphite samples containing 9 vol% Al-Si alloy with graphite contents of (a) 20 vol%, (b) 40 vol%, and (c) 60 vol%.

Fig. 3.13 shows the TC of the hot-extruded Al/graphite samples containing 9 % Al-Si alloy as a function of graphite content. At the graphite contents of 20 % and 40 %, the samples with Al-Si alloy showed TC values of 247 W/mK and 283 W/mK, respectively, which correspond to 7% and 21% enhancement in comparison with the samples without Al-Si alloy. As shown in Fig. 3.13, the TC exhibited a linear increase with graphite content until 40% graphite, followed by a slowly increasing trend at >40%. The slight increase in TC at 60% results from its lower relative density, lower orientation degree $f_{(00l)}$ of graphite, and more Al/graphite interfaces. A maximum TC value of 297 W/mK was obtained at 60 % graphite.
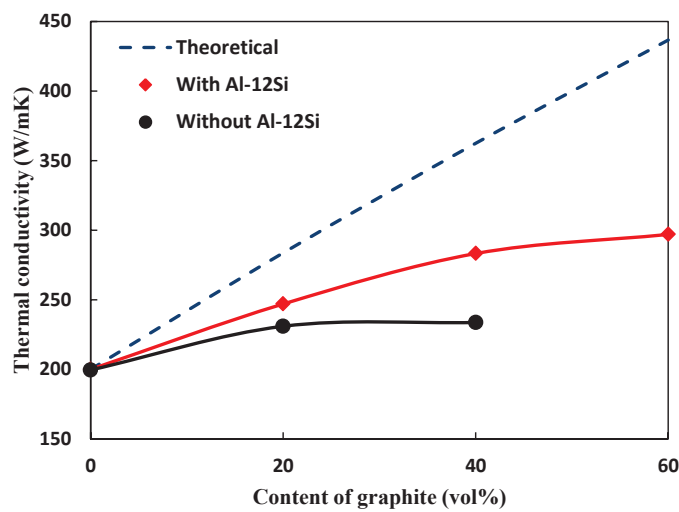

Fig. 3.13 Comparison of experimental TC data of 450 ˚C-extruded Al/graphite samples with theoretical prediction by the EMA model.

To better understand the effect of graphite content on the TC of the extruded Al/graphite composites, a theoretical prediction has been made by using an effective-medium approximation (EMA) model [3, 4]. It should be noted that the orientation, geometry, composition, and intrinsic TC of graphite, as well as interfacial thermal resistance between Al and graphite are main factors that should be taken into consideration. The general EMA formulations of TC in extrusion direction ($K_{c//ED}$) can be expressed as follows:

$$K_{c//ED} = K_m \frac{2+f_g[\beta_L(1-S_L)(1+cos^2\theta)+\beta_T(1-S_T)(1-cos^2\theta)]}{2-f_g[\beta_L S_L(1+cos^2\theta)+\beta_T S_T(1-cos^2\theta)]} \tag{3.4}$$

with

$$\beta_L = \frac{K_L-K_m}{K_m+S_L(K_L-K_m)} \tag{3.5}$$

$$\beta_T = \frac{K_T-K_m}{K_m+S_T(K_T-K_m)} \tag{3.6}$$

$$\langle cos^2\theta \rangle = \frac{\int \rho(\theta)cos^2\theta sin\theta d\theta}{\int \rho(\theta)sin\theta d\theta} \tag{3.7}$$

where f_g is the volume fraction of graphite. The subscripts L and T refer to the longitudinal (parallel to the basal planes) and the transverse (perpendicular to the basal planes) directions of the graphite flakes, respectively. S is the geometrical factor of the graphite flakes expressed as $S_L = \frac{\pi t}{4D}$ and $S_T = 1 - \frac{\pi t}{2D}$, where D and t represent the diameter and thickness of the graphite flakes, respectively. K_m, K_L, and K_T are the intrinsic TC values of Al matrix and graphite in longitudinal and transverse directions, respectively. $\langle cos^2\theta \rangle$ describes the statistical orientation of graphite, where θ is the angle between the basal planes of graphite and extrusion direction, and $\rho(\theta)$ describes the statistical distribution. In this study, for simplicity, graphite in all samples is assumed uniformly distributed, then $\rho(\theta) = 1$. According to Fig. 3.12, the range of θ

in the extruded samples can be assumed as $0°-30°$, thus $\langle cos^2\theta \rangle$ is calculated to be 0.872.

Concerning the effect of interfacial thermal resistance, graphite is considered to be coated with a very thin interfacial thermal barrier layer. Therefore, K_L and K_T in Eqs. (3.5) and (3.6) can be replaced by K_L^{eff} and K_T^{eff}, which means graphite having an effective TC, expressed as:

$$K_L^{eff} = \frac{K_L}{\frac{2K_L}{hD}+1} \qquad (3.8)$$

$$K_T^{eff} = \frac{K_T}{\frac{2K_T}{ht}+1} \qquad (3.9)$$

where h is the interfacial thermal conductance (i.e. the reciprocal of interfacial thermal resistance), calculated using the acoustic mismatch model (AMM) [5-7]:

$$h \cong \frac{1}{2}\rho_m C_m \frac{v_m^3}{v_i^2} \frac{\rho_m v_m \rho_g v_g}{(\rho_m v_m + \rho_g v_g)^2} \qquad (3.10)$$

where ρ, C, and v are the density, specific heat capacity and Debye phonon velocity, respectively, and subscripts m and g refer to the Al matrix and graphite, respectively. Assuming $\rho_m = 2700$ kg m^{-3}, $C_m = 895$ J kg^{-1} K^{-1}, $v_m = 3595$ m s^{-1}, and $\rho_g = 2260$ kg m^{-3}, $C_g = 710$ J kg^{-1} K^{-1}, $v_g = 14800$ m s^{-1} [8], and substituting these parameters into Eq. (3.10), we obtained $h = 4.47 \times 10^7$ W m^{-2} k^{-1}, which is close to the experimental result measured by Chen $et\ al$. (5×10^7 W m^{-2} k^{-1}) [9].

For the other parameters used in this research, K_L, K_T, K_m, D, and t were taken as 1000 W/mK, 10 W/mK, 200 W/mK, 250 μm, and 20 μm, respectively [10]. After substituting K_L, K_T, D, and t into Eqs. (3.8) and (3.9), the effective TC of graphite in two directions, K_L^{eff} and K_T^{eff}, were calculated to be 848.14 W/mK and 9.78 W/mK, respectively. Based on these calculated values, the theoretical TC value predicted by EMA model is shown in Fig. 3.13 (dashed line).

It is obvious that the theoretically predicted TC shows much higher values compared to the experimental data. This implies that there is still much potential for further enhancing the TC values of extruded Al/graphite composites. The large discrepancies between the theoretical and experimental TC values are considered to be attributed to the following two reasons. (i) The deformation and breakage of graphite flakes occurred during hot extrusion may result in more damages in graphite and larger Al/graphite interfaces, thus leading to relatively lower values of the experimental TC. (ii) The theoretical prediction might be overestimated, because the EMA model ignores the effects of pores, aggregations of graphite, and inter-particle multiple scattering in Al matrix.

3.3.2 Coefficient of thermal expansion

Fig. 3.14 shows the variations of CTE (measured in the extrusion direction) of the hot-extruded Al/graphite samples on graphite content. The addition of graphite in Al matrix caused significant reductions in CTE in the extruded samples with and without Al-Si alloy addition. This is obviously attributed to the negative CTE value of the graphite in the direction parallel to the basal planes (-1.0 ppm/K [11]). Furthermore, the samples containing Al-Si alloy showed lower CTE values than those without Al-Si alloy, further indicating good Al/graphite interfacial bonding. As shown in Fig. 3.14, when 60% graphite was added into Al, the CTE value of the extruded Al/60% graphite/9 % Al-Si sample was reduced to 7.95 ppm/K from 26 ppm/K of pure Al. Besides, although it is difficult to measure the CTE values in the direction perpendicular to the extrusion direction due to limited sizes of the extruded samples, it is reasonable to assume that the CTE values in the direction perpendicular to the extrusion direction are larger than those

55

in the direction parallel to the extrusion direction, because of higher CTE value of graphite in c-axis (28.0 ppm/K [11]).
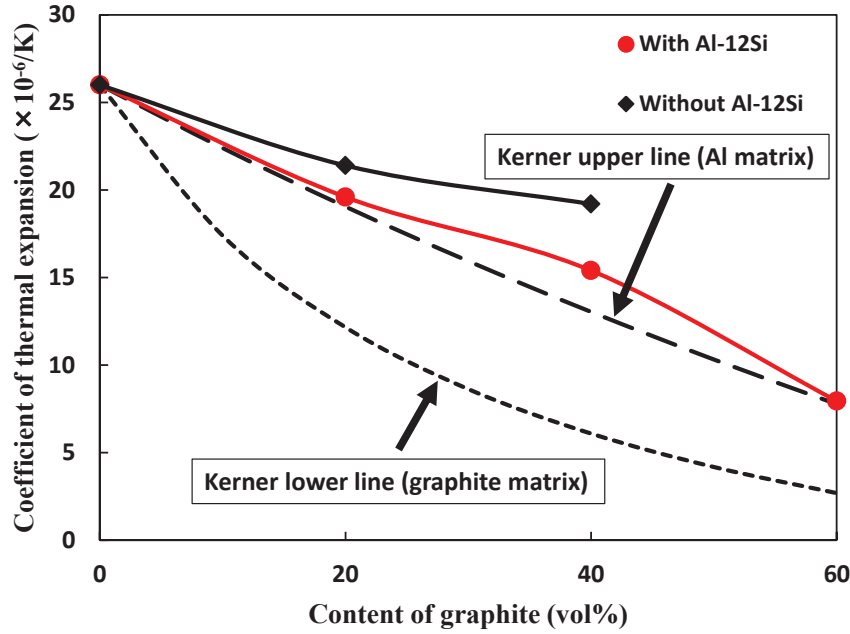

Fig. 3.14 Comparison of experimental CTE data of 450 ˚C-extruded Al/graphite samples with theoretical prediction by the Kerner model.

On the other hand, the theoretical CTE values of the extruded Al/graphite composites have been estimated by the Kerner model [12] using the following equation:

$$\alpha_c = \alpha_1 + V_2(\alpha_2 - \alpha_1) \times \frac{B_1(3B_2+4G_1)^2+(B_2-B_1)(16G_1^2+12G_1B_2)}{(4G_1+3B_2)[4V_2G_1(B_2-B_1)+3B_1B_2+4G_1B_1]} \tag{3.11}$$

where α, V, B, and G correspond to CTE, volume fraction, bulk modulus, and shear modulus, respectively. The subscripts c, 1, 2 refer to the composite, phase 1, and phase 2, respectively. As reported by Kurita *et al*. [13], the α, B, G of Al are 26.0 ppm/K, 72 GPa, and 26 GPa, respectively, while those of graphite are -1.0 ppm/K, 500 GPa, and 440 GPa, respectively. After substituted these parameters into Eq. (3.11), the predicted upper and lower lines were obtained in Fig. 3.14 by reversing the role of matrix and second phase in the Kerner model. In general, the experimentally measured CTE values

fall into the region between the upper and lower theoretical lines. However, the experimental CTE values of the extruded samples with Al-Si alloy were slightly higher than the upper line estimated by the Kerner model. This implies that the Al/graphite interfacial bonding in some areas is still weak, and it is possible to further decrease the CTE values of the extruded Al/graphite composites by improving the interfacial bonding between Al and graphite.

3.3.3 Compressive strength

The compressive strength of the hot-extruded Al/graphite samples along the extrusion direction is plotted in Fig. 3.15 as a function of graphite content. The compressive strength decreased with increasing the graphite content for both composites with and without Al-Si alloy. At the graphite contents of 20 % and 40 %, the extruded samples with Al-Si alloy showed compressive strength values of 114.5 MPa and 98.5 MPa, respectively, which are much higher than those without Al-Si alloy. The high strength of the extruded samples with Al-Si alloy is associated with their high density and strong Al/graphite interfacial bonding. However, the compressive strength decreased significantly at 60 % graphite and showed a relatively low value of 20.5 MPa due to severe aggregations of graphite. Moreover, in comparison with the data of conventional squeeze-cast Al/graphite composites as reported by Li *et al*. [14], the compressive strength of the extruded Al/graphite composites with Al-Si alloy exhibited higher values, especially at a graphite content of 40 %.
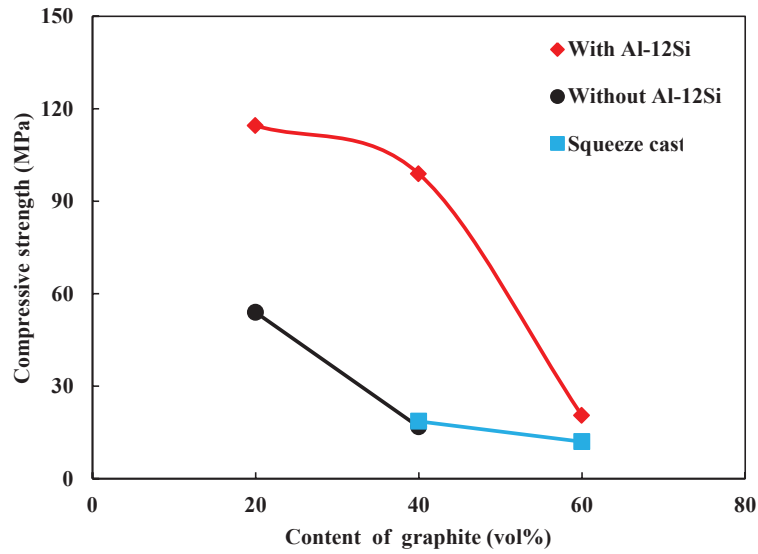
Fig. 3.15 Graphite content dependence of compressive strength of 450 ˚C-extruded Al/graphite samples with and without Al-Si alloy.

3.4 Conclusions

(1) Al/graphite composites containing small amounts of Al-12Si alloy were consolidated by SPS and hot-extrusion processes. The addition of Al-Si alloy resulted in improvements in relative density of the composites, interfacial bonding between Al and graphite, and orientation degree $f_{(00l)}$ of graphite, thus leading to enhancement of TC.

(2) As the extrusion temperature increased, the average grain size of the Al matrix increased, while the orientation degree $f_{(00l)}$ of graphite decreased. As a result, the extrusion temperature had small effect on TC of the extruded Al/graphite composites.

(3) As the graphite content increased, the TC of the hot-extruded Al/graphite composites increased. A maximum TC value of 297 W/mK was obtained at 60 vol% graphite with 9 vol% Al-Si addition.

(4) The addition of Al-Si alloy caused reduction in CTE values of the hot-extruded Al/graphite composites. A minimum CTE value of 7.95 ppm/K was obtained at 60 vol% graphite with 9 vol% Al-Si addition.

(5) The hot-extruded Al/graphite composites with Al-Si alloy showed higher compressive strength in comparison with the conventional squeeze-casted composites and hot-extruded composites without Al-Si alloy.

References

[1] F.K. Lotgering: Topotactical reactions with ferrimagnetic oxides having hexagon crystal structures—I. J. Inorg. Chem 9. 113-123 (1959).

[2] D. Kim, Y. Suhng, M. Labes: Mechanical properties of pyrolytic graphite flakes. Carbon 30. 729-737 (1992).

[3] C.W. Nan, R. Birringer, D.R. Clarke, H. Gleiter: Effective thermal conductivity of particulate composites with interfacial thermal resistance. J. Appl. Phys 81(10). 6692-6699 (1997).

[4] C.W. Nan, X.P. Li, R. Birringer: Inverse problem for composites with imperfect interface: determination of interfacial thermal resistance, thermal conductivity of constituents, and microstructural parameters. J. Am. Ceram. Soc. 83(4). 848-854 (2000).

[5] J.M. Molina, R. Prieto, J. Narciso, E. Louis: The effect of porosity on the thermal conductivity of Al-12 wt% Si/SiC composites. Scr. Mater. 60(7). 582-585 (2009).

[6] E.T. Swartz, R.O. Pohl: Thermal boundary resistance. Rev. Mod. Phys 61(3). 605-668 (1989).

[7] Z.Q. Tan, Z.Q. Li, D.B. Xiong, G.L. Fan, G. Ji, D. Zhang: A predictive model for interfacial thermal conductance in surface metallized diamond aluminum matrix

composites. Mater. Design. 55. 257-262 (2014).

[8] B. Dewar, M. Nicholas, P.M. Scott: The solid phase bonding of copper, nickel and some of their alloys to diamonds. J. Mater. Sci. 11(6). 1083-1090 (1976).

[9] A.J. Schmidt, K.C. Collins, A.J. Minnich, G. Chen: Thermal conductance and phonon transmissivity of metal-graphite interfaces. J. Appl. Phys. 107(10). 104907 (2010).

[10] G.M. Yuan, X.K. Li, Z.J. Dong, W. Aidan, Z.W. Cui, C. Ye, H.D. Du, F.Y. Kang Graphite blocks with preferred orientation and high thermal conductivity. Carbon 50(1). 175-182 (2012).

[11] M. Murakami, N. Nishiki, K. Nakamura, J. Ehara, H. Okada, T. Kouzaki, K. Watanabe, T. Hoshi, S. Yoshimura: High quality and highly oriented graphite block from polycon-densation polymer films. Carbon 30(2). 255-262 (1992).

[12] E.H. Kerner: The elastic and thermos-electric properties of composite media. Proc. Phys. Soc. 69(8). 808-813 (1956).

[13] H. Kurita, T. Miyazaki, A. Kawasaki, Y.F. Lu, J.F. Silvain: Interfacial microstructure of graphite flake reinforced aluminum matrix composites fabricated via hot pressing. Compos Part A: Appl. Sci. Manuf. 73. 125-131 (2015).

[14] W.J. Li, Y. Liu, G.H. Wu: Preparation of graphite flakes/Al with preferred orientation and high thermal conductivity by squeeze casting. Carbon 95. 545-551 (2015).

Chapter 4   Fabrication of Al/carbon fibers composites by hot-extrusion process

4.1 Introduction

In chapters 2 and 3, Al/graphite composites have been successfully fabricated by a hot-extrusion technique, indicating that hot-extrusion is an effective method to fabricate highly oriented Al-based composites. Recently, Tokunaga *et al*. [1] have reported to fabricate Al/CFs composites by a hot-extrusion technique. They found that the CFs were mainly oriented along the extrusion direction. Moreover, the addition of small amounts of Al-Si alloy led to enhancement in relative density and TC of composites. However, the effects of CFs size and extrusion temperature on microstructure and TC were investigated by few researchers. In this chapter, Al/CFs composites with different CFs size were fabricated by a hot-extrusion technique and the relationships among processing conditions, microstructure, and TC were investigated.

4.2 Experimental procedure

4.2.1 Starting materials

Pure Al powder (>99.9% purity, mean particle size of 30 μm) and CFs with different lengths and TCs, named K13D2U and K223HM [2], were used as the starting materials, as shown in Table 4.1. The appearances of the CFs were shown in Fig. 4.1, the K13D2U CFs had continuous morphology, while the K223HM CFs exhibited powder shape. In this study, the K13D2U CFs were chopped into an average length of 3 mm. For simplification, hereafter, the K13D2U and K223HM CFs were called long CFs and short CFs, respectively.

Table 4.1 Density and thermal conductivity of matrix and second phase used in this study [2].

Material		Type/length	Density (g/cm^3)	Thermal Conductivity (W/mK)
Matrix	Al		2.7	200
Second phase	Carbon fibers	K13D2U/3 mm	2.2	800/10 (//CF axis / ⊥CF axis)
		K223HM/ 200 μm	2.2	550/10 (//CF axis / ⊥CF axis)
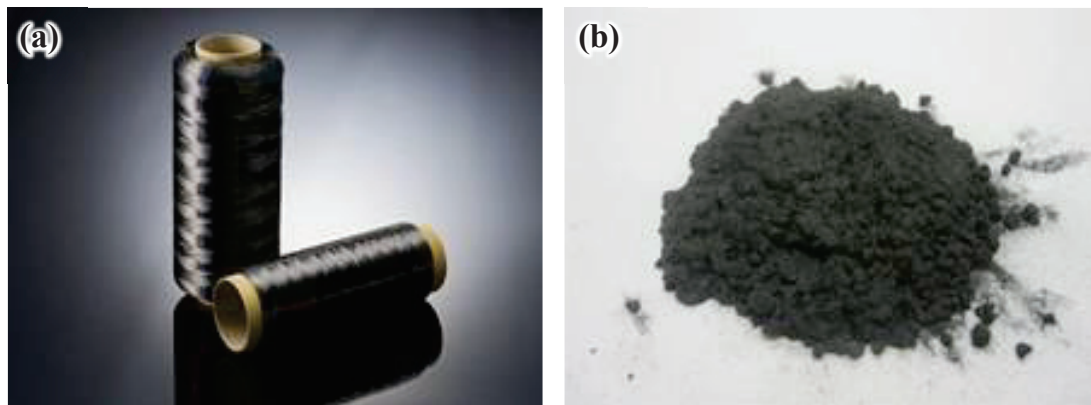
Fig. 4.1 Appearances of CFs named (a) K13D2U and (b) K223HM.

4.2.2 Consolidation method

The Al and CFs with nominal compositions of 10, 20, 30, and 40 vol% CFs were ball-milled for 8 h. The Al/CF powder mixture was sintered by spark plasma sintering (SPS) at 450 ˚C for 10 min under 40 MPa. The conditions of SPS are listed in Table 4.2. The sintered samples were rotated 90° and then vacuum-encapsulated into an Al can to obtain a billet used for hot extrusion (Fig. 4.2). The extrusion was performed in a temperature range of 400-500 ˚C with an extrusion ratio of 14:1 and a punch speed of 1 mm/min. The extrusion conditions are listed in Table 4.3.

Table 4.2 Conditions of SPS

Atmosphere	Vacuum
Heating rate	30 ˚C/min
Temperature	450 ˚C
Pressure	40 MPa
Sizes of green compact	Φ20mm×20mm

Table 4.3 Conditions of hot extrusion

Extrusion billet	SPSed compact
Atmosphere	Air
Extrusion temperature	400-500℃
Extrusion ratio	14
Extrusion speed	1mm/min

Fig. 4.2 Schematic view of 90° rotated vacuum-encapsulation.

4.2.3 Characterization

The density of the extruded samples was determined by the Archimedes method.

The density and relative density were calculated by the following equations, respectively.

$$\rho = \frac{m_a}{m_a - m_w} \times \rho_w \qquad (4.1)$$

$$\rho_R = \frac{\rho}{\rho_T} \times 100 \qquad (4.2)$$

where ρ and ρ_w are the density of the sample and water, respectively; m_a and m_w are the weight of sample in the air and water, respectively; ρ_R and ρ_T are the relative density and theoretical density of the sample, respectively.

The orientation parameter F of CFs was determined using the Herman's method by the following equations [3]:

$$F = 2 \times (cos\,\theta)^2 - 1 \qquad (4.3)$$

where θ is the angle between the extrusion direction and the axis direction of CF; $F = 1$ means the CFs are completely parallel to the extrusion direction; $F = 0$ means the CFs are Randomly oriented; $F = -1$ means the CFs are completely perpendicular to the extrusion direction.

The microstructure was observed by optical microscope (OM) and scanning electron microscope (SEM). The TC was determined by measuring thermal diffusivity and specific heat at room temperature by using a laser flash apparatus (LFA457 Micro Flash, Netzsch, Germany).

4.3 Results and discussion

4.3.1 Microstructure

Fig. 4.3 shows the appearances of the extruded Al/CFs samples with different graphite contents. The samples with graphite contents of ≤30 vol% exhibited sound appearances, and no evident cracks, voids and other defects were observed, as shown in Figs. 4.3 (a)-(c) and (e)-(g). However, many defects were clearly observed on the

64

surface of the sample with 40 vol% graphite (see Figs. 4.3 (d) and (h)). This may result from severe aggregation of CFs and thus lead to poor formability.
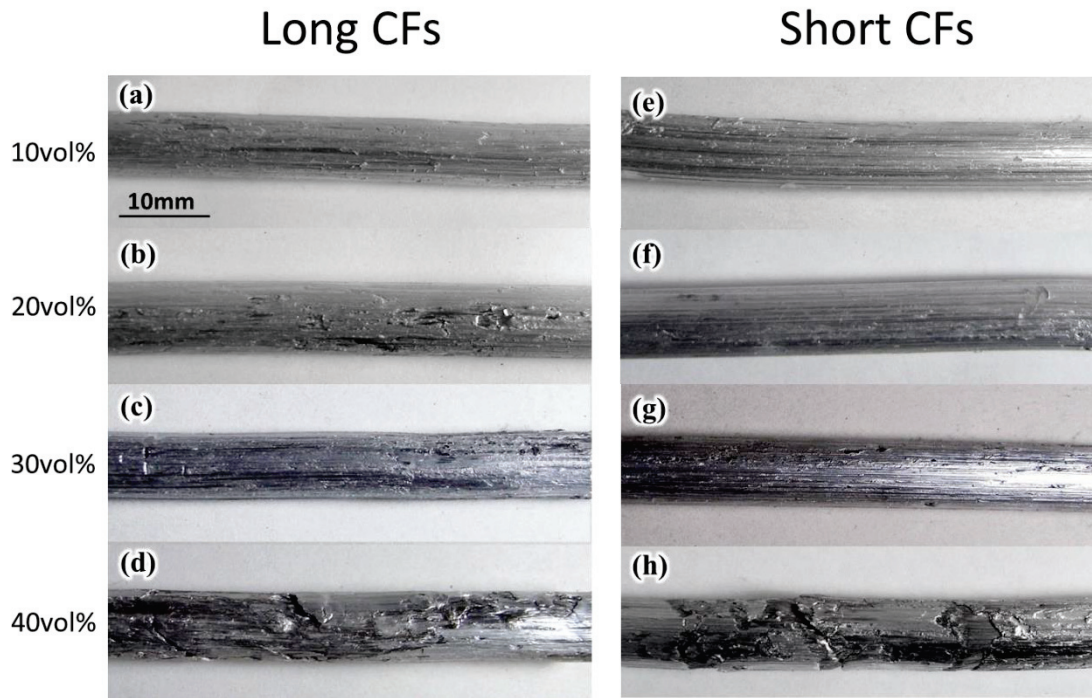

Fig. 4.3 Appearances of Al/CFs samples with (a) 10 vol%, (b) 20 vol%, (c) 30 vol%, (d) 40 vol% long CFs (3 mm) and (e) 10 vol%, (f) 20 vol%, (g) 30 vol%, (h) 40 vol% short CFs (200 μm). Extrusion temperature: 450 ˚C.

Fig. 4.4 shows the variations of relative density of the 450 ˚C-extruded Al/CFs samples with different CFs sizes and contents. The relative density of all the extruded samples decreased with increasing the CFs content. This indicates that the presence of CFs inhibits the deformation of Al matrix and densification of the composites. In addition, the relative density of the samples with short CFs was slightly higher than that with long CFs. This is assumed to be related to the more aggregation of long CFs. With regard to the samples extruded at different temperatures, the relative density showed almost the same values, indicating the extrusion temperature had small effect on porosity and Al/graphite interfacial bonding of the extruded samples.
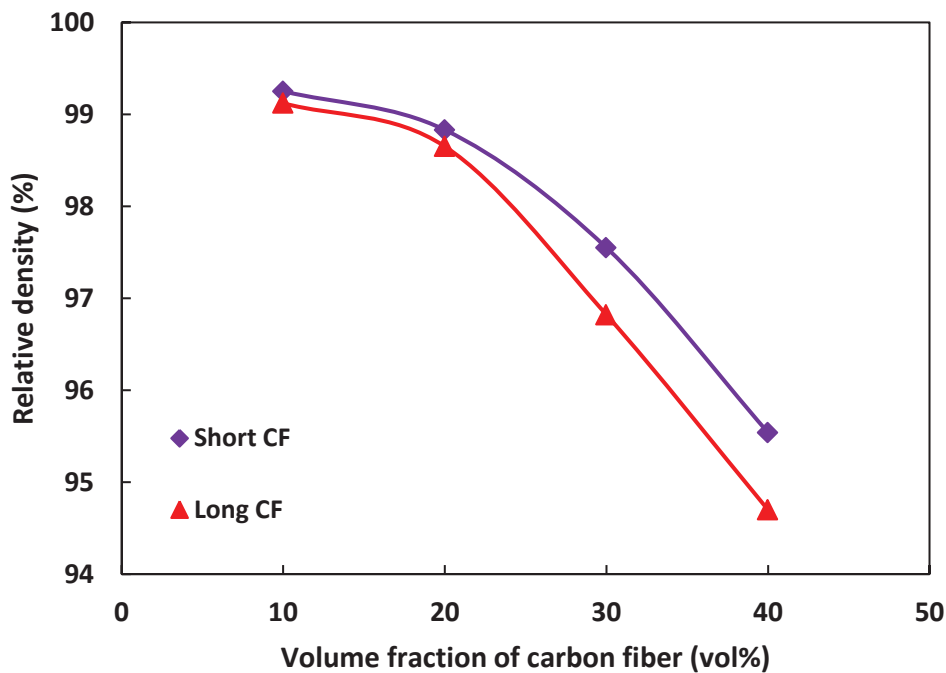
Fig. 4.4 Variations of the relative density of the hot-extruded Al/CFs samples with different CFs sizes and contents. Extrusion temperature: 450 ˚C.

Fig. 4.5 shows the SEM images (backscattered electron mode) on longitudinal sections of the 450 ˚C-extruded Al/CFs samples with different CFs sizes and contents, where the white and dark regions correspond to Al and CFs, respectively. It was clearly observed that the CFs tended to be distributed along the extrusion direction in the extruded samples. As the CFs content increased, more aggregation of CFs can be observed in the sample with long CFs. In contrast, the samples with short CFs exhibited homogeneous distribution. Furthermore, Fig. 4.6 shows the SEM images of the Al/20 vol% long CFs samples extruded at different temperatures. As the extrusion temperature varied, no evident change can be seen in the distribution of CFs.
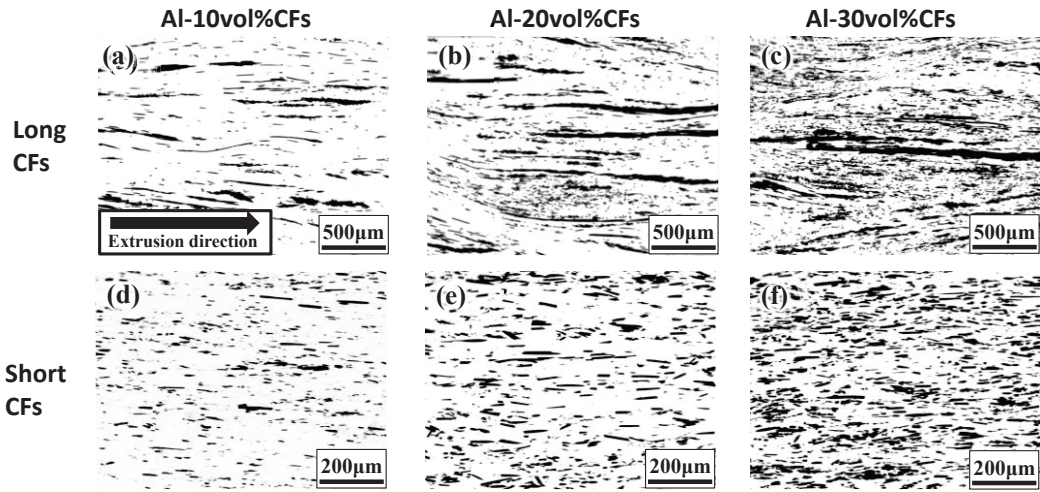
Fig. 4.5 SEM images on longitudinal sections of the hot-extruded Al/CFs samples with (a) 10 vol%, (b) 20 vol%, (c) 30 vol% long CFs (3 mm) and (d) 10 vol%, (e) 20 vol%, (f) 30 vol% short CFs (200 μm). Extrusion temperature: 450 ˚C.
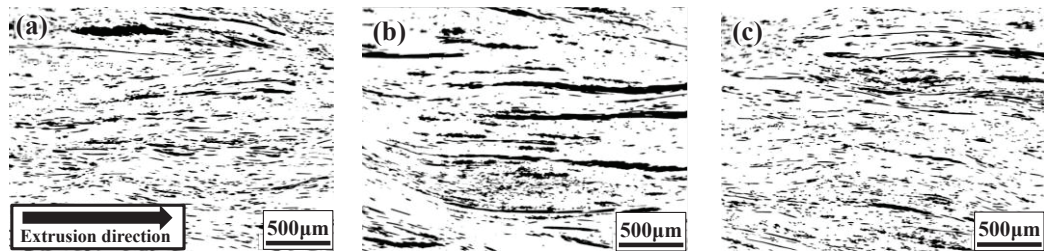
Fig. 4.6 SEM images on longitudinal sections of Al/20 vol% CFs (long CFs 3mm) samples extruded at (a) 400 ˚C, (b) 450 ˚C, (c) 500 ˚C.

In order to measure the Al grain size of the Al/20 vol% CFs samples extruded at different temperatures, the samples were etched by 7% hydrofluoric acid, and observed by OM. The etched microstructures of the samples with long CFs extruded at (a) 400 ˚C, (b) 450 ˚C, (c) 500 ˚C were shown in Fig. 4.7. The Al grains were deformed and elongated along the extrusion direction. As the extrusion temperature increased, grain growth can be observed. The average grain sizes of the Al matrix were measured as 9.23 μm, 11.56 μm, and 12.37 μm at 400 ˚C, 450 ˚C, and 500 ˚C, respectively.

Fig. 4.8 illustrates the quantitative results of the orientation parameter of CFs in

Al/CFs samples. With increasing the CFs content, the orientation parameter of long CFs at CFs contents of 20 and 30 vol% showed slightly lower value in comparison with that at CFs content of 10 vol%. This may be related to the severe aggregation of long CFs at a higher CFs content. In comparison, the orientation parameter of short CFs had small change with increasing the CFs content. Moreover, in Fig. 4.9, as the extrusion temperature increased, the orientation parameter of long CFs decreased slightly. This is attributed to the reduction in deformation resistance of Al with increasing the extrusion temperature, leading to a weaker orientation degree of CFs.
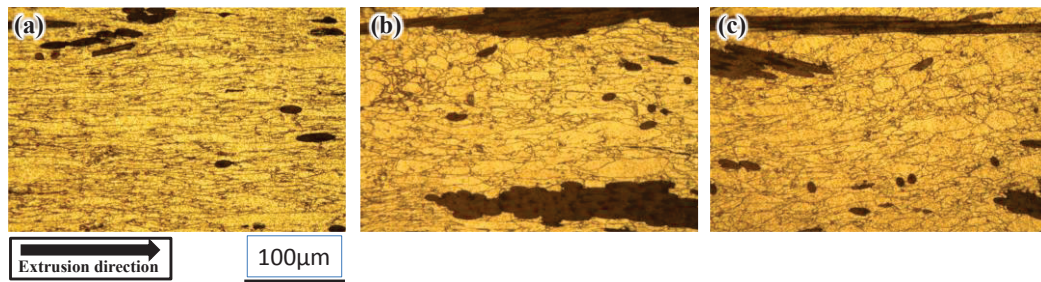
Fig. 4.7 OM images of the etched microstructures of Al/20 vol% CFs (long CFs 3mm) samples extruded at (a) 400 ˚C, (b) 450 ˚C, (c) 500 ˚C.
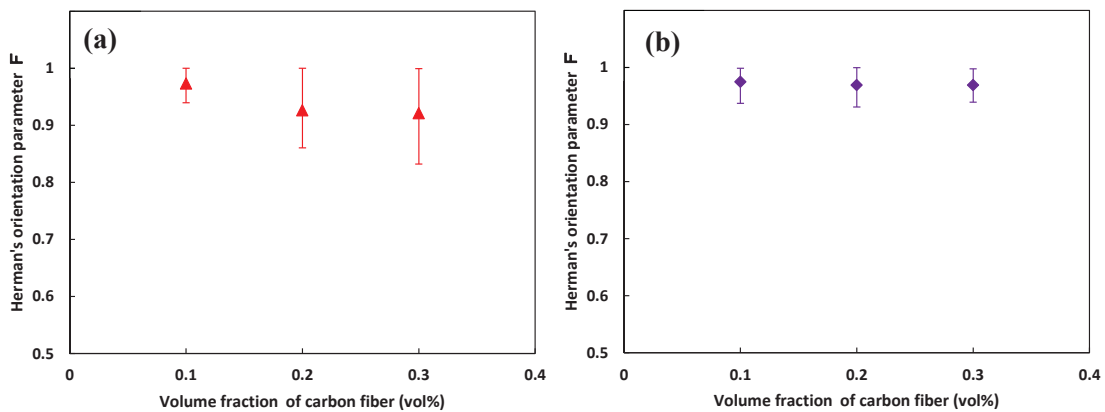
Fig. 4.8 Orientation parameter of CFs in Al/CFs samples with (a) long CFs and (b) short CFs.
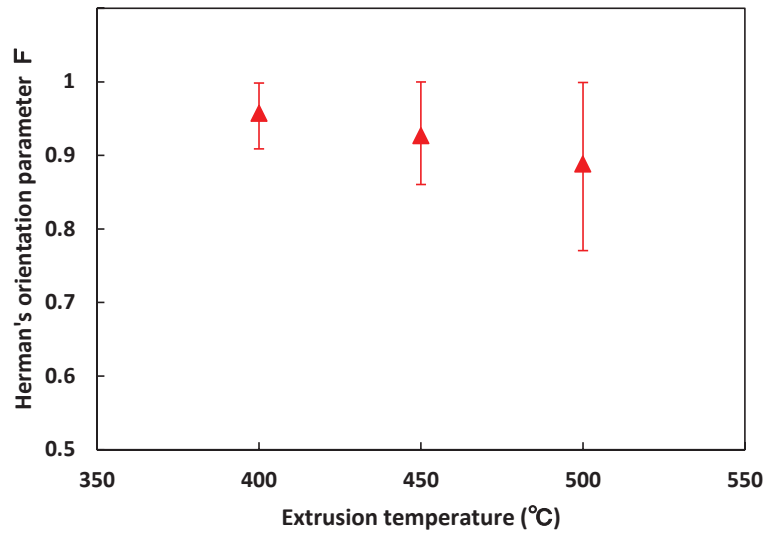
Fig. 4.9 Orientation parameter of CFs in Al/ 20 vol% long CFs samples extruded at (a) 400 ˚C, (b) 450 ˚C, and (c) 500 ˚C.

4.3.2 Thermal conductivity

Fig. 4.10 shows the CFs content dependence of TC of the Al/CFs samples extruded at 450 ˚C. For the samples with the long CFs, the measured TC along the extrusion direction exhibit larger improvement in TC in comparison with short CFs. Besides, as the CFs content increases, the TC of the samples with short CFs had small change. This is because of large interfacial thermal resistance. In contrast, with addition of long CFs, the interfacial thermal resistance decreased obviously. The TC improved significantly from 0 to 20 vol% and decreased obviously from 20 % to 30 vol%. The reduction in TC of the sample with 30vol% CFs may be related to lower relative density and more aggregation of long CFs. On the other hand, Fig. 4.11 shows the TC of Al/20 vol% long CFs extruded samples as a function of extrusion temperature. In the temperature range of 400-500 ˚C, the TC showed a peak value at 450 ˚C. The TC value increased as the extrusion temperature increased from 400 to 450 ˚C. This is mainly attributed to the grain growth (Fig. 4.7) at a higher extrusion temperature, which causes reduction in

scattering of phonons at grain boundaries. However, as the extrusion temperature further increased from 450 to 500 ˚C, the TC decreased and thus reached a peak at 450 ˚C. A lower TC value at 500 ˚C is likely to be due to a significant reduction in orientation degree of graphite as mentioned previously (Fig. 4.9). Another possible reason may be due to the formation of Al_4C_3 compound during the hot extrusion at 500 ˚C. The above results suggest that grain boundaries play a dominant role in thermal conduction in the extrusion temperature range of 400-450 ˚C, whereas the orientation degree of the graphite becomes dominant at 450-500 ˚C.
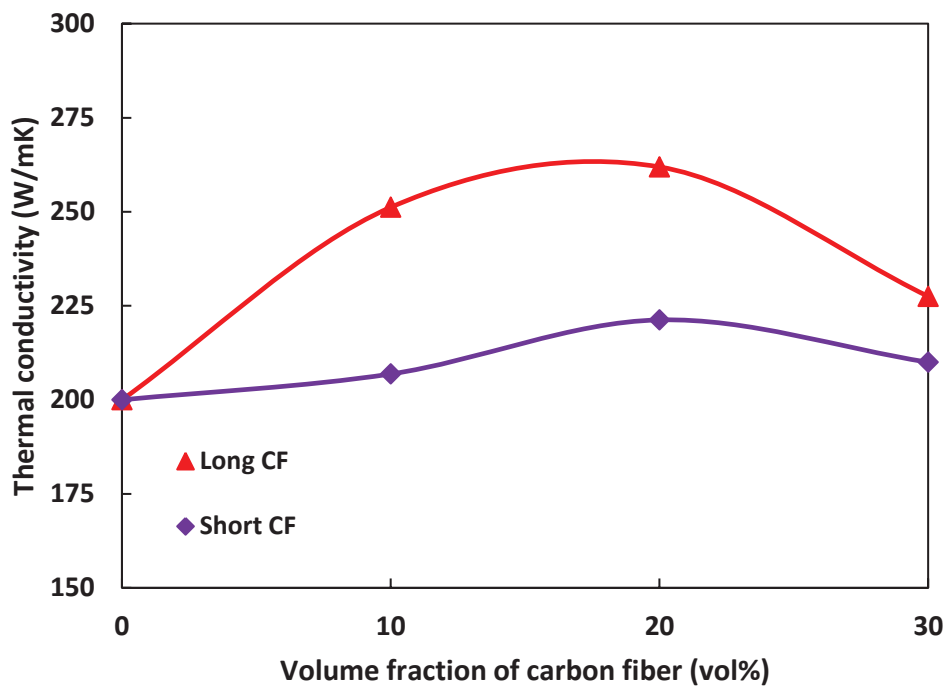
Fig. 4.10 TC of the 450 ˚C-Al/CFs extruded samples with different CFs sizes and contents.
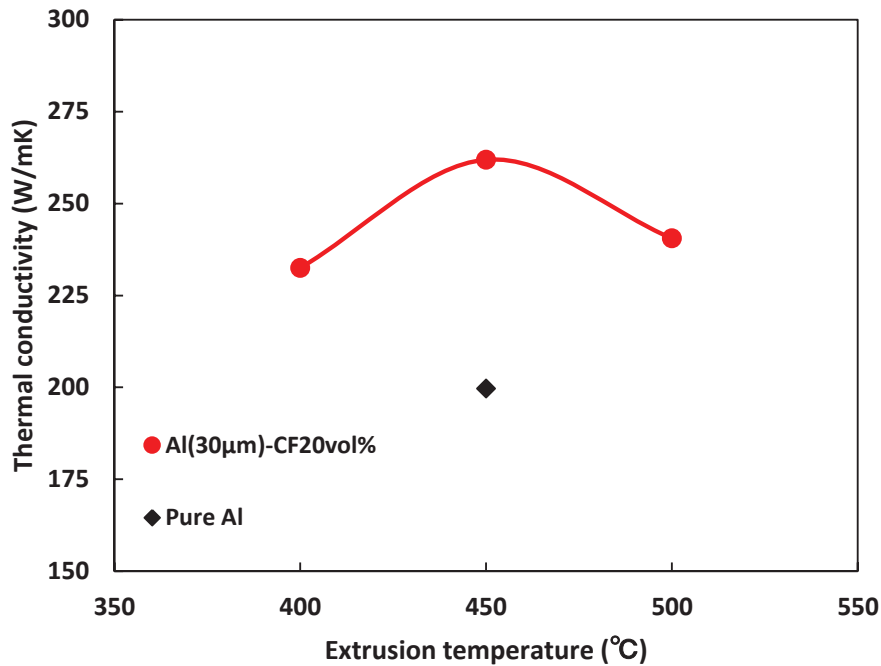
Fig. 4.11 TC of Al/20 vol% long CFs (3 mm) samples as a function of extrusion temperature.

4.4 Conclusions

(1) Al-CFs composites have been successfully fabricated by a hot-extrusion method.

(2) The microstructure of extruded composites showed that the CFs were mainly distributed along the extrusion direction.

(3) The orientation degree of CFs depended on the extrusion temperature. With the increase in extrusion temperature, the orientation degree of CFs became smaller.

(4) The incorporation of long CFs exhibited larger improvement in TC in comparison with short CFs.

(5) The TC of the extruded samples depended on the extrusion temperature, and the samples extruded at 450 ˚C exhibited high TC.

References

[1] T. Tokunaga, K. Takahashi, M. Ohno, K. Sasaki, T. Imanshi, K. Matsuura: Fabrication of carbon fiber oriented Al-based composites by hot extrusion and evaluation of their thermal conductivity. Mater. Trans. 58. 938-944 (2017).

[2]https://www.m-chemical.co.jp/products/departments/mcc/cfcm/product/1200539_73 04.html　2018/10/1.

[3] Alexander, L. E. X-ray diffraction in polymer science. Wiley. New York. 9 (8). 635-636 (1971).

Chapter 5 Microstructure and thermal/mechanical properties of Ni-coated carbon fibers/Al composites prepared by spark plasma sintering

5.1 Introduction

Since Al/CFs composites can be successfully fabricated by hot-extrusion process, it is important to further improve their thermal/mechanical properties by surface modification of CFs. As reported by Qu *et al*. [1], surface coating for CFs is an effective method to enhance the interfacial bonding and thus improving the thermal/mechanical properties. In recent years, Ni-coating as an effective and potential surface modification method for Al/CFs composites has attracted much attention. For example, Tan *et al*. [2] have calculated that Ni layer with the thickness less than 1.0 μm can improve the interfacial thermal conductance and TC of the Al/C composites, while some metal layers with high TC, such as Cu and Ag cannot. In addition, Hou *et al*. [3] have examined the effect Ni-coating on TC and mechanical properties of Magnesium/CFs composites fabricated by powder metallurgy process. Further, Chen *et al*. [4] have investigated the effect Ni-coating on microstructure, CTE, and mechanical properties of copper/graphite composites fabricated by SPS. The above reports indicate that Ni-coating can effectively enhance the interfacial bonding, TC, and mechanical properties, as well as reduce the CTE of composites. However, Chen *et al*. did not deeply investigate the effect of Ni-coating on TC. In addition, the addition of CFs in the study of Hou *et al*. [3] was only 0.8-1.5 vol%, which leads to slightly enhancement in thermal/mechanical properties. Consequently, in this chapter, large amount of Ni-coated CFs were incorporated into Al matrix, and Al/Ni-coated CFs composites were fabricated by SPS process. The purpose is to investigate the effect of Ni-coating on microstructure

and thermal/mechanical properties and find optimal Ni-coating and SPS process conditions.
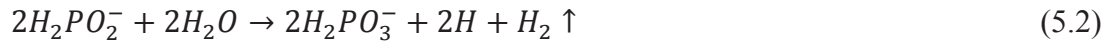
5.2 Experimental procedure

5.2.1 Preparation of Ni-coated CFs

Milled mesophase pitch-based CFs (XN-100 type, supplied by Nippon Graphite Fiber Corp., Japan) with an average length of 250 μm, diameter of 10 μm, TC in axial of 900 W/mK, and density of 2.2 g/cm^3 were used in the experiment. Ni-coated CFs were obtained by electroless deposition technique which involved the following steps (see Fig. 5.1): (1) Defatting treatment: to remove the photoresist on the surface of CFs, the raw CFs were immersed in acetone with mechanical stirring for 10 min, and rinsed by distilled water. (2) Etching treatment: to make the surface of CFs rougher and facilitate the subsequent Ni coating, the CFs were immersed in 10 mass% HNO$_3$ with mechanical stirring for 10 min. (3) Sensitizing and activating treatments: to deposit Pd catalyst on the surface of CFs, the CFs were immersed in tin(II) chloride (SnCl$_2$) solution (100 mL, 20 g/L SnCl$_2$, 40 mL/L HCl) with mechanical stirring for 5 min, and then immersed in palladium(II) chloride (PdCl$_2$) solution (100 mL, 0.2 g/L SnCl$_2$, 50 mL/L HCl) with mechanical stirring for 5 min after carefully washing and filtration. The chemical reaction is shown by the following equation:

$$Pd^{+2} + Sn^{+2} \rightarrow Sn^{+4} + Pd \tag{5.1}$$

(4) Ni electroless coating: same quantity of activated CFs (3.5g) were dropped into coating solutions (100mL, 20 mL/L LPH-S provided by Okuno Chemical Industries Co., Ltd., coating temperature of 75 ˚C, and pH of 6.5) with different coating times (1, 1.5, 2, 3, 5 min) so as to control the thickness of coating layer, with the following reations:

$$2H_2PO_2^- + 2H_2O \rightarrow 2H_2PO_3^- + 2H + H_2 \uparrow \tag{5.2}$$

$$Ni^{2-} + 2H \rightarrow Ni + 2H^+ \tag{5.3}$$

$$H_2PO_2^- + H \rightarrow P + OH^- + H_2O \tag{5.4}$$

(5) Washing and drying: the Ni-coated CFs were washed by methanol to reduce the aggregation, and followed by drying in a vacuum desiccator at room temperature.
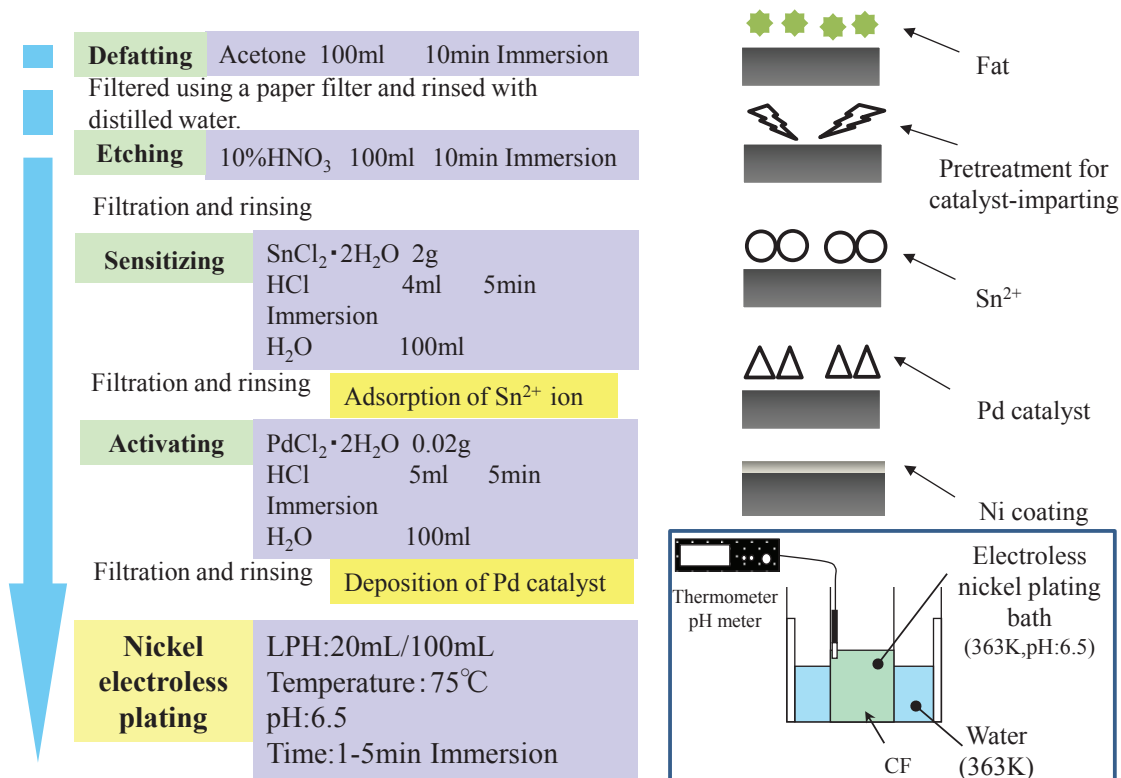

Fig. 5.1 Schematic diagram of Ni coating.

5.2.2 Consolidation method

The samples were fabricated by spark plasma sintering (SPS). Firstly, the raw CFs or Ni-coated CFs and pure Al powders (99.99%, 30 μm) were used as the starting materials. The powders with nominal compositions of 40 vol% CFs were mixed under 50 rpm for 8 h. Subsequently, the mixed powders were consolidated by SPS under a pressure range of 40-100 MPa and a temperature range of 400-500 °C for 0-10 min. The

planes in the composites perpendicular and parallel to the SPS loading direction were named as X-Y plane and Z plane, respectively (see Fig. 5-2).

Pressing direction

X-Y Plane   Z Plane
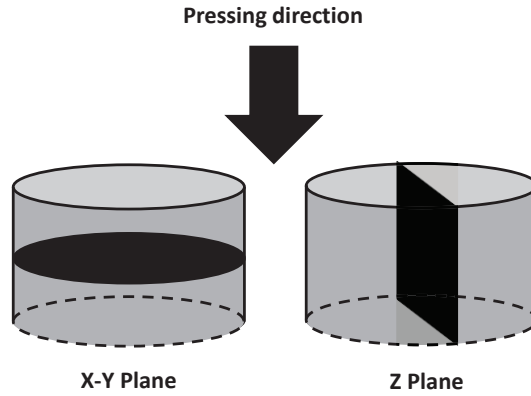
Fig. 5.2 Schematic views of X-Y and Z planes of SPSed composite

5.2.3 Characterization

The density of the extruded samples was determined by the Archimedes method, which was illustrated by the following equations:

$$\rho = \frac{m_a}{m_a - m_w} \times \rho_w \tag{5.5}$$

$$V_{Ni} = \frac{m_{Ni}}{\rho_{Ni}} \times \frac{x}{5} \tag{5.6}$$

$$\rho_T = \frac{V_{Al} \times \rho_{Al} + V_{CF} \times \rho_{CF} + V_{Ni} \times \rho_{Ni}}{V_{Al} + V_{CF} + V_{Ni}} \tag{5.7}$$

$$\rho_R = \frac{\rho}{\rho_T} \times 100 \tag{5.8}$$

where ρ, ρ_w, ρ_{Al}, ρ_{CF}, ρ_{Ni} are the density of the sample, water, Al, CF, and Ni, respectively; m_a and m_w are the weight of sample in the air and water, respectively; V_{Al}, V_{CF}, and V_{Ni} are the volume of Al, CF, and Ni, respectively; x is the Ni coating time; ρ_R and ρ_T are the relative density and theoretical density of the sample, respectively. Since the concentration of coating solution is 5.5 g/L Ni, there is 0.11 g Ni in 20 mL coating solution by calculation. In addition, when coating time was 5 min, the color of coating

solution varied from blue to colorless, indicating the Ni ions in the solution were completely reduced. Therefore, in this study, we assumed that the weight of the reduced Ni was in proportion to the coating time.

The surface morphology of the starting materials and the microstructures of the composites were observed by scanning electron microscopy (SEM). The element distribution was characterized by energy dispersive X-ray spectroscopy (EDS) and electron probe micro-analyzer (EPMA). The phase composition was analyzed by X-Ray Diffraction (XRD). The TC was determined by measuring thermal diffusivity and specific heat at room temperature by using a laser flash apparatus (NETZSCH LFA457, Germany). The specimens for TC measurements were in the form of discs with a diameter of 6 mm and a thickness of 2 mm. The CTE was determined using a horizontal dilatometer (SEIKO TMA/SS6000, Japan) in temperature range of 20-150 ℃ at a heating rate of 2 ℃/min. The CTE was measured on cuboid samples with dimension of 20 mm×5 mm×5 mm. The compression test was carried out by electronic universal testing machine (SHIMADZU SFL-50kNAG, Japan) with a compression rate of 1 mm/min. The compression specimens were cylinders with dimensions of Φ6 mm×8 mm.

5.3 Results and discussion

5.3.1 Microstructure and Thermal conductivity

5.3.1.1 Effect of Ni thickness

Fig. 5.3 (a) shows the surface morphologies of coated CF with coating time of 1.5 min (hereafter 1.5 min Ni-coated CF), the bright and dark regions are likely to be correspond to Ni and CF, respectively. In order to confirm their element compositions,

EDS analysis were carried out in regions 1 and 2, with spectra shown in Figs. 5.3 (b) and (c), respectively. In Fig. 5.3 (b), not only peaks of Ni but also peak of P were detected, indicating the formation of Ni-P alloy layer on the surface of CF by co-deposition of Ni and P atoms as mentioned in equations (5.3) and (5.4). In Fig. 5.3 (c), only a sharp peak of C was detected, which corresponds to the CF.
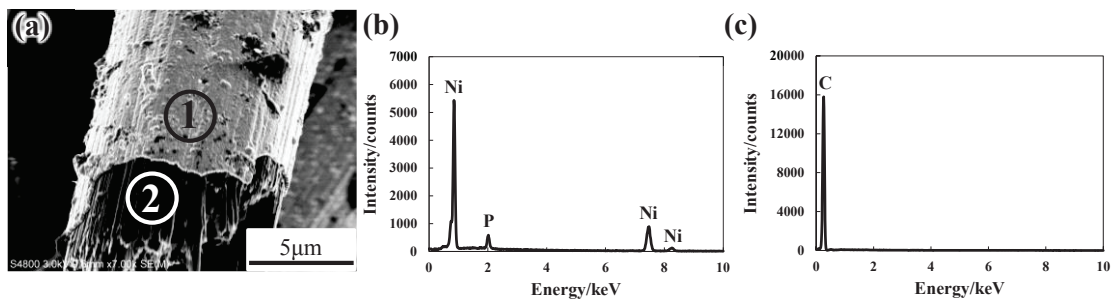

Fig. 5.3 FE-SEM morphologies of (a) 1.5 min Ni-coated CF. (b) EDS spectra corresponding to region 1. (c) EDS spectrum corresponding to region 2.

In order to measure the thickness of Ni layer, the cross sections of CFs were observed by FE-SEM. Fig. 5.4 (a) shows the cross section of 1.5 min Ni-coated CF, it can be observed that the thickness of Ni layer around the CF were uniform. Fig. 5.4 (b) exhibits the cross section of the 1.5 min Ni-coated CF at a higher magnification. The thickness was measured about 200 nm for coating time of 1.5 min. Since the thickness of Ni layer is smaller than 1 μm, it is believed that the Ni layer is beneficial to improve the interfacial thermal conduction.
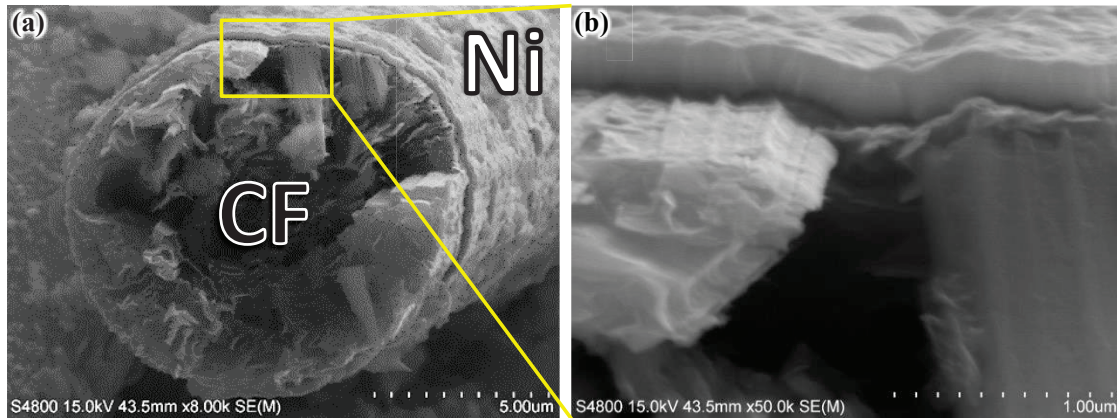
Fig. 5.4 The cross sections of the 1.5 min Ni-coated CF at different magnifications.
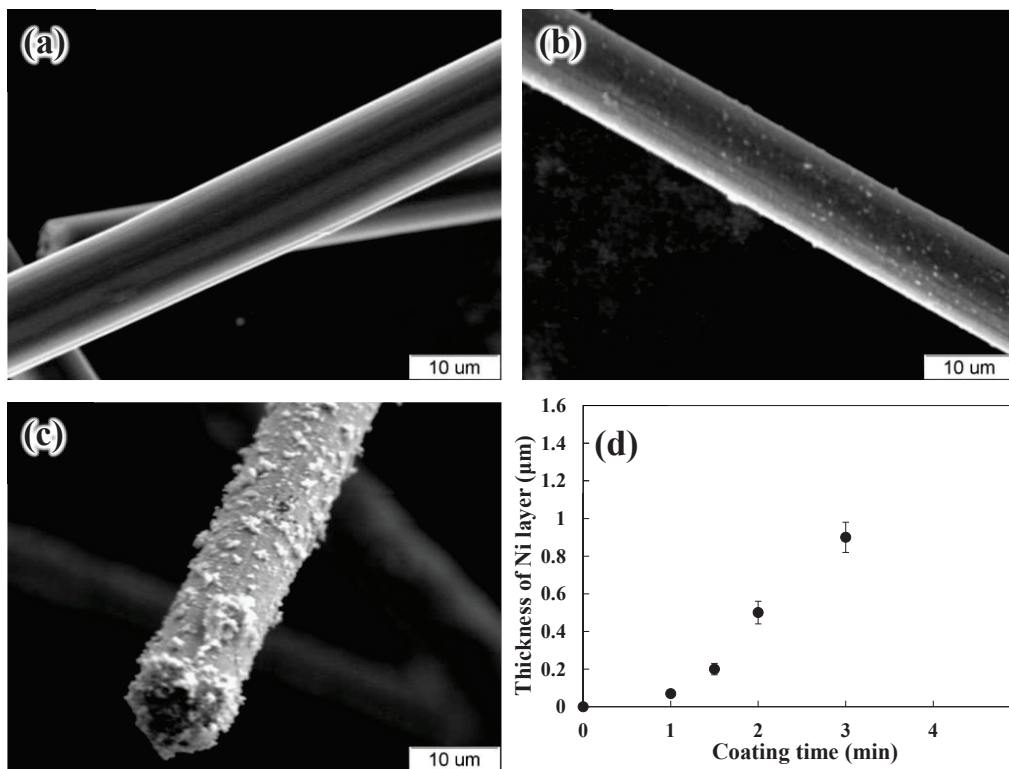

Fig. 5.5 SEM macro morphologies of the (a) raw CF and the CFs with coating times of (b) 1.5 and (c) 5 min. (d) The measured thickness of Ni layer at various coating times.

Figs. 5.5 (a)-(c) shows the SEM macro morphologies of the raw CF and the CFs with coating times of 1.5 and 5 min. It seems that the thickness of Ni layer increased

with increasing the coating time. In addition, the Ni layer at coating time of 5 min became rougher, indicating an uneven deposition effect at relatively longer coating time. Through the measurement method shown in Fig. 5.4, the thicknesses of Ni layer at various coating times were measured and exhibited in Fig. 5.5 (d). It is clear that the thickness of Ni layer increased with increasing the coating time.
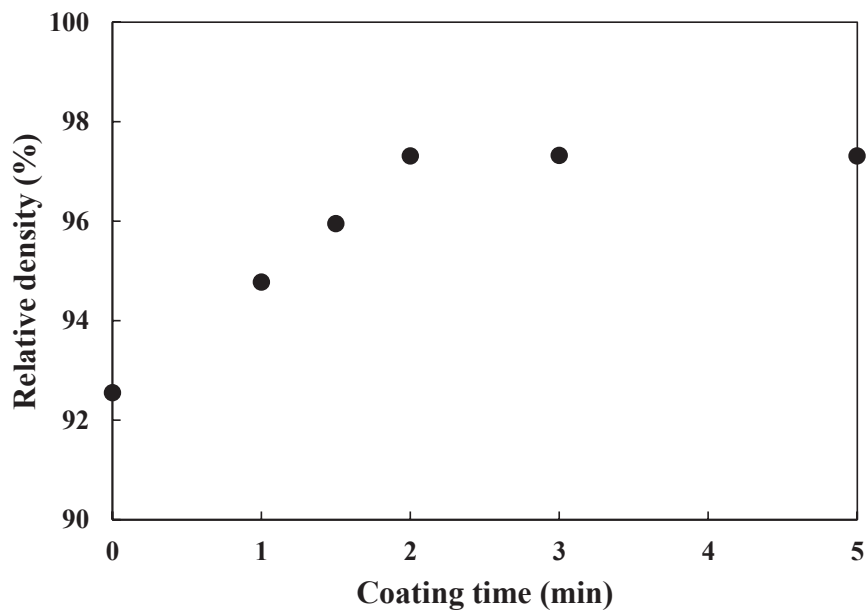
Fig. 5.6 Relative density of the Al/uncoated CF sample and Al/Ni-coated CF samples with various coating times.

Fig. 5.6 shows the relative density of the Al/uncoated CF sample and Al/Ni-coated CF samples with various coating times. The relative density values of the Al/Ni-coated CF samples were higher than that of the Al/uncoated CF sample. This indicates the enhanced Al/CF interfacial bonding with Ni-coating on the surface of CFs. In addition, the relative density values of the Al/Ni-coated CF samples increased gradually from 1 min to 2 min, which is attributed to more integrate Ni coating layer. With further increasing the coating time, the relative density remained almost unchanged. This

implies that when the Ni coating layer on the surface of CFs was integrate enough, further enhancement in thickness of Ni coating layer had small effect on density of the composites.

Fig. 5.7 shows the SEM images (backscattered electron mode) on X-Y plane of the Al/uncoated CF sample and Al/Ni-coated CF samples with various coating times. It is clear that CFs were randomly oriented in plane perpendicular to the SPS loading direction. For the Al/uncoated CF samples, severe aggregation of CFs can be observed. When the coating time increased to 1.5 min, it is obvious that the aggregation of CFs disappeared gradually and the distribution of CFs became homogenous. With further increasing the coating time, the distribution of CFs had small change and remained homogenous, which indicates that the thickness of coating layer had almost no effect on distribution of CFs in Al matrix.
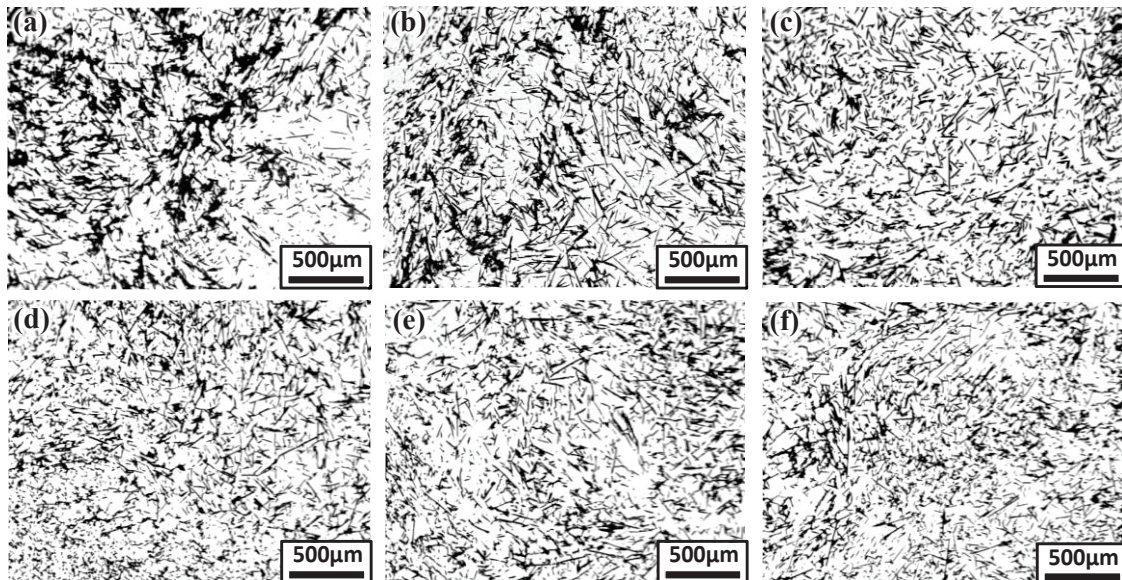
Fig. 5.7 SEM images on X-Y plane of (a) the Al/uncoated CF sample, and Al/Ni-coated CF samples with coating times of (b) 1 min, (c) 1.5 min, (d) 2 min, (e) 3 min, (f) 5 min.

Fig. 5.8 shows the SEM images (backscattered electron mode) on Z plane of the

Al/uncoated CF sample and Al/Ni-coated CF samples with coating times of 1 and 1.5 min. The CFs were mainly shown as dark points, which is in consistent with the orientation of CFs in Fig. 5.7. This indicates that the Al/CF composites may exhibit an anisotropy of thermal properties. In addition, the distribution of CFs also tended to be homogenous with increasing the coating time.
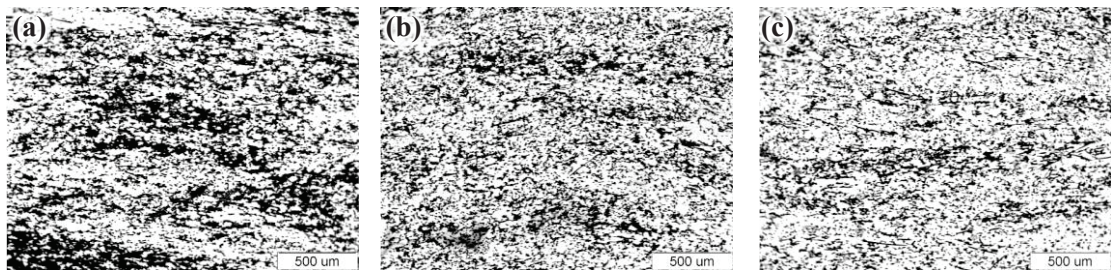

Fig. 5.8 SEM images on Z plane of (a) Al/uncoated CF sample, and Al/Ni-coated CF samples with coating times of (b) 1 min, (c) 1.5 min.

Since the distribution of CFs in Al matrix has been clarified, the interfacial structures of obtained composites were further observed by FE-SEM. Fig. 5.9 shows the FE-SEM images (secondary electron mode) on X-Y plane of the Al/uncoated CF sample and Al/1.5 min Ni-coated CF sample. In Fig. 5.9 (a), the uncoated CFs with almost no adhesion with Al, and large amount of voids can be observed, which indicates the extremely weak interfacial bonding and low density of the Al/uncoated CF sample. In contract, the Al/1.5min Ni-coated CF sample in Fig. 5.9 (b) exhibited good interfacial bonding and homogeneous distribution.
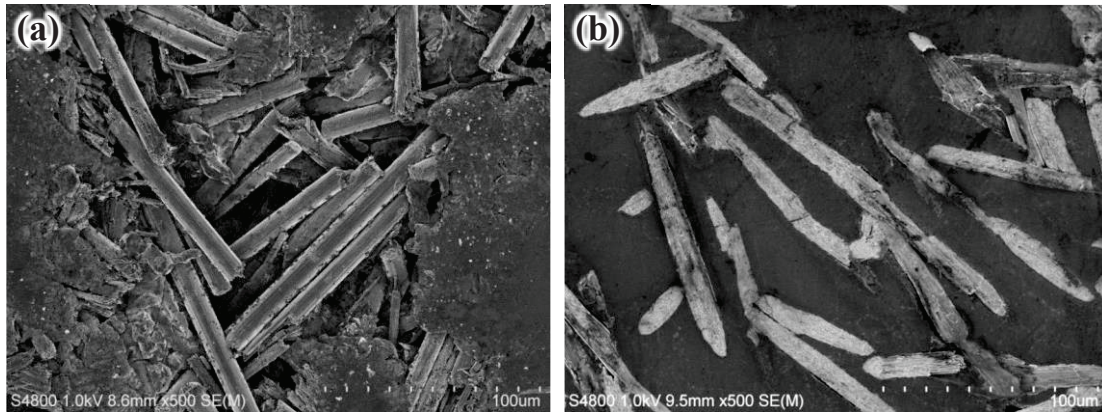
Fig. 5.9 FE-SEM images on X-Y plane of (a) Al/uncoated CF sample and (b) Al/1.5min Ni-coated CF sample.

In order to further clarify the distribution of Ni in composites, EPMA was performed for the 1.5 min Al/Ni-coated CF sample with coating time of 1.5 min. Fig. 5.10 shows the elemental distributions around the interface region. For the microstructure shown in Fig. 5.10 (d), the corresponding elemental distribution maps of Al, C, and Ni are shown in Figd. 5.10 (a)-(c), respectively. A comparison of the microstructure and Ni distribution map shows that Ni was mainly present at the interface between Al and C (*i.e.*, distributed in the initial coating layers). This confirms that the Ni layer on the surface of CFs remained integrate after powder mixing and following SPS process. However, small amounts of Ni can also be observed in Al matrix, which may degrade the TC of Al matrix. This may be attributed to the desquamation of Ni coating layer during powder mixing process. Moreover, it should be noticed that due to the error of EPMA equipment, the thickness of Ni coating layer measured from the EPMA map is slightly larger than that measured in Fig. 5.4, indicating the diffusion of Ni into Al matrix during sintering.
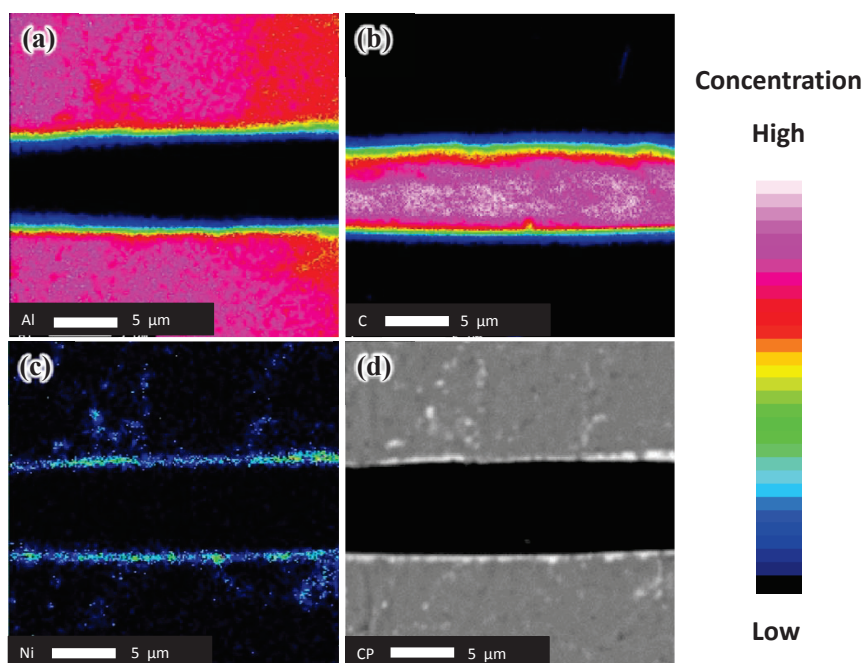
Fig. 5.10 Elemental distribution maps (a) Al, (b) C, (c) Ni and (d) corresponding backscattered electron image for the Al/1.5 min Ni-coated CF composite, analyzed by EPMA.

To confirm the formation of the reaction product, the composites were further examined by XRD in the range of $2\theta = 41\text{-}50°$, in which the characteristic peaks of Al_3Ni are included. Fig. 5.11 shows the XRD patterns on X-Y plane of the Al/uncoated CF sample and Al/Ni-coated CF samples with coating times of 1.5, 3, and 5 min. It should be noted that the extremely strong diffraction peak at $2\theta = 44.7°$ corresponding to the (200) crystal plane of Al. In addition, eight relatively weak diffraction peaks at about $2\theta = 41.2°, 41.8°, 43.7°, 45.3°, 46.0°, 47.0°, 48.4°,$ and $49.3°$ were found corresponding to (031), (112), (131), (301), (230), (311), (212), and (040) crystal planes of Al_3Ni, respectively, indicating a chemical interfacial bonding. Furthermore, it is clear that the intensities of Al_3Ni became stronger with increasing the coating time. This might be due to the rougher Ni layer on the surface of CFs with longer coating time, because rough Ni layer is easier to react with Al matrix.
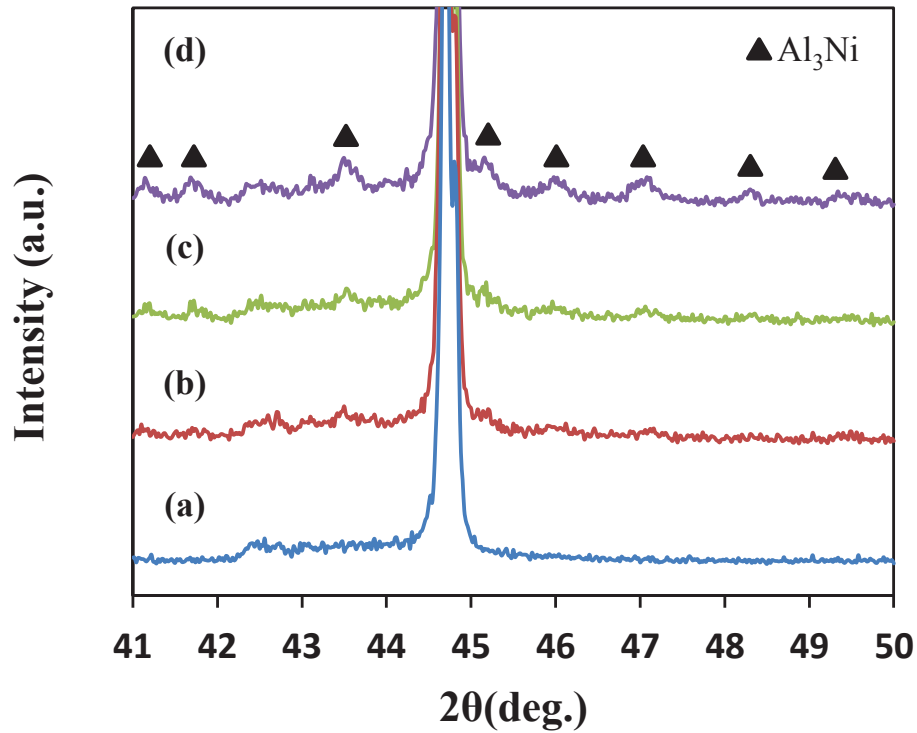
84

Fig. 5.11 XRD patterns of (a) the Al/uncoated CFs sample, and Al/Ni-coated CFs samples with coating times of (b) 1.5 min, (c) 3 min, and (d) 5 min.

Fig. 5.12 shows the TCs in X-Y plane direction and Z plane direction of the Al/uncoated CFs sample and Al/Ni-coated CFs samples with various coating times. The TC in X-Y plane direction was much higher than that in Z plane direction. This anisotropic behavior in TC is in good consistent with the alignments of CFs in Al matrix. In addition, the TC of the Al/Ni-coated CFs samples showed higher values than that of the Al/uncoated CFs sample. This is attributed to the improvements in density and Al/CFs interfacial bonding, as well as the reduction of CFs aggregation. As the coating time increased, the TC in X-Y plane direction improved obviously and reached a peak at coating time of 1.5 min, followed by a gradually reduction. The remarkable enhancement from 1 min to 1.5 min is due to the more integrate and thin enough Ni coating layer, as well as the improved density, Al/CFs interfacial bonding, and

dispersion of CFs. The decrease in TC with further increasing the coating time is considered to be due to the increased thickness of Ni coating layer and the generation of more Al_3Ni compound at the interface. On the other hand, the TC in Z plane direction had small change with increasing the coating time. This result is considered to be related to the domination effect of the extremely low TC (10 W/mK) in transverse direction of CFs. When heat transmits along the Z plane direction, the transverse section of CFs will act as heat blockers in Al matrix. Thus in Z plane direction, the low TC in transverse direction of CFs plays a dominant role in thermal conduction in comparison with the other factors. Furthermore, it should be noted that the highest TC obtained in this study is still lower than that of pure Al (~200 W/mK). This is mainly due to the randomly orientation of CFs in X-Y plane. Thus, in order to align the CFs in one direction and further improve the TC, Al/Ni-coated CF composites were fabricated by hot-extrusion process, and the results are shown in the next chapter.
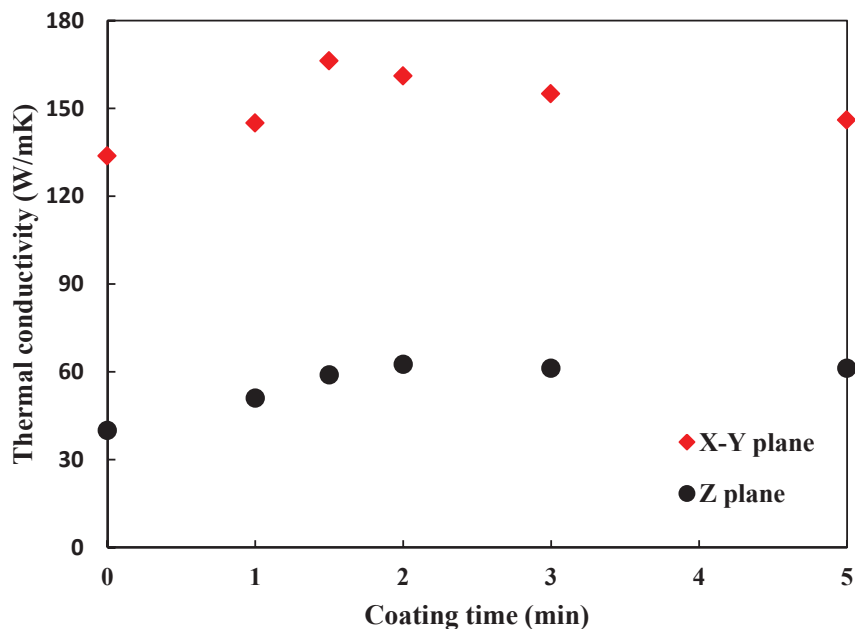

Fig. 5.12 Thermal conductivity of the Al/uncoated CFs sample and Al/Ni-coated CFs samples with various coating times.

5.3.1.2 Effect of sintering pressure

Fig. 5.13 shows the relative density of Al/1.5min Ni-coated CFs samples (sintered at 500 ˚C for 10 min) as a function of sintering pressure. As the sintering pressure increased from 40 MPa to 70 MPa, the relative density improved obviously. With increasing the sintering pressure, the contact area between the Al particles increased, thus neck formation and growth started from larger number of sites, leading to a faster densification and a larger reduction in the porosity [5]. However, as the sintering pressure further increased from 70 MPa to 100 MPa, the relative density had small change. This can be attributed to two reasons. (i) The number of sites reached saturation. (ii) Higher pressure may lead to more damages in CFs, which inhibited further densification.
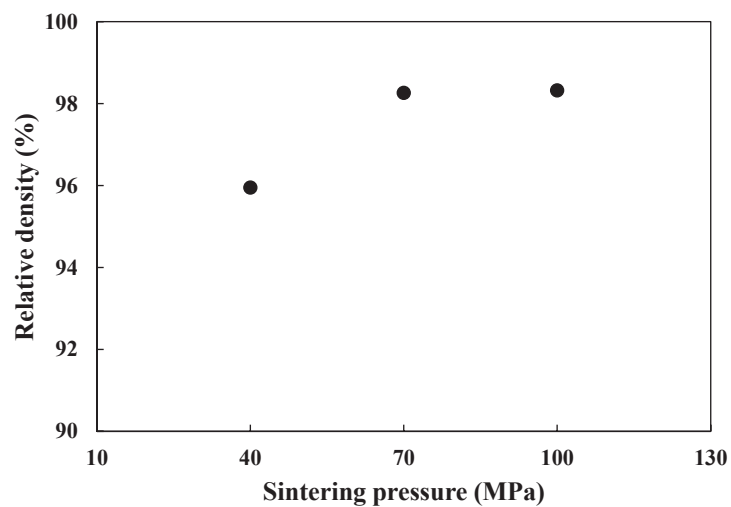
Fig. 5.13 Relative density of Al/1.5min Ni-coated CFs samples as a function of sintering pressure.

Fig. 5.14 shows the TCs in X-Y plane direction of the Al/1.5 min Ni-coated CFs samples as a function of sintering pressure. The TC value increased as the sintering pressure increased from 40 MPa to 70 MPa. This is mainly attributed to the improved density (Fig. 5.13). However, as the sintering pressure further increased, the TC

decreased and thus reached a peak at 70 MPa. A lower TC value at 100 MPa is likely to be due to more breakage of CFs and more exfoliation of Ni layers.
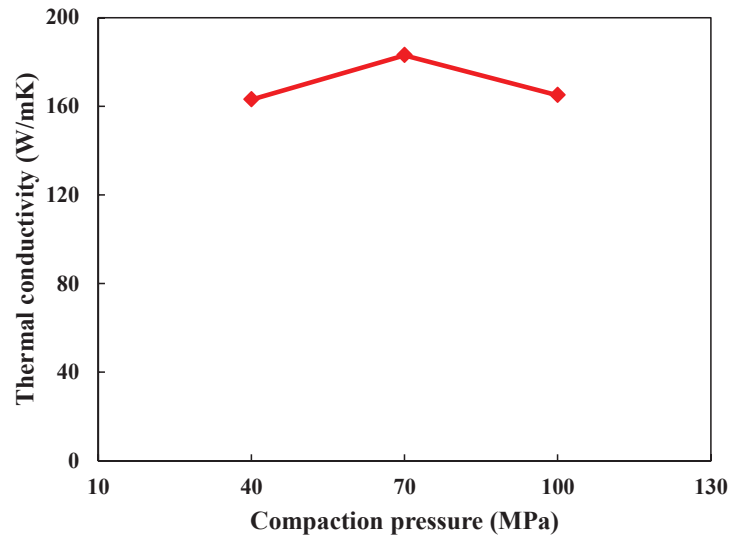

Fig. 5.14 Thermal conductivity of Al/1.5min Ni-coated CFs samples as a function of sintering pressure.

5.3.1.3 Effect of sintering temperature

Fig. 5.15 shows the relative density of Al/1.5min Ni-coated CFs samples (compacted at 70 MPa and sintered for 10 min) as a function of sintering temperature. Obviously, the relative density increased with increasing the sintering temperature. At a higher sintering temperature, particles of Al matrix diffused into each other at a faster rate, thus leading to better densification. In addition, at a higher sintering temperature, Al and Ni were easier to react and form a strong reaction bonding.
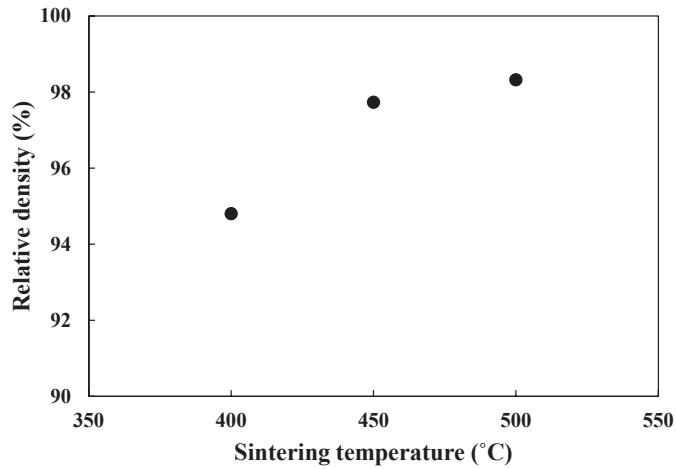
Fig. 5.15 Relative density of Al/1.5min Ni-coated CFs samples as a function of sintering temperature.

Fig. 5.16 shows the interfacial microstructures of Al/1.5 min Ni-coated CFs samples sintered at different sintering temperatures. For composite sintered at 400 ˚C (Fig. 5.16 (a)), as the arrows point, some pores existed in Al matrix near CF, which indicates poor interfacial bonding between Al and CF. When sintering temperature increased from 400 ˚C to 450 ˚C (Fig. 5.16 (b)), pores in Al matrix disappeared and the interfacial bonding between Al and CF seemed to be stronger. However, crack still can be observed at the interface. In Fig. 5.16 (c), the composite exhibited good interfacial bonding without any cracks. To further study the interfacial structure, the sample sintered at 500 ˚C was also characterized by EDS.
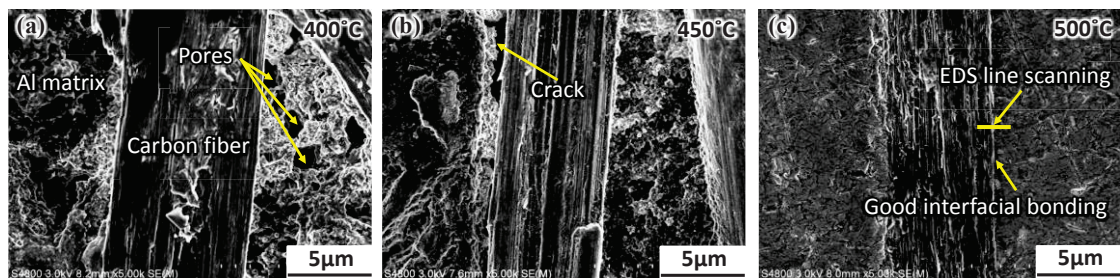

Fig. 5.16 Interfacial microstructures of Al/1.5min Ni-coated CFs samples sintered at (a) 400 ˚C, (b) 450 ˚C and (c) 500 ˚C.

Fig. 5.17 shows the element distribution of line scanned on Al/CF interface. The length of the scanning line is about 1.8 μm (Fig. 5.16 (c)). It can be seen from Fig. 5.17 that the C, Al, and Ni elements were all detected along the line perpendicular to the Al/CF interface. It can be seen that the Ni enrichment near the interface is about 0.8 μm, which is larger than the thickness of Ni layer (~ 0.2 μm, see Fig 5.4 (b)). This indicates the interfacial inter-diffusion of Al-Ni and thus leading to a strong Al-Ni reaction bonding.
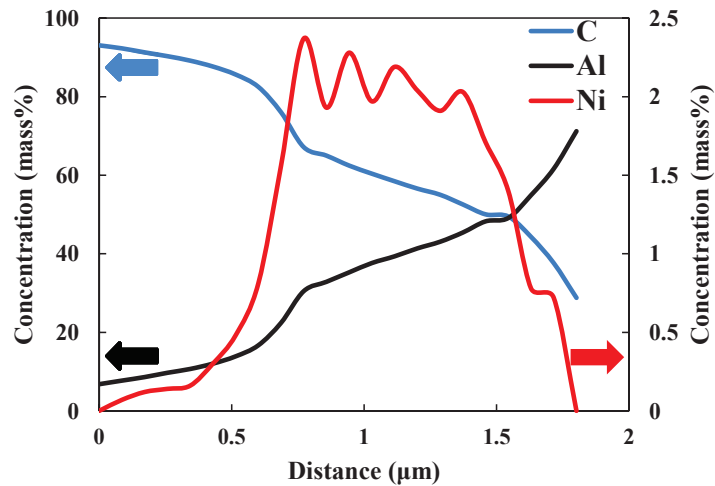

Fig. 5.17 Element distribution of line scanned on Al/CF interface.

Fig. 5.18 shows the TC in X-Y plane direction of the Al/1.5 min Ni-coated CFs samples as a function of sintering temperature. As the sintering temperature increased, the TC in X-Y plane direction increased. This result is attributed to the improvements of relative density (Fig. 5.15) and interfacial bonding (Fig. 5.16).
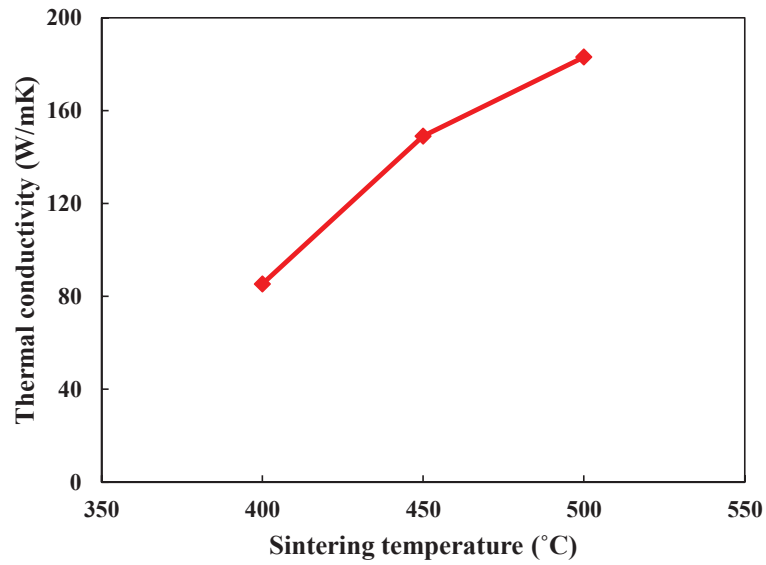
Fig. 5.18 Thermal conductivity in X-Y plane of Al/1.5 min Ni-coated CFs samples as a function of sintering temperature.
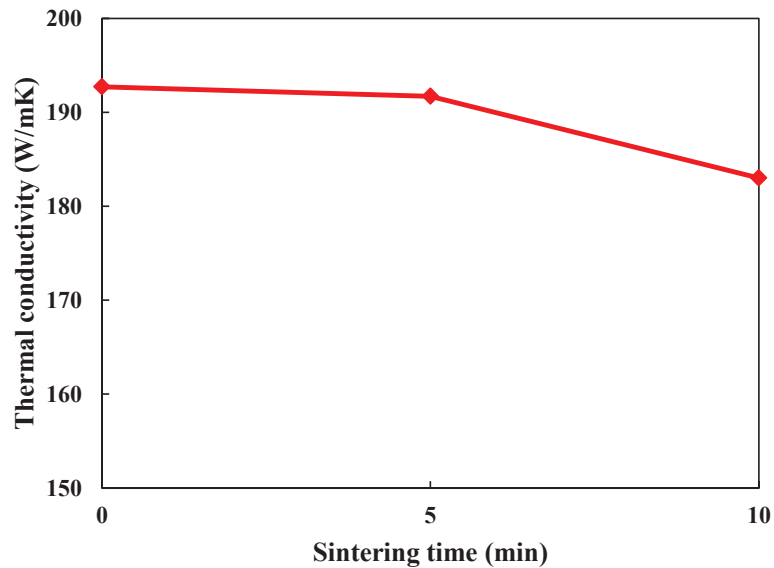
5.3.1.4 Effect of sintering time

Fig. 5.19 Thermal conductivity in X-Y plane of Al/1.5 min Ni-coated CFs samples as a function of sintering time.

Fig. 5.19 shows the TC in X-Y plane direction of the Al/1.5min Ni-coated CFs samples (compacted at 70 MPa and sintered at 500 ˚C) as a function of sintering time.

As the sintering time decreased from 10 min to 5 min, the TC increased from 183 W/mK to 192 W/mK. This might be due to the formation of fewer Al$_3$Ni compounds. With further decreasing the sintering time to 0 min, the TC had small change. This suggests that when sintering time was shorter than 5 min, the amount of Al$_3$Ni compounds may have small effect on thermal conductivity.

5.3.2 Coefficient of thermal expansion

Fig. 5.20 shows the CTE values (measured in the X-Y plane direction) of the SPSed Al/CFs samples with and without Ni coating. It should be noted that the coating time, sintering pressure, sintering temperature, and sintering time of the SPSed Al/Ni-coated CFs composites were 1.5 min, 70 MPa, 500 ˚C, and 0 min, respectively. The addition of CFs in Al matrix caused significant reductions in CTE in comparison with pure Al (26 ppm/K). This is obviously attributed to the negative CTE value of the CFs in the axis direction (-1.45 ppm/K [6]). Furthermore, the samples with Ni coating showed lower CTE values than that without Ni coating, further indicating good Al/CFs interfacial bonding. Besides, although it is difficult to measure the CTE values in the Z plane direction due to limited sizes of the SPSed samples, it is reasonable to assume that the CTE values in the Z plane direction are larger than those in the in the X-Y plane direction, because of higher CTE value of CFs in direction perpendicular to the axis direction (10.0-12.0 ppm/K [7]).
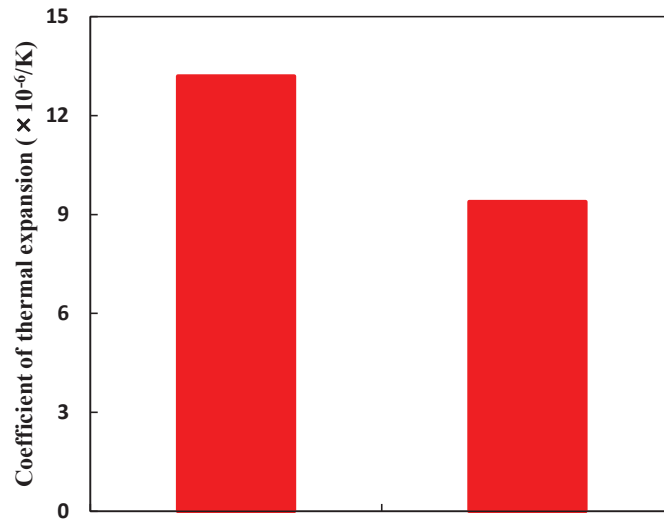
Fig. 5.20 Coefficient of thermal expansion of the SPSed Al/40 vol% CFs samples with and without Ni-coating.

5.3.3 Compressive strength

Fig. 5.21 shows the compressive strength (measured along the X-Y plane direction) of the SPSed Al/40vol% CF samples with and without Ni coating. It should be mentioned that the coating time, sintering pressure, sintering temperature, and sintering time of the SPSed Al/Ni-coated CFs composites were 1.5 min, 70 MPa, 500 ˚C, and 0 min, respectively. The SPSed samples with and without Ni coating showed compressive strength values of 84.2 MPa and 61.8 MPa, respectively. The high strength of the SPSed sample with Ni coating is associated with its high density and strong Al/CFs interfacial bonding.
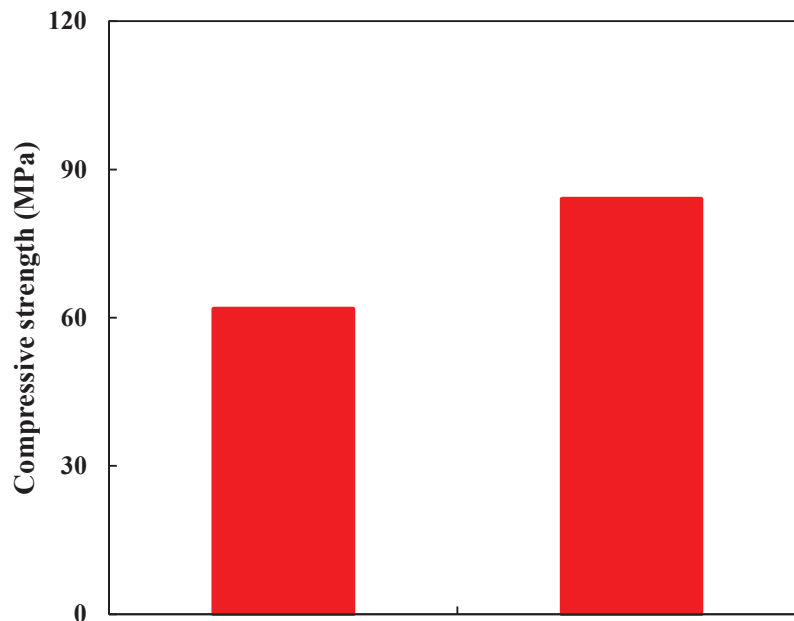
Fig. 5.21 Compressive strength of the SPSed Al/40 vol% CFs samples with and without Ni-coating.

5.4 Conclusions

(1) The application of Ni coating on CFs effectively improved the relative density of the composites and interfacial bonding between Al and CFs, thus leading to enhancement of TC.

(2) The optimum coating time, sintering pressure, sintering temperature, and sintering time for thermal conductivity of SPSed Al/CFs composites were 1.5 min, 70 MPa, 500 ˚C, and 0 min, respectively.

(3) The application of Ni coating on CFs also caused reduction in CTE and improvement in compressive strength.

References

[1] X.H. Qu, L. Zhang, M. Wu, S.B. Ren: Review of metal matrix composites with high thermal conductivity for thermal management applications. Prog. Nat. Sci: Mater. Int.

21. 189-197 (2011).

[2] Z.Q. Tan, Z.Q. Li, D.B. Xiong, G.L. Fan, D. Zhang: A predictive model for interfacial thermal conductance in surface metallized diamond aluminum matrix composites. Mater. Des. 55. 257-262 (2014).

[3] L.G. Hou, R.Z. Wu, X.D. Wang, J.H. Zhang, M.L. Zhang, A.P. Dong, B.D. Sun: Microstructure, mechanical properties and thermal conductivity of the short carbon fiber reinforced magnesium matrix composites. J. Alloy. Compd. 695. 2820-2826 (2017).

[4] J.H. Chen, S.B. Ren, X.B. He, X.H. Qu: Properties and microstructure of nickel-coated graphite flakes/copper composites fabricated by spark plasma sintering. Carbon 121. 25-34 (2017).

[5] K. Raza, F. A. Khalid: Optimization of sintering parameters for diamond-copper composites in conventional sintering and their thermal conductivity. J. Alloy. Compd. 615. 111-118 (2014).

[6] T.T. Liu, X.B. He, Q. Liu, S.B. Ren, Q.P. Kang, L. Zhang, X.H. Qu: Effect of chromium carbide coating on thermal properties of short graphite fiber/Al composites. J. Mater. Sci. 49: 6705-6715 (2014).

[7] H. Kurita, E. Feuillet, T. Guillemet, J.M. Heintz, A. Kawasaki, J.F. Silvain: Simple Fabrication and Characterization of Discontinuous Carbon Fiber Reinforced Aluminum Matrix Composite for Lightweight Heat Sink Applications. Acta. Metall. Sin (Engl. Lett) 27 (4): 714-722 (2014).

Chapter 6   Microstructure and thermal/mechanical properties of Ni-coated carbon fibers/Al composites prepared by hot-extrusion technique

6.1 Introduction

In chapter 5, Al/Ni-coated CFs composites have been successfully fabricated by SPS process. However, the CFs were randomly oriented in plane perpendicular to the pressing direction, which seriously limits the thermal/mechanical properties of Al/Ni-coated CFs composites. In order to align the CFs in one direction, in this chapter, Al/Ni-coated CFs composites were fabricated by hot-extrusion process. The purpose is to investigate the effect of Ni-coating on microstructure and thermal/mechanical properties and find optimal extrusion conditions.

6.2 Experimental

6.2.1 Consolidation method

Firstly, the 1.5 min Ni-coated CFs and pure Al powders (99.99%, 30 µm) were used as the starting materials. The powders with nominal compositions of 40 vol% CFs were mixed under 50 rpm for 8 h. Subsequently, the mixed powders were consolidated by SPS at 500 ˚C for 0 min under 100 MPa (the SPS conditions are listed in Table 6.1), followed by vacuum-encapsulation into an Al can to obtain a hot-extrusion billet. The extrusion was performed in a temperature range of 400-500 ˚C with an extrusion ratio of 14:1 and a punch speed of 1 mm/min (the extrusion conditions are listed in Table 6.2.)

6.2.2 Characterization

The density of the extruded samples was determined by the Archimedes method.

Phase identification was performed by X-ray diffraction (XRD) with Cu Kα radiation. The microstructure was observed and analyzed by scanning electron microscopy (SEM).

With regard to the thermal and mechanical properties of hot-extruded samples, the TC was determined by measuring thermal diffusivity and specific heat at room temperature by using a laser flash apparatus (NETZSCH LFA457, Germany). The specimens for TC measurements were in the form of discs with a diameter of 6 mm and a thickness of 2 mm. The CTE was determined using a horizontal dilatometer (SEIKO TMA/SS6000, Japan) in a temperature range of 20-150 ˚C at a heating rate of 2 ˚C/min. The CTE was measured on cuboid samples with dimensions of 20 mm×5 mm×5 mm. In addition, compression tests were carried out using a universal testing machine (SHIMADZU SFL-50kNAG, Japan) with a compression rate of 1 mm/min. Cylindrical samples with dimensions of Φ6 mm×8 mm were used in the compression tests.

Table 6.1 Conditions of SPS

Atmosphere	Vacuum
Heating rate	30 ˚C/min
Temperature	450 ˚C
Pressure	70 MPa
Sizes of green compact	Φ20mm×10mm

Table 6.2 Conditions of hot extrusion.

Extrusion billet	SPSed compact
Atmosphere	Air
Extrusion temperature	400-500℃
Extrusion ratio	14
Extrusion speed	1mm/min

6.3 Results and discussion

6.3.1 Microstructure

Fig. 6.1 shows the relative density of the hot-extruded Al/40% Ni-coated CFs samples as a function of extrusion temperatures. For the purpose of comparison, the density value of 450 ˚C-extruded Al/40% CFs samples without Ni-coating is also included in the figure. Obviously, the extruded samples with Ni-coating showed higher density values in comparison with those without coating, due to the enhanced interfacial bonding. In addition, as the extrusion temperature increased, the relative density increased gradually. It is considered that Al matrix became softer at a higher extrusion temperature, thus resulting in smaller damages on CFs and Ni layers. Therefore, a denser composite can be obtained at a higher extrusion temperature.
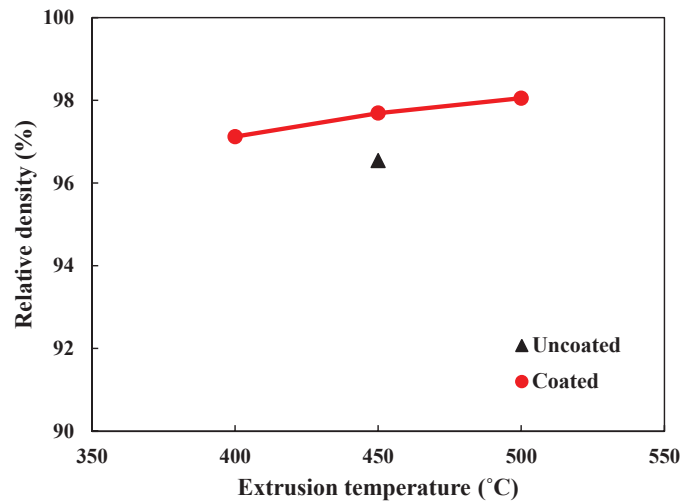
Fig. 6.1 Relative density of hot-extruded Al/40 vol% CFs samples with and without Ni-coating as a function of extrusion temperature.

Fig. 6.2 shows the SEM images (backscattered electron mode) on longitudinal sections of Al/40 vol% CFs samples extruded at different temperatures. The white and dark regions shown in Fig. 6.2 correspond to Al and CF, respectively. The CF was mainly distributed along the extrusion direction in the extruded samples. In comparison with the sample without coating shown in Fig. 6.2 (a), it is obvious that the CFs with coating showed more homogeneous distribution. Moreover, as the extrusion temperature varied, the distribution of the CFs along the extrusion direction showed no obvious change. To further understand the orientation of CFs at different extrusion temperatures, the quantitatively evaluation is underway.
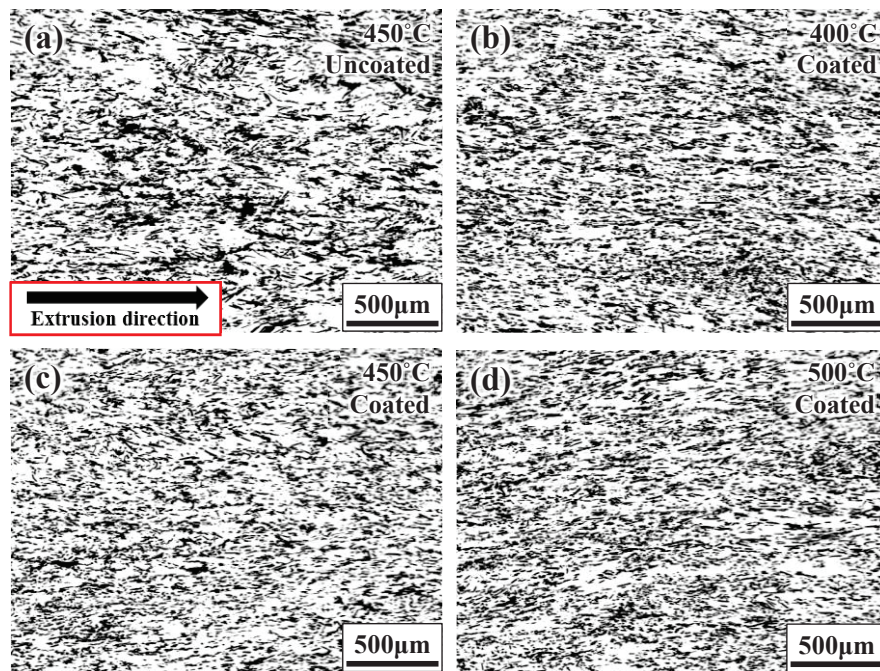
Fig. 6.2 SEM images on longitudinal sections of Al/40 vol% CFs samples extruded at (a) 450 ˚C, uncoated, (b) 400 ˚C, coated, (c) 450 ˚C, coated, and (d) 500 ˚C, coated.

Fig. 6.3 shows the high magnification SEM image (backscattered electron mode) of the 450 ˚C-extruded Ni-coated CFs/Al composite. The dark, gray, and white regions correspond to CFs, Al, and Ni, respectively. It can be observed that many broken Ni layers in the Al matrix. This is considered to be due to the heavy shear deformation during extrusion, which results in the breakage of Ni layer.

To confirm the formation of the reaction product, the composites were further examined by XRD in the range of $2\theta = 41\text{-}50˚$, in which the characteristic peaks of Al_3Ni are included. Fig. 6.4 shows the XRD patterns on longitudinal sections of Al/40 vol% CFs extruded at different temperatures. It should be noted that the extremely strong diffraction peak at $2\theta = 44.7˚$ corresponding to the (200) crystal plane of Al. For the Al/40vol% uncoated CFs sample extruded at 450 ˚C, no other peaks can be observed. However, for the Al/40vol% Ni-coated CFs samples extruded at different temperatures,

eight relatively weak diffraction peaks at about 2θ = 41.4˚, 41.8˚, 43.7˚, 45.3˚, 46.0˚, 47.0˚, 48.4˚, and 49.5˚ were found corresponding to (031), (112), (131), (301), (230), (311), (212), and (040) crystal planes of Al$_3$Ni, respectively, indicating a chemical interfacial bonding. Furthermore, it is clear that the intensities of Al$_3$Ni became stronger with increasing the extrusion temperature.
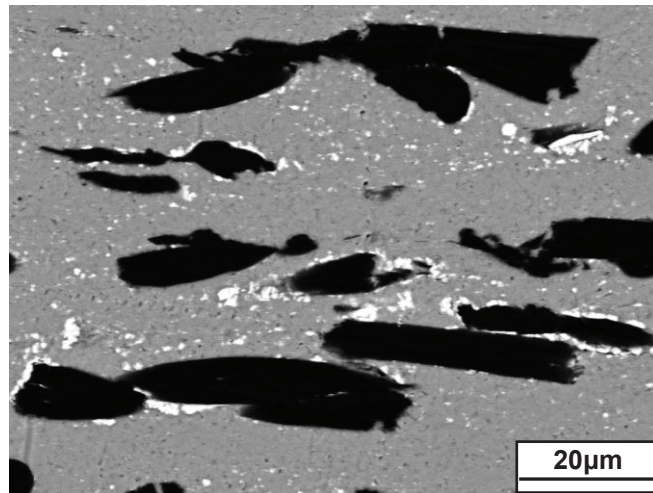

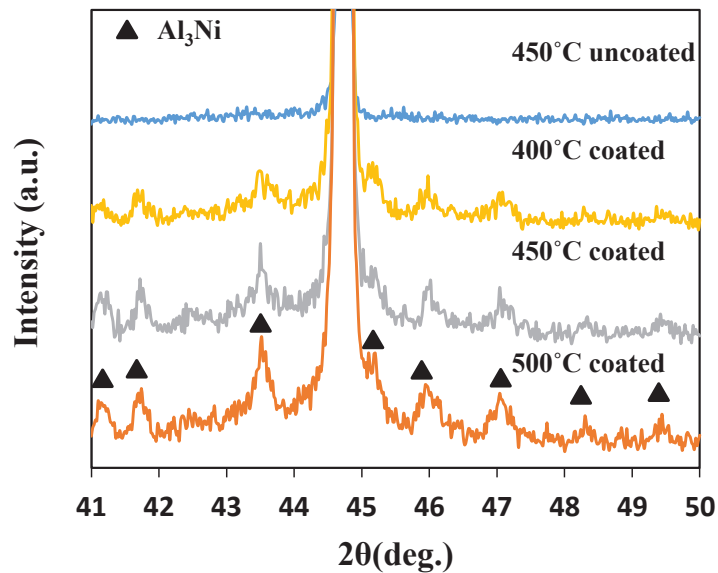Fig. 6.3 High magnification SEM image of the 450 ˚C-extruded Al/40 vol% Ni-coated CFs sample.

Fig. 6.4 XRD patterns of (a) the Al/uncoated CFs sample, and Al/Ni-coated CFs samples with coating times of (b) 1.5 min, (c) 3 min, and (d) 5 min.

101

6.3.2 Thermal conductivity

Fig. 6.5 shows the TC of Al/40 vol% CFs samples with and without Ni coating as a function of extrusion temperature. As a reference, the TC value of a 450 ˚C-extruded pure Al sample is also plotted in the figure. All the extruded Al/CFs samples showed higher TC values in comparison with pure Al extruded sample. With Ni coating on CFs, the TC values were slightly decreased in comparison with those without coating. This might be due to two reasons. (i) The formation of large amount of Al_3Ni compounds during extrusion. (ii) The breakage of Ni layer during the extrusion process (see Fig. 6.3), although the relative density and distribution of CFs were improved. Since the TC of Ni (~88 W/mK) is much lower than that of Al (~200 W/mK), the broken Ni layer in Al matrix may seriously inhibit heat transfer. Furthermore, all the extruded Al/CFs samples showed higher TC values in comparison with the SPSed Al/CFs samples mentioned in Chapter 5. This is attributed to the unidirectional alignment of CFs in the extruded composites.
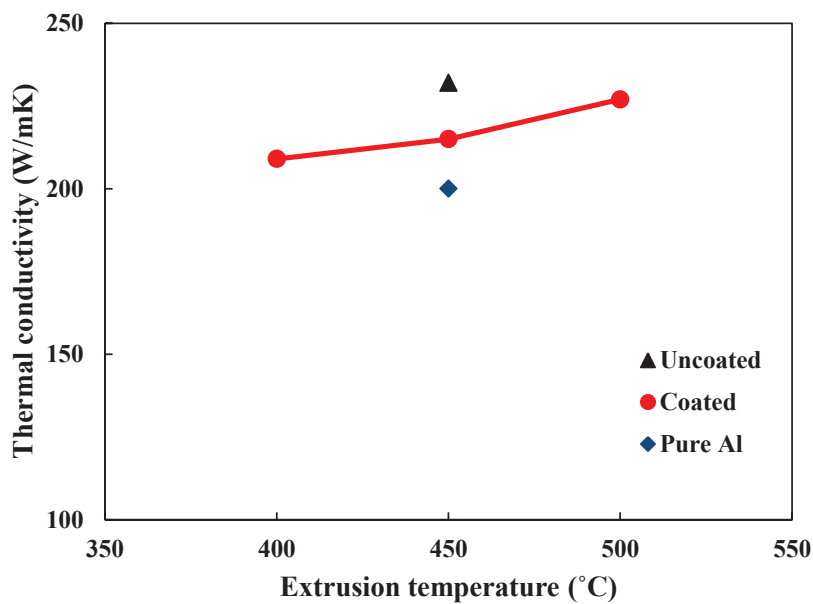

Fig. 6.5 Thermal conductivity of hot-extruded Al/40 vol% CFs samples with and without Ni-coating as a function of extrusion temperature.

6.3.3 Coefficient of thermal expansion

Fig. 6.6 shows the variations of CTE (measured in the extrusion direction) of the extruded and SPSed Al/CFs samples with and without Ni coating. The addition of CFs in Al matrix caused significant reductions in CTE in comparison with pure Al (26 ppm/K). This is obviously attributed to the negative CTE value of the CFs in the axis direction (-1.45 ppm/K [1]). Moreover, the samples with Ni coating showed lower CTE values than that without Ni coating, further indicating good Al/CFs interfacial bonding. Besides, although it is difficult to measure the CTE values in the direction perpendicular to the extrusion direction due to limited sizes of the extruded samples, it is reasonable to assume that the CTE values in the direction perpendicular to the extrusion direction are larger than those in the direction parallel to the extrusion direction, because of higher CTE value of CFs in direction perpendicular to the axis direction (10.0-12.0 ppm/K [2]). Furthermore, the CTE values of the extruded samples were higher than those of the 500 ˚C-SPSed samples. This is considered to be related to the unidirectional alignment of CFs in the extruded composites.
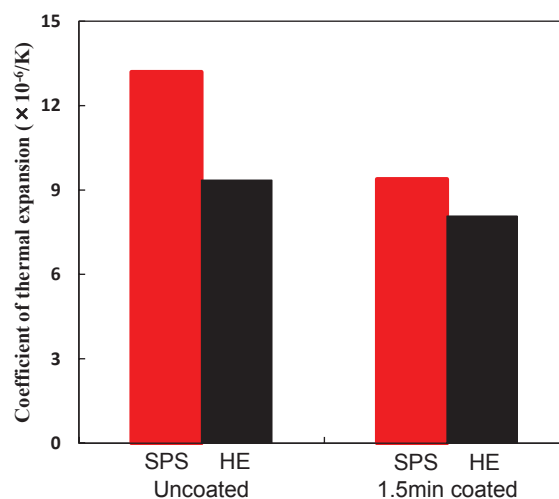

Fig. 6.6 Coefficient of thermal expansion of the extruded and SPSed Al/40 vol% CFs samples with and without Ni-coating.

6.3.4 Compressive strength

Fig. 6.7 shows the compressive strength (measured along the X-Y plane direction) of the extruded and SPSed Al/40vol% CF samples with and without Ni coating. The extruded samples with and without Ni coating showed compressive strength values of 115.8 MPa and 96.8 MPa, respectively. The high strength of the extruded sample with Ni coating is associated with its high density and strong Al/CFs interfacial bonding. Furthermore, the extruded samples showed higher compressive strengths than the 500 ˚C-SPSed samples. This might be due to the higher strength in direction along the CF axis than that in direction perpendicular to the CF axis. Since the CFs aligned in the extrusion direction of the extruded samples, the compressive strength of the extruded samples showed higher values.
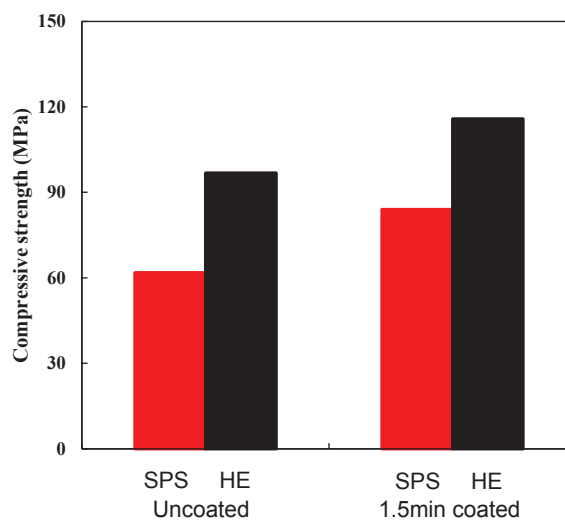

Fig. 6.7 Compressive strength of the extruded and SPSed Al/40 vol% CFs samples with and without Ni-coating.

6.4 Conclusions

(1) Al/Ni-coated CF composites were consolidated by SPS and hot-extrusion processes. The extruded samples with Ni-coating showed more homogeneous distribution than

the sample without Ni-coating.

(2) As the extrusion temperature increased, more Al_3Ni compounds were detected, and the TC of the sample with Ni-coating increased gradually.

(3) The application of Ni-coating on CFs caused reduction in CTE and improvement in compressive strength. However, the TC was decreased in comparison with the sample without Ni-coating.

References

[1] T.T. Liu, X.B. He, Q. Liu, S.B. Ren, Q.P. Kang, L. Zhang, X.H. Qu: Effect of chromium carbide coating on thermal properties of short graphite fiber/Al composites. J Mater Sci 49: 6705-6715 (2014).

[2] H. Kurita, E. Feuillet, T. Guillemet, J.M. Heintz, A. Kawasaki, J.F. Silvain: Simple Fabrication and Characterization of Discontinuous Carbon Fiber Reinforced Aluminum Matrix Composite for Lightweight Heat Sink Applications. Acta Metall. Sin (Engl. Lett) 27 (4): 714-722 (2014).

Chapter 7 Summary

Al/carbon composites have been widely used in the fields of electronic packaging and thermal management applications because of their good thermal and mechanical properties. However, conventional fabrication techniques, such as squeeze casting and hot pressing, are difficult to simultaneously meet the needs of mass production and good thermal/mechanical properties. In the present work, from the viewpoints of mass production and orientation control, a hot-extrusion technique was proposed to fabricate Al/carbon composites, with emphasis on systematically investigating the effect of processing conditions on extrusion behavior, microstructure, texture, and thermal and mechanical properties of the extruded composites. The main results obtained in the present research can be summarized as follows.

Chapter 1 described background of the present research. In order to face the continuing miniaturization and increasing power density of various electronic devices, as well as environmental pollution issues, thermal management materials attract much attention in the recent decades. However, it is difficult to simultaneously meet the needs of mass production and good thermal/mechanical properties. Therefore, a hot-extrusion technique was proposed to fabricate Al/carbon composites. The purpose of present research was to understand the relationships among processing conditions, microstructure, texture, thermoelectric and mechanical properties, thus to promote their industrial applications and contribute to satisfy the requirements of rapid heat removal, long service life, high reliability, and environmental pollution issues. Development status of various AMCs for thermal management applications and fabrication methods are also described in Chapter 1.

In chapters 2, Aluminum/graphite composites have been successfully prepared by a hot-extrusion technique. The effects of processing conditions such as graphite particle size, graphite content, and extrusion temperature on extrusion behavior, microstructure, texture, and TC have been systematically investigated. During the hot extrusion, the graphite was subjected to deformation and hence distributed along the extrusion direction in the extruded Al/graphite composites. The (00l) basal planes of the graphite were preferentially orientated along the extrusion direction. The preferred orientation of the graphite resulted in an anisotropy of TC in the extruded samples. On the other hand, the utilization of bimodal graphite powder consisting of coarse and fine particles is beneficial to the enhancement of both relative density and TC. Moreover, when a pressed green compact was rotated 90° and then subjected to the hot extrusion, the resulting composite exhibited higher TC due to its higher density, fewer Al/graphite interfaces, and higher orientation degree of the graphite.

In chapters 3, in order to simultaneously improve the thermal and mechanical properties of Al/graphite composites, Al/graphite composites with small amounts of Al-Si alloy were consolidated by spark plasma sintering and hot-extrusion processes. The effect of Al-Si alloy addition on densification behavior, microstructure, TC, CTE, and compressive strength has been systematically investigated. The results showed that the addition of Al-Si alloy resulted in improvements in relative density of the composites, interfacial bonding between Al and graphite, and orientation degree of graphite. The composites with Al-Si alloy showed improved TC and reduced CTE values in comparison with those without Al-Si alloy. For example, the 450 ˚C-extruded Al/60 vol% graphite/9 vol% Al-Si composite showed a maximum TC of 297 W/mK and a minimum CTE of 7.95 ppm/K. Moreover, the hot-extruded Al/graphite composites

containing Al-Si alloy exhibited higher compressive strength compared to conventional squeeze-cast composites and hot-extruded composites without Al-Si alloy.

In Chapter 4, Aluminum/carbon fibers (CFs) composites have been successfully prepared by a hot-extrusion technique. The effects of processing conditions such as CFs size, CFs content, and extrusion temperature on extrusion behavior, microstructure, and TC have been systematically investigated. The extruded samples with less than 30 vol% CFs exhibited good appearances with high relative density of > 97%, while those with 40 vol% show some cracks and reduction in relative density. Microstructure observation showed that the CFs were mainly aligned along the extrusion direction (ED) in all the samples. The measured TC along the extrusion direction of extruded samples showed that long CFs exhibited larger improvement in TC compared with short CFs. The resultant TC_{max} of 262 W/mK was achieved for the 450 ˚C-extruded Al/20 vol% long CFs sample.

In Chapter 5, in order to improve the interfacial bonding between Al and CFs, Ni-coating was introduced, and Al/Ni-coated CFs composites were fabricated by SPS process. The effects of Ni-coating on microstructure and thermal/mechanical properties were investigated, and the optimal Ni-coating and SPS process conditions were obtained. The results showed that Ni-coating can effectively enhance the interfacial bonding between Al and CFs, thus resulting in higher density, thermal and mechanical properties.

In Chapter 6, in order to further improve the thermal and mechanical properties, Al/Ni-coated CFs composites were fabricated by hot-extrusion process. The effect of Ni-coating on microstructure, TC, CTE, and compressive strength has been systematically investigated.

Finally, in Chapter 7, general conclusions and summary of this work, as well as some achievements pegged on this work are presented.

Achievements

Journal publications

1. Li-Fu Yi, Noriaki Yoshida, Tetsuhiko Onda, Zhong-Chun Chen, Thermal Conductivity of Aluminum-Graphite Composites Fabricated by Hot Extrusion. [Published in Proceeding of The 9th Pacific Rim International Conference on Advanced Materials and Processing, PRICM 2016, The Japan Institute of Metals and Materials, 211-214 (2016)]

2. Li-Fu Yi, Noriaki Yoshida, Tetsuhiko Onda, Zhong-Chun Chen, Effect of processing conditions on microstructure and thermal conductivity of hot-extruded aluminum/graphite composites. *Materials Transactions* (accepted).

3. Li-Fu Yi, Noriaki Yoshida, Takashi Yamamoto, Tetsuhiko Onda, Zhong-Chun Chen, Microstructure and thermal/mechanical properties of hot-extruded aluminum/graphite composites with Al-Si alloy addition. *Journal of Materials Science* (under review).

International conferences

1. Li-Fu Yi, Noriaki Yoshida, Masashi Takano, Tetsuhiko Onda, Zhong-Chun Chen, Thermal Conductivity of Aluminum-Graphite Composites Fabricated by Hot Extrusion. *The Ninth Pacific Rim International Conference on Advanced Materials and Processing (PRICM9)*, Kyoto, Japan, Aug. 2016.

2. Li-Fu Yi, Noriaki Yoshida, Takahiro Akao, Tetsuhiko Onda, Zhong-Chun Chen, Microstructure and Thermal Conductivity of Aluminum-Graphite Composites Fabricated by Hot Extrusion. *The 6th Joint Symposium on Materials and Mechanical Engineering between Northeastern University and Tottori University*, Tottori, Japan,

Sept. 2016.

3. Tetsuhiko Onda, Li-Fu Yi, Noriaki Yoshida, Zhong-Chun Chen, Microstructure and thermal/mechanical properties of hot-extruded aluminum/graphite composites with Al-Si alloy addition. *The 7th Joint Symposium on Materials and Mechanical Engineering between Northeastern University and Tottori University*, Shenyang, China, Sept. 2018.

Domestic symposia

1. Li-Fu Yi, Noriaki Yoshida, Takahiro Akao, Tetsuhiko Onda, Zhong-Chun Chen, Extrusion Behavior and Thermal Conductivity of Aluminum-Graphite Composites. The 66th Japanese Joint Conference for the Technology of Plasticity, Oct. 2015.

2. Li-Fu Yi, Noriaki Yoshida, Takahiro Akao, Tetsuhiko Onda, Zhong-Chun Chen, Effect of Extrusion Temperature on Thermal Conductivity of Aluminum-Graphite Composites Fabricated by Hot Extrusion. The 158th Spring Annual Meeting of the Japan Institute of Metals and Materials, Mar. 2016.

3. Li-Fu Yi, Noriaki Yoshida, Tetsuhiko Onda, Zhong-Chun Chen, Thermal Conductivity of Aluminum-Carbon Fiber Composites Fabricated by Hot Extrusion. The 9th Chugoku Shikoku Branch Meeting of the Japan Institute of Light Metals, Jul. 2017.

4. Li-Fu Yi, Noriaki Yoshida, Tetsuhiko Onda, Zhong-Chun Chen, Microstructure and Thermal Conductivity of Aluminum-Carbon Fiber Composites Fabricated by Hot Extrusion. The 57th Chugoku Shikoku Branch Meeting of the Japan Institute of Metals and Materials, Aug. 2017.

5. Li-Fu Yi, Noriaki Yoshida, Tetsuhiko Onda, Zhong-Chun Chen, Effect of Al-Si Alloy Addition on Thermal Conductivity of Aluminum-Graphite Composites Fabricated by Hot-Extrusion. The 162th Spring Annual Meeting of the Japan Institute of Metals and Materials, Mar. 2018.

6. Li-Fu Yi, Noriaki Yoshida, Tetsuhiko Onda, Zhong-Chun Chen, Microstructure

and Thermal Conductivity of Hot-extruded Aluminum/Graphite Composites. The Heisei 30th Japanese Joint Conference for the Technology of Plasticity, Jun. 2018.

7. Li-Fu Yi, Noriaki Yoshida, Tetsuhiko Onda, Zhong-Chun Chen, Microstructure, Thermal and Mechanical Properties of Aluminum-Graphite Composites Fabricated by Hot Extrusion. The 10th Chugoku Shikoku Branch Meeting of the Japan Institute of Light Metals, Jul. 2018.

8. Takashi Yamamoto, Li-Fu Yi, Tetsuhiko Onda, Zhong-Chun Chen, Thermal Conductivity of Ni-coated Carbon Fibers/Aluminum Composites. The 58th Chugoku Shikoku Branch Meeting of the Japan Institute of Metals and Materials, Aug. 2018.

Acknowledgements